UNIVERSITÀ DEGLI STUDI DI ROMA "TOR VERGATA"

FACOLTA' DI INGEGNERIA

DOTTORATO DI RICERCA IN
MATERIALI PER L'AMBIENTE E L'ENERGIA

XXI CICLO

IN-SITU STUDY BY ADVANCED SPECTROSCOPIC TECHNIQUES OF MESOPOROUS SILICA FILMS OBTAINED BY SOL-GEL PROCESSING

MASSIMO PICCININI

A.A. 2008/2009

Docente Guida/Tutor: Prof. Plinio Innocenzi

Coordinatore: Prof. Enrico Traversa

Abstract

The possibility of processing mesoporous materials as thin films is especially interesting, due to the combined properties of a thoroughly tailored pore system and the inherent features of thin films. Moreover, a wide variety of inorganic or hybrid frameworks can be easily obtained by evaporation-based methods and thoroughly studied by in-situ techniques. The control of chemical and processing variables also permits the easy creation and reproduction of an amazing library of functional-pore arrays. In this doctorate work, well assessed experimental techniques, as small-angle X-ray scattering (SAXS) and transmission electron microscopy, have been used to characterize thoroughly the mesophase symmetry of silica and hybrid organic-inorganic films and membranes obtained by sol-gel processing, through evaporation-induced self-assembly and dip-coating. For the first time, time-resolved rapid-scan Fourier-transform infrared (FTIR) spectroscopy has been used in-situ to study the kinetics of polycondensation reactions during film formation. The FTIR technique has shown to be very powerful to understand in great detail the chemical-physical processes that take place during film formation. It has been applied in-situ also simultaneously with SAXS, to have both the structural and chemical information and it has allowed to establish the important role of ethanol and water related to micelle formation and mesostructure organization with time. These results have led us to investigate in great detail the evaporation processes of water and ethanol and how they are influenced by the environmental conditions (i.e., relative humidity), which play a fundamental role in the final properties of the as-deposited mesoporous film. The power of the IR technique has been confirmed also by its application as time-resolved FTIR imaging to study the coffee-stain effect in a pure solvent-solute system. Finally, it has been shown that it is possible to fabricate mesoporous functionalized arrays with controlled size and shape by integrating deep X-ray lithography with dip-pen writing. It has been possible to control the quality of the whole production process by means of characterization techniques currently available in a modern synchrotron facility. The successful application of these bottom-up and top-down techniques allows to envisage new fabrication technologies of functional mesoporous materials for applications, such as DNA nano-spotting or lab-on-a-chip devices.

Contents

INTRODUCTION

Nanoscience is one of the fields that will contribute to a high level of scientific and technological development along the 21st century. Nanostructured inorganic, organic, or hybrid organic-inorganic nanocomposites present paramount advantages to facilitate integration and miniaturization of the devices, thus affording a direct connection between the inorganic, organic and biological worlds. The ability to assemble and organize inorganic, organic, and even biological components in a single material represents an exciting direction for developing novel multifunctional materials presenting a wide range of novel properties. Soft chemistry based processes (i.e., chemistry at low temperatures and pressures, from molecular or colloidal precursors) clearly offer innovative strategies to obtain tailored nanostructured materials. The mild conditions of sol-gel chemistry provide reacting systems mostly under kinetic control. Therefore, slight changes of experimental parameters (i.e., pH, concentrations, temperature, nature of the solvent) can lead to substantial modifications of the resulting supramolecular assemblies. This may give rise to inorganic or hybrid solids with enormous differences in morphology and structure and, hence, in their properties. However, the resulting nanostructures, their degree of organization, and thus their properties certainly depend on the chemical nature of their organic and inorganic components, but they also rely on the synergy between these components. Thus, the tuning of the nature, the extent, the accessibility, and the curvature of the hybrid interfaces is a key point in the design of new nanostructured materials.

The growth of soft chemistry derived inorganic or hybrid networks templated by organized surfactant assemblies (structure directing agents) allowed construction of a new family of nanostructured materials in the mesoscopic scale (2-100 nm): the best example is the ever-growing family of meso-organized hybrids or mesoporous inorganic materials. They constitute a challenging domain in materials chemistry that is experiencing explosive growth. In the past few years, an increasing quantity of mesoporous materials with very diverse chemical compositions (oxides, metals, carbons, chalcogenides, semiconductors, etc.) shaped as powders, monoliths, thin films, membranes, or fibres have appeared. Different families of such materials were discovered through innovative combinations of templates or texturing agents (ionic and non-ionic surfactants, amphiphilic block copolymers, biopolymers, ionic liquids, dendrimers, etc.), starting from mineral precursors (salts, alkoxides, organosilanes, nanobuilding blocks: clusters, nanoparticles, etc.) and sol-gel reaction media (solvents, water content, pH, complexing agents, aging conditions, etc.). These novel materials offer a high degree of versatility in terms of structure, texture, and functionality.

The possibility of processing mesoporous hybrid materials as thin films is especially interesting, for the combined properties of a thoroughly tailored pore system and the inherent features of thin films (i.e., accurate control of thickness, composition, transparency, presence of electrodes, possibility of multilayer stacking etc.). Moreover, a wide variety of inorganic or hybrid frameworks can be easily obtained, as evaporation-based methods are usually more flexible than precipitation and can be thoroughly studied by in-situ techniques. The control of chemical and processing variables permits the easy creation and reproduction of an amazing library of functional-pore arrays. These functions can be in turn activated or modified by solicitations such as light, current or a changing environment, making mesoporous hybrid thin films an exciting prospect for several nanotechnology applications (sensors, actuators, separation and interfacing devices, etc.).

Mesoporous films are typically produced after evaporation of solutions containing an inorganic precursor (alkoxide, chloride or mixtures of both), an organic supramolecular template (mostly ionic, non-ionic or polymeric surfactants) and some additives (in general, acidic or complexing molecules to control pH, thus avoiding inorganic extended condensation) dissolved in a volatile solvent (mostly alcohols or ethers). In principle, pore size and symmetry can be adequately tuned by the use of the organic template, from relatively small ionic surfactants to amphiphilic block copolymers. The nature of the wall (whether inorganic or hybrid) and surface can be controlled by choosing the adequate precursor and controlling the sol–gel chemistry of the metal centre. Deposition techniques are varied: from controlled drying of deposited droplets to dip- or spin-coating. The deposition environment, the evaporation process and the resulting film thickness are important not only for the formation of porosity, but also for the symmetry of the pore array. The complex processes taking place during solvent evaporation and subsequent formation of an inorganic-template organised mesophase can be overall ordered in the so-called “evaporation-induced self-assembly” (EISA).

Within this research framework is placed the subject of this doctorate thesis, in particular, my attention has been focused on mesoporous silica films obtained by sol-gel processing and EISA.

In chapter 1 are reported the basic concepts regarding the synthesis of mesoporous materials, with particular attention to films, discussing concepts regarding sol-gel and surfactant chemistry and physics, but particular attention is given to silica mesoporous films templated by amphiphilic block copolymers.

Chapter 2 provides both theoretical and technical information on the in-situ characterisation techniques employed in the experimental part of this doctorate work. As a matter of fact, because mesostructure formation often occurs in a few seconds during the deposition process, in-situ

characterisation has been carried out using advanced spectroscopic techniques and special configurations.

In chapter 3 is demonstrated how this in-situ study plays a central role to understand thoroughly the physics and chemistry underlying templated self-assembly in mesostructured films. In particular, time-resolved Fourier-transform infrared (FTIR) spectroscopy and small-angle X-ray scattering (SAXS) have been applied, also simultaneously, during film formation obtained by EISA and dip-coating. On the other hand, both these techniques are applied also ex-situ after completion of film formation, in order to have a detailed sample characterization, especially concerning the mesophase symmetry.

Starting from all that is described in chapter 3, chapter 4 reports the results of the research carried out moving towards two opposite directions. The first direction pointed to investigating the basics of EISA in sol-gel processing. The relative humidity strongly affects the overall process, so the knowledge of the physics and the chemistry behind the evaporation of solvents, especially of ethanol and water, which are the most commonly used, is very important: these processes have been studied by time-resolved FTIR spectroscopy. The second direction pointed to nanotechnology applications. By time-resolved FTIR imaging, we have studied the coffee-stain effect, as it has been observed for a large variety of solvent-solute systems and it was shown that controlled stain effects can be used to pattern solid surfaces by a self-assembly mechanism and several applications in nanotechnology have been envisaged. Another experiment was performed by patterning mesoporous silica films by means of deep X-ray lithography using synchrotron radiation, obtaining mesoporous objects with controlled size and shape; then an atomic force microscope enabled a particular selective functionalisation of the objects. Also this experiment allowed envisioning new fabrication technologies of functional mesoporous materials.

CHAPTER 1

Mesoporous materials synthesized by sol-gel processing

The importance of porous materials is testified to by their widespread use both in industrial and in household products. The discovery of mesoporous silica and aluminosilicates with ordered pore arrangement and tuneable pore size ranging from 1 to tens of nanometres provided a solution and constituted a starting point for new porous materials for traditional (e.g. catalytic and separation) and advanced (e.g. sensing, electronics) applications. The synthesis of mesoporous materials in the form of homogeneous films was a very important breakthrough because it allowed the development of materials for advanced applications, e.g. in optics, sensing and microelectronics.
In this chapter are reported the basic concepts regarding the synthesis of mesoporous materials, with particular attention to films, discussing concepts regarding sol-gel and surfactant chemistry and physics. Particular attention is given to silica mesoporous films templated by amphiphilic block copolymers, due to their major importance in this doctorate work.

1.1 Nanostructured materials

1.1.1 Main features and synthesis techniques

Nanotechnology can be thought as a new approach to scientific research, spanning different areas characterized by marked interdisciplinarity. It essentially consists in the design, fabrication and application of structures with feature size in the nanometre scale (1 to 100 nm), be it individual particle size or interparticle distance.
Nanotechnology implies the study and the comprehension of phenomena and physicochemical properties of matter at the nanoscale that, when applied to materials science and engineering, can offer concepts, tools and models for the preparation of nanomaterials with highly innovative properties. As a matter of fact, when at least one characteristic length of a material is in the nanometre range, physical and chemical properties can be profoundly different than at the macroscopic scale. This gives rise to an ensemble of new functional properties upon which devices can be built that have a potential to contribute to a high level of scientific and technological development. The reason for this behaviour is mainly twofold: the increase in surface area and

quantum size effects. As the size of a material decreases, the ratio between the number of atoms that lie on the surface (a_s) and the total number of atoms (a_{tot}) increases. Let us consider a cube of size l =1 cm that has a volume density of ~10^{23} atoms·cm^{-3} and a surface density of ~10^{15} atoms·cm^{-2}: the ratio $f = a_s/a_{tot}$ is $f \sim 6 \cdot 10^{-8}$. For smaller l values, f is correspondingly larger, e.g. if l =1 nm, we obtain f ~ 0.6, that is to say 60% of the total atoms lies on the surface. Because the energy at the surface of a material is different than in the bulk, the energy of a material on the nanoscopic scale is different than at the macroscopic scale. This can be a very important property for applications that involve chemical reactions at interfaces, such as in catalysis.

In the intermediate size range between matter at the molecular and at the macroscopic scale, individual energy states of molecules and continuous energy bands of solids become discrete and their energy separations display a dependence on the spatial dimension of the material, which in principle can be calculated by solving the Schrödinger equation for an electron in a box that has a size on the order of the Bohr radius of the electron. This causes particular electronic and optical properties to emerge as a function of size, e.g. plasmonic resonance frequency in metallic nanoparticles and tuneable energy gap in semiconductor nanoparticles (quantum dots). These properties are exploited for advanced applications, e.g. in electronics, linear and non-linear optics.

Surface area and quantum size effects can explain a number of effects caused or enhanced by small size, such as magnetic or mechanical properties. The critical length below which matter shows interesting behaviour will obviously depend on the material itself and on the particular property one is considering, therefore one or more different critical lengths can be defined from case to case.

All synthetic approaches of nanomaterials fall into two categories: top-down and bottom-up. Top-down techniques start from a bulk material and reduce its dimensions by chemical etching, mechanical grinding, lithography until a nanomaterial is obtained. Bottom-up syntheses involve the assembly of small (generally atomic or molecular) units into the desired structure. Since both approaches have upsides and downsides, it is not possible to determine which is the best synthetic strategy regardless of the final structure that has to be obtained. However, we can say that the possibility of building structures defined at the atomic or molecular level is a prerogative of bottom-up syntheses, whereas complex structures such as micro- and nanoscopic interconnects and circuits can be obtained by top-down approaches.

1.1.2 Self-assembly: a bottom-up synthesis approach for nanomaterials

The strategies for the synthesis of nanomaterials using bottom-up approaches involve the assembly of small units, called nano-building blocks (NBBs), into a nanostructure, where NBBs are arranged according to a well defined shape and architecture. Among all bottom-up techniques, one of

outstanding interest is self-assembly (SA), which is the basis of all syntheses presented in the experimental part of this thesis.

The distinctive aspect of SA is that the driving force that causes the NBBs to assemble into the final structure is strictly local, and there is no intervention of external forces. Starting from suitable NBBs with tailored size and shape, composition and surface structure, charge and functionality, one can obtain various nanostructures by a SA process which may be spontaneous, directed by templates or guided by chemically or lithographically defined surface patterns. These nanostructures are shaped into architectures that perform a function.

Within the framework of this thesis, we can define self-assembly in chemistry as the spontaneous and reversible organization of molecular units into ordered structures by non-covalent interactions [1]. Three main aspects make SA a distinct concept: (1) the self-assembled structure must have a higher order than the isolated components; (2) weak interactions (e.g. Wan der Waals, capillary, p-p, hydrogen bonds) play a key role with respect to covalent, ionic or metallic bonds; (3) the building blocks are not only atoms and molecules, but span a wide range of nano- and mesoscopic structures, with different chemical compositions, shapes and functionalities.

Another characteristic that is common to nearly all self-assembled systems is their thermodynamic stability: in order for SA to take place without the intervention of external forces, the process must lead to a lower Gibbs free energy, thus self-assembled structures are thermodynamically more stable than the single, unassembled components. Weak interactions and thermodynamic stability can be recalled in order to rationalise another property which is often found in self-assembled systems: the sensitivity to perturbations exerted by the external environment: small fluctuations that alter the thermodynamic variables might lead to marked changes in the structure and even compromise it, either during or after SA. The weak nature of interactions accounts for the flexibility of the architecture and allows for rearrangements of the structure in the direction determined by thermodynamics. If fluctuations bring the thermodynamic variables back to the starting condition, the structure is likely to go back to its initial configuration. This leads us to identify one more property of SA, which is generally not observed in materials synthesised by other techniques: reversibility.

Generally speaking, the fundamental condition in order to have NBBs to self-assemble into an ordered structure is the simultaneous presence of long-range repulsive and short-range attractive forces [2]. In Table 1.1 are given a few examples of repulsive-attractive competing forces that can give rise to SA phenomena.

Long-range repulsion	Short-range attraction	Example
Hydrophobic-hydrophilic interaction	Covalent bonding	Micelles, lyotropic liquid crystals
Coulomb repulsion	Electroneutrality	Ionic crystals
Excluded volume	Minimum space required	Thermotropic liquid crystals
Electric dipole field	Electric dipole interaction	Ferroelectric domains
Magnetic field	Magnetic dipole interaction	Magnetic domains

Table 1.1. Examples of long-range repulsive and short-range attractive competing forces that give self-assembled systems.

When structure-directing species (often molecular and organic) are used that serve to fill space, balance charge and direct the formation of a specific structure in addition to the self-assembling NBBs, the process is referred to as templated self-assembly. This is the most used technique to synthesize mesoporous materials.

1.2 Porous and mesoporous materials

1.2.1 Importance of porous materials

Porous materials containing cavities in the nanometre and micrometre range (e.g. sponges, clay, zeolites) hold a significant position in industry owing to their widespread use both in industrial and in household products. Well-known applications include catalysis, filtration, extraction, cleaning and sorption. In all these cases, the synthesis of a porous material must allow for the control of the pore dimension and size distribution, which is generally required narrow and centred on a given value. Advanced applications of materials containing porosity require pores that may be either interconnected and open to the external environment, e.g. to allow for the diffusion of analytes in sensors, or isolated and inaccessible, e.g. in low dielectric constant materials in microelectronics [3,4].

According to IUPAC classification [5], porous solids fall into three categories according to pore size (d): microporous ($d < 2$ nm), mesoporous (2 nm $< d < 50$ nm) and macroporous ($d > 50$ nm). Microporous and mesoporous materials are generally referred to as nanoporous materials, which fall into the general class of nanostructured materials, since they possess features (pores) which are defined on the nanoscale.

Zeolites were among the first porous materials with pores in the nanometre range to be synthesised, and they certainly represent the most known class of microporous materials. Zeolites are available from natural resources but there exist synthetic routes that permit obtaining zeolites with well-

defined framework composition and pore size. Natural zeolites are hydrated aluminosilicates of alkali metals or alkaline earth metal ions, characterised by cavities and channels of molecular dimension that permeate the whole structure. Alkaline and alkaline earth cations are localised in the cavities and serve to maintain electroneutrality.

The motivation for research on mesoporous materials was the demand for porous materials similar to zeolites (narrow pore size distribution, thermal, chemical and mechanical properties), but with larger pores. In particular, larger pores could afford catalysis of larger molecules, thus extending applications to chemical reactions involving macromolecular reactants. The pioneering work of a Mobil Oil research group provided a first answer to the need for larger pores in 1992, when the first family of mesoporous materials, named M41S, was synthesised [6].

1.2.2 Templated self-assembly of mesoporous materials

In the case of mesoporous materials, the self-assembly of molecular inorganic NBBs is directed by the presence of a structure-directing agent, which serves as a scaffold for the polycondensation of the inorganic NBBs. The structure-directing agents are essentially supramolecular structures formed by the aggregation of amphiphilic molecules such as surfactants, which are molecules containing both hydrophilic and hydrophobic groups. Surfactants exhibit a particular behaviour in solution: above a certain concentration (critical micelle concentration, *cmc*) the surfactant molecules undergo a microphase segregation process in order to minimise the free Gibbs energy, forming supramolecular aggregates (micelles), whose shape is determined by the nature and the architecture of the organic building units, as well as by other parameters such as nature of the solvent, pH and presence of ions. Inorganic polycondensation reactions take place around the templating supramolecular units and yield a hybrid network, constituted by a gel hydrated by solvent molecules. A thermal treatment (calcination) is then performed to remove the templating agent and stiffen the inorganic framework by promoting further inorganic condensation. Alternatively, the organic mesophase can be removed by solvent extraction.

The synthesis of mesoporous materials requires knowledge of the chemistry and the physics of the inorganic and organic component units. In many cases inorganic chemistry is that of sol-gel systems, since inorganic precursors are often alkoxides, organoalkoxides and inorganic salts that undergo hydrolysis and condensation reactions. On the other hand, supramolecular self-assembly of organic species borrows many concepts from colloidal and polymer chemistry and physics. Therefore, we will now deal briefly with the general concepts of self-assembly and sol-gel chemistry.

1.2.3 Inorganic polycondensation and sol-gel processes

Sol-gel processing is based on the controlled polymerisation of inorganic molecular precursors in mild temperature conditions, organic solvents, and controlled amounts of water. This technique is crucial in the development of synthesis routes towards the inorganic NBBs.

Oxide formation by the sol-gel process implies connecting the metal centres with oxo or hydroxo bridges, generating metal-oxo or metal-hydroxo polymers in solution. A colloidal suspension (sol) evolves through polycondensation reactions towards the formation of a continuous solid with the desired shape (e.g. monolith, film, powder) in which a liquid phase is intercalated (gel). Upon drying, a solid is formed, next thermal treatment may then be performed in order to favour further polycondensation reactions and enhance mechanical properties.

The precursor is either an alkoxide, i.e. a compound where a metal (e.g. Ti, B, Al, Ga, Zr, Y, Ca) or metalloid (Si, Ge) is chemically bonded to one or more organic groups through an oxygen atom, or an inorganic salt, generally a transition metal chloride.

Hydrolysis of an alkoxy group attached to a metal centre leads to hydroxyl–metal species:

$$M(OR)_n + H_2O \rightarrow M(OR)_{n-1}(OH) + ROH$$

The hydroxylated metal species can react with other metal centres leading to condensation reactions, in which an oligomer is formed by bridging two metal centres. Condensation can lead to an oxo bridge, and water or alcohol is eliminated:

$$M(OR)_n + M(OR)_{n-1}(OH) \rightarrow (RO)_{n-1}M\text{-}O\text{-}M(OR)_{n-1} + ROH$$

$$M(OR)_{n-1}(OH) + M(OR)_{n-1}(OH) \rightarrow (RO)_{n-1}M\text{-}O\text{-}M(OR)_{n-1} + H_2O$$

Therefore, metal centres end up linked by bridging oxygens in a network. Since this condensation process results in the assembly of a macromolecule starting from monomer units, freeing smaller molecules such as water and alcohol for each new unit linked to the forming structure, it is similar to organic living polymerisation, which somehow justifies the term “inorganic polymerisation” that is often used as a synonym for polycondensation.

The effect of catalysis has a dramatic effect on the microstructure of the solid that is obtained by hydrolysis and condensation reactions of the precursor sol [7,8]. Let us consider the case of silica, as it is the most relevant in the scope of this thesis.

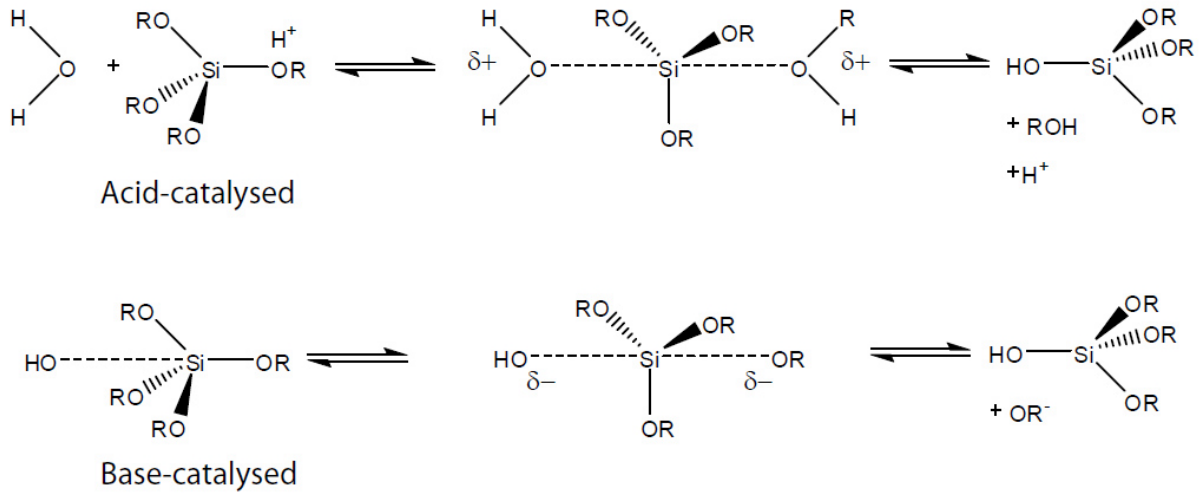

Figure 1.1: Scheme of acid- and base-catalysed hydrolysis from silicon alkoxide.

In acidic conditions an alkoxy group is protonated in a rapid first step; electron density is withdrawn from the Si atom, making it more electrophilic and thus more susceptible to attack from water: this results in the formation of a positively-charged five-coordinate transition state which decays by displacement of an alcohol and inversion of the silicon tetrahedron (Figure 1.1). Conversely, in basic conditions an OH group directly attacks a Si atom forming a five-coordination, negatively charged transition state.

The rate of hydrolysis and condensation of the 4 alkoxy groups bonded to a Si atom can be understood in terms of electronic effects, bearing in mind that alkoxy groups (OR) are electron-donating groups, whereas hydroxyl groups (OH) are electron-withdrawing. Therefore, a substituting OH withdraws electron from the central Si atom and the positively-charged transition state in acid-catalysed hydrolysis becomes less stabilised as more alkoxy groups are substituted by hydroxyl groups and the reaction rate decreases. Conversely, in base-catalysed hydrolysis the negatively-charged transition state becomes more stabilised as more alkoxy groups are substituted by hydroxyl groups, thus more highly hydrolysed silicones are more prone to attack and the reaction rate increases. This means that in acidic conditions one molecule of silicon alkoxide is one- or two-substituted by OH groups, whereas in basic conditions the silicate species will be almost fully hydrolysed.

Condensation reactions proceed according to the same principle. In acidic conditions the transition state is positively charged and stabilised by electron-donating alkoxy groups, therefore less substituted $(RO)_3SiOH$ condense faster than $(RO)_2Si(OH)_2$, which condenses faster than $ROSi(OH)_3$ and $Si(OH)_4$. As a consequence, an open network forms initially, followed by further hydrolysis and cross-condensation reactions. In contrast, in base-catalysed condensation fully

hydrolysed species condense and form branched clusters which eventually link to form gels with large pores between the interconnected clusters. Acid-catalysed sols are more suitable for depositing films by dip- or spin-coating, whereas base-catalysed sols are used e.g. for the synthesis of silica nano- and micro-spheres [9].

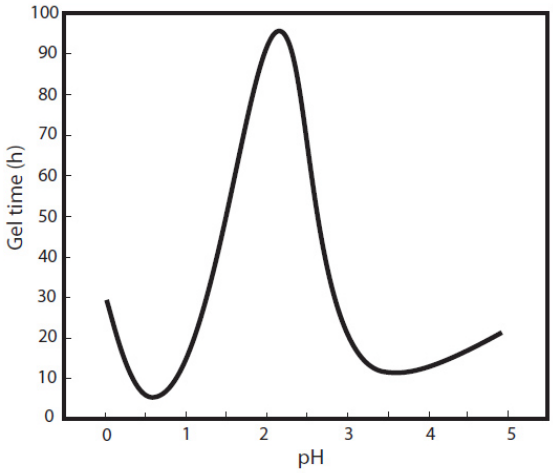

Figure 1.2: Gel time as a function of pH for HCl-catalysed TEOS ($[H_2O]/[Si] = 4$).

The rate of reaction at different pH values shown in Figure 1.2 can be understood in these terms, considering that the isoelectric point of silica (i.e. where the equilibrium species has zero net charge) is at pH_{iep}=2.2. Below pH_{iep} the condensation rates are proportional to $[H^+]$. Between pH=2 and pH=6 condensation rates are proportional to $[OH^-]$. Above pH=7 condensed species are ionised and therefore mutually repulsive: growth occurs primarily through the addition of monomers to the more highly condensed particles rather then by particle aggregation. Due to the greater solubility of silica above pH=7, the reaction rate decreases again.

1.2.4 Supramolecular structures

In the synthesis of mesoporous materials, one exploits the self-assembly of amphiphilic molecules or macromolecules, which are constituted by a hydrophobic region (typically an aliphatic chain) and a hydrophilic region (typically an ion or a polar organic group). The most representative category goes under the name of surfactants, a term referring to the property of lowering the interface energy between a hydrophobic and a hydrophilic phase (surface active agent).

In general, amphiphilic molecules and macromolecules show a tendency to self-assemble forming micelles when their concentration in a polar solvent is higher than a critical micellar concentration ($c > cmc$). Micelles in a polar solvent are constituted by a finite number of amphiphilic units in which the hydrophobic regions form the core of the micelle, whereas the hydrophilic ends point towards the exterior and are swelled by solvent molecules (in an apolar medium it is the other way

round: hydrophilic cores are surrounded by a hydrophobic corona). Micelle shape is determined by the interactions between the amphiphilic units and the solvent molecules. For higher concentrations (c >> *cmc*) micelles can form lyotropic phases, where micelles form periodic ordered patterns [10]. Some examples of micellar aggregates are shown in Figure 1.3. We will discuss the formation of supramolecular structures in more detail in the next sections.

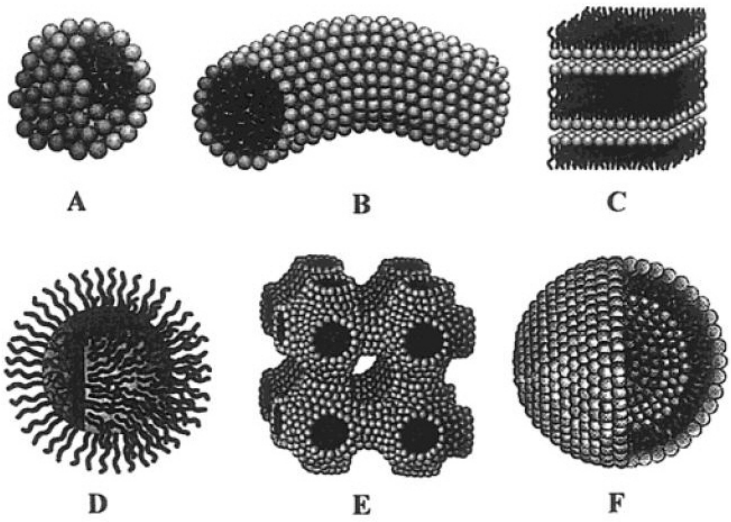

Figure 1.3: Examples of micellar structures: (A) sphere, (B) cylinder, (C) planar bilayer, (D) reverse micelles, (E) bicontinuous phase, (F) liposomes.

1.2.5 Thermodynamic and kinetic considerations on the synthesis of mesoporous materials

The formation of an ordered mesostructure consists in the spatial organisation of hydrophilic and hydrophobic species, which are separated by a so-called hybrid interface (HI). Four different contributions to the Gibbs free energy of mesostructure formation, ΔG_{ms}, can be devised:

$$\Delta G_{ms} = \Delta G_{inter} + \Delta G_{inorg} + \Delta G_{org} + \Delta G_{sol}.$$

The term ΔG_{inter} accounts for the Van der Waals and electrostatic interactions between the organic and the inorganic species at the HI. ΔG_{org} contains the electrostatic interactions between the hydrophilic groups, together with the Van der Waals interactions and the conformational energy of the hydrophobic surfactant chains. As the inorganic phase contains units that may undergo polycondensation, the term ΔG_{inorg} describes the energetics of the electrostatic and intermolecular interactions of the inorganic units in the polycondensation process. The solution chemical potential is given by ΔG_{sol}.

In cooperative assembly routes leading to the formation of a mesostructure, the surfactant concentration is much lower than in water-surfactant lyotropic phases. This fact has been rationalised with the formation of hybrid intermediate states as NBBs in the formation of the mesostructure, which results in a lower *cmc*. As a consequence, the creation of a HI between the organic and inorganic species is a fundamental requisite for the formation of micelles with a well-defined curvature. This leads us to conclude that the term ΔG_{inter} predominates over the other free energy contributes, in particular: $|\Delta G_{org}| << |\Delta G_{inter}|$. This is evident in the syntheses of mesoporous silica performed at high pH values (pH>13) where the formation of small oligomeric silica species prevails over long-range condensation. In such a system, the process of mesostructure formation can be decoupled from inorganic polymerisation and we can consider $|\Delta G_{inorg}| \dashrightarrow 0$. Since an ordered mesophase appears at low surfactant concentrations, the free energy of HI formation is confirmed to be the most important term [11]. On the other hand, in synthesis conditions where inorganic condensation is not inhibited, further rearrangements of the mesostructure can take place through siliceous condensation, which can be brought about by adjusting pH and temperature. In this case, inorganic condensation alters the charge balance at the interface, therefore the system responds by adopting a new morphology in order to re-establish electroneutrality. This accounts for rearrangements in mesophase symmetry.

The thermodynamic aspect on the formation of a HI must be combined with kinetic considerations. The formation of a well-ordered mesostructure can be hindered if inorganic condensation is too fast, eventually leading to a product with disordered or even absent porosity. No matter if the creation of an ordered mesostructure is thermodynamically favoured: if inorganic polycondensation is too fast, no order will be obtained. When inorganic condensation is slow, the kinetic constants are ordered such that $k_{inter} > k_{org} > k_{inorg}$. Therefore, mesostructure formation is controlled by the formation of a HI. On the other hand, if inorganic condensation is too fast ($k_{inorg} > k_{inter}$ or $k_{inorg} > k_{org}$) the formation of a HI may be inhibited even in favourable thermodynamic conditions [11].

To summarise, there are two aspects of thermodynamic and kinetic order which are at play in the synthesis of mesostructured materials: interactions between inorganic and organic precursors which cooperate in forming a well-defined HI, and reactivity of inorganic precursors (polymerization rate, isoelectric point, etc.).

1.2.6 Self-assembling templates

It is a well-known fact that amphiphilic molecules in water solution can form a variety of supramolecular aggregates (spherical, cylindrical, lamellar, etc.) which in turn self-organise into ordered structures with different symmetries (cubic, hexagonal, gyroid, etc.). Their symmetries and

morphologies show a strong dependence on solution parameters such as pH or electrolyte concentration.

At low concentration, amphiphilic molecules are present in aqueous solvent as free molecules, whose polar head is solvated. When the concentration is raised above *cmc* the molecules self-assemble into micelles with a well-defined shape and aggregation number (i.e. average number of molecules per aggregate). At higher concentrations a series of phase transformations may take place, related to changes in the curvature radius of the micelles. This phase transitions follow a general sequence with increasing concentration: direct spheres, direct cylinders, lamellae, inverse cylinders and inverse spheres (see Figure 1.3). It should be noted how this sequence corresponds to a monotonic change in the curvature at the interface. The architecture of the final materials will directly rely on the nature of the surfactant molecules, that is, the morphology of the micellar aggregates and the interactions at the inorganic-organic interface (solvent-micelle interaction, in the case of solutions). Thus, knowledge of the polar head geometry and charge of the surfactants is essential.

Different models have been proposed to explain these experimental facts, the main parameters taken into account being (1) the hydrophobic interactions between organic chains, (2) geometric restrictions due to molecular packing, (3) molecule exchange between aggregates, (4) enthalpy and entropy of packing, and (5) electrostatic repulsion between polar heads. A relatively simple model proposed by Israelachvili and colleagues [12,13] based on geometrical considerations, explains and predicts the resulting self-assembled structures of each type. This model considers a hydrophobic liquid-like core, the contribution of which is merely due to geometrical constraints.

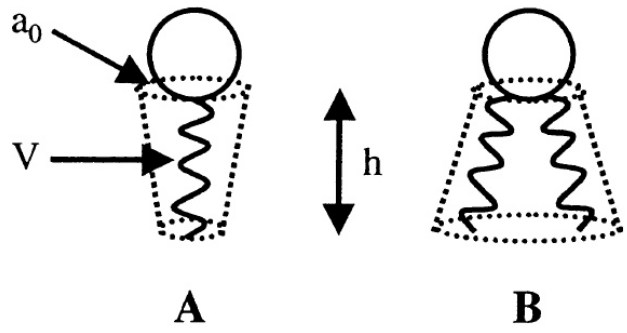

Figure 1.4: Schematic representation of amphiphilic molecules, adopting conical shape (*ice-cream cone*, A) or inverse conical (*champagne cork*, B).

These geometrical considerations rely on the ratio of the polar head surface to the hydrophobic volume. The amphiphilic molecules are thus modelled like a conical fragment (the hydrophobic part) attached to a spherical (hydrophilic) head. Two main shapes are possible (Figure 1.4): direct conical, or *ice-cream cone* (one hydrophobic chain), and inverse conical, or *champagne cork* (two

hydrophobic chains). The steric hindrance of the hydrophobic chain is characterized by the ratio v/l, where v is the chain volume (considered incompressible, for the sake of simplicity) and l is the chain length. In the case of the polar head, its contribution is given by the effective optimal surface, a_0, at which the opposing steric or ionic repulsion forces of the headgroups and the hydrophobic attraction forces inducing molecules to aggregate, are balanced. To ensure chain fluidity, l must verify that $l < l_c$, where l_c is the length of the fully extended chain; l_c can be easily estimated as a function of the number of C atoms in the chain, n. The value of the packing parameter, defined as $g = v/l_c a_0$, can be calculated after the three parameters v, l_c, a_0 are known (by means of calculation or measurement) and it links the molecular structure of the amphiphilic molecule to the architecture of the aggregates.

One can also experimentally conclude that amphiphilic molecules with large polar headgroups tend to form high-curvature spherical aggregates, which will pack according to a cubic symmetry, whereas molecules with longer hydrocarbon tails or smaller polar headgroups will give cylindrical structures packed in a 2d-hex fashion, or lamellae. Surfactants with two hydrocarbon tails have a larger volume (v), therefore they will tend to form bilayers or vescicles (e.g. cell membranes are natural examples formed by the self-assembly of phospholipids, which have two hydrophobic tails; see Figure 1.5). Finally, for $g > 1$ inverse micelles are favourite, where the hydrophilic headgroups point inwards. Table 1.2 gives a guideline for the correlation between the packing factor g and the resulting mesophase symmetry. Huo et al. [14] were the first to take into account the g parameter to explain the formation of different surfactant-templated oxide mesostructures.

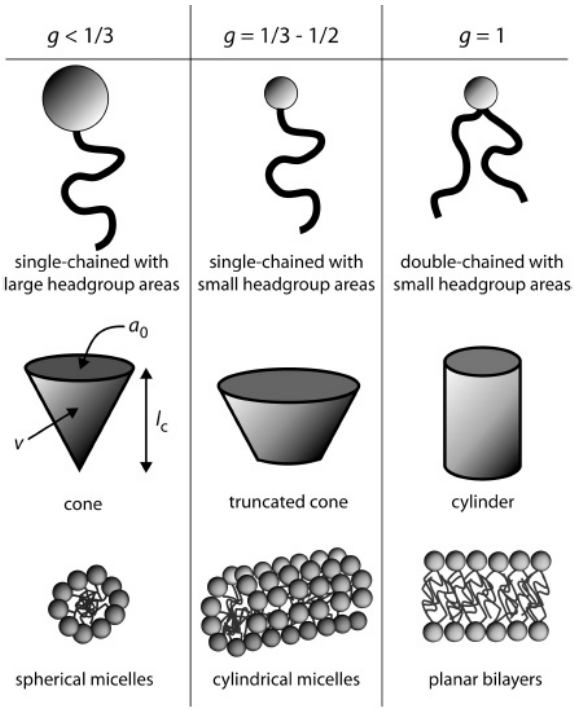

Figure 1.5: Examples of packing shapes and micellar aggregates formed by surfactants.

g	Symmetry
1/3	Cubic Pm3n
1/2	2d-hex p6mm
1/2 - 1/3	Cubic Ia3d
1	Lamellar

Table 1.2: Ordered mesophases corresponding to different packing factor values.

1.2.7 Types of hybrid interfaces: role of the polar head charge

Both surfactant and inorganic soluble species direct the synthesis of mesostructured MCM-41-type materials. The hybrid solids thus formed are strongly dependent on the interaction between surfactants and the inorganic precursors. In the case of ionic surfactants, the formation of the mesostructured material is mainly governed by electrostatic interactions. In the simplest case, the charges of the surfactant (S) and the mineral species (I) are opposite, in the synthesis conditions (pH). Two main direct synthesis routes have been identified: S^+I^- and S^-I^+. This notation has been introduced by Huo et al. to classify the interactions between the inorganic framework (I) and the surfactant (S); the + and - signs refer to their charge [15].

Two other synthesis paths, considered to be indirect, also yield hybrid mesophases from the self-assembly of inorganic and surfactant species bearing the same charge: counterions get involved as charge compensating species. The $S^+X^-I^+$ path takes place under acidic conditions, in the presence of halogenide anions (X^-, Cl^-, Br^-). For example, it is possible to obtain mesoporous silica working in acidic conditions, below the isoelectric point (pH<2), by adding a hydrogen halide such as HCl or HBr: in these conditions silica acquires a positive charge because the silanols become protonated as $Si(OH_2)^+$ [7]. Because the surfactant's cationic head group is surrounded by halogenide ions, the hybrid interface that forms is of type $S^+X^-I^+$, where the halogenide ions X^- form a negatively charged layer around the surfactant headgroups S^+, and the protonated silica I^+ hydrogen bonds to halogenide anions. Therefore, the latter serve as the mediating agents that connect the inorganic and the organic cations. As inorganic condensation proceeds, protons are expelled from the interface, together with halogenide ions, in order to maintain electroneutrality.

The $S^-M^+I^-$ route is characteristic of basic media, in the presence of alkaline cations (M^+, Na^+, K^+). The different possible hybrid inorganic-organic interfaces are schematized in Figure 1.6.

The products obtained using ionic surfactants have several drawbacks. First, the thickness of the inorganic wall (i.e. the distance between two adjacent pores) is so small (typically 8 to 13 Å) that it poses a serious limitation in terms of mechanical stability, especially for uses in catalysis. Second, ionic surfactants allow obtaining limited porosity (roughly 15 to 100 Å). Third, the strong electrostatic interactions between the surfactant and the inorganic framework are the cause for difficulty in surfactant extraction: high calcination temperatures are needed, which may cause

chemical degradation or collapse of the mesostructure; moreover, counterions (e.g. Na^+, K^+, Br^-, Cl^-) are not completely removed and remain as impurities in the final product.

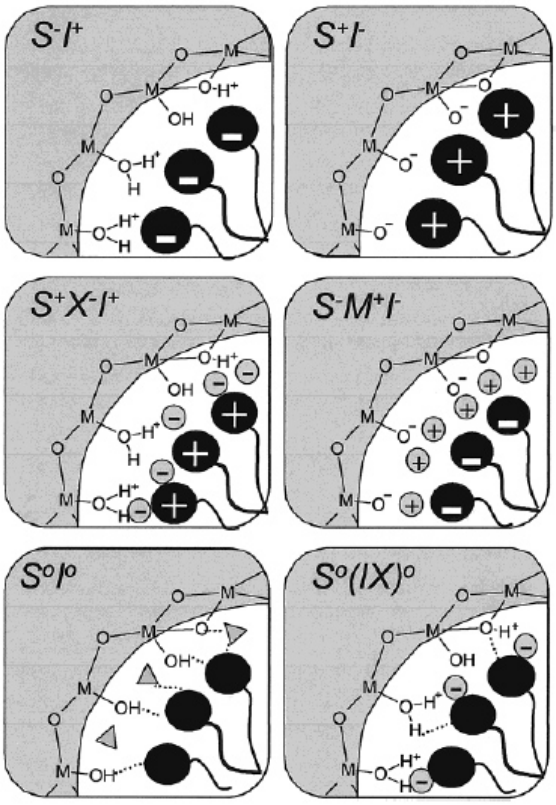

Figure 1.6: Schematic representation of the different types of silica-surfactant interfaces. S represents the surfactant molecule and I, the inorganic framework. M^+ and X represent the corresponding counterions. Solvent molecules are not shown, except for the I^0S^0 case (triangles); dashed lines correspond to H-bonding interactions.

Other synthesis routes were developed, which rely on non-ionic surfactants, where the main interactions between the template and the inorganic species are H-bonding or dipolar. In 1995 Pinnavaia et al. presented a new synthesis of mesoporous silica using a non-ionic surfactant [16]. Their approach was based on the formation of a HI through hydrogen bonds between the amino groups in the surfactant and the silanols in the partially hydrolysed precursor. This HI is denoted as S^0I^0 because there is no net electrostatic charge on the two phases constituting the HI. The mesoporous silica thus obtained was characterised by larger inorganic walls (around 1.7 nm), which give better mechanical stability. Moreover, removal of surfactant is less of a critical step because hydrogen bonds are more easily cleaved than electrostatic bonds. A major drawback of this first attempt is that the mesophase was not highly ordered, but rather made of disordered tubular cavities, a structure called “wormlike”. To date, amphiphilic block copolymers are the most important class of non-ionic surfactants used in the synthesis of mesoporous materials. Because the surfactants used in the experimental work presented in this thesis are amphiphilic block copolymers, they will be addressed more thoroughly in the next section.

1.2.8 Mesostructures templated by amphiphilic block copolymers

In a copolymer (or heteropolymer), two or more chemically different monomers are covalently linked in the same macromolecule, as opposed to a homopolymer, where only one type of monomer is used. In block copolymers (BC) the chemically different monomers are grouped in blocks, thus monomers within one block are alike and differ from the monomers belonging to the adjacent blocks.

Block copolymers whose blocks have different hydrophilic-hydrophobic properties are called amphiphilic block copolymers (ABCs). These belong to a family of macromolecular surfactants widely employed in industrial and households products, e.g. as foaming and dispersing agents, coatings, detergents. Regarding their use in the synthesis of mesoporous materials, ABCs present several advantages as compared to low molecular weight surfactants: (1) micelles are bigger and permit obtaining porous structures with pore sizes up to several tens of nanometres; (2) mesophase symmetry can be controlled by such parameters as nature of copolymer, solvent and co-solvent composition; (3) many ABCs with diverse chemical compositions, molecular weights and architectures are commercially available, or alternatively can be synthesised for specific purposes [17]. Table 1.3 shows three examples of ABCs used in the synthesis of mesoporous films, while Table 1.4 summarises the main aspects of ABCs, as well as the main differences with low molecular weight surfactants.

Name	Chemical formula
Brij	C_xEO_y $H–(CH_2)_x–(CH_2CH_2O)_y–H$ $x = 12, 16, 18$ $y = 2, 4, 10, 20$
Pluronic	$EO_xPO_yEO_x$ $HO–(CH_2CH_2O)_x–(CH(CH_3)CH_2O)_y–(CH_2CH_2O)_x–H$ x and $y = 20 – 100$
Tween	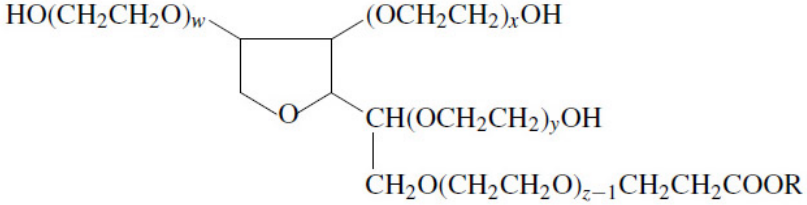 with $x + y + z + w = 20$ Tween 80: $R = (CH_2)_7CH=CH(CH_2)_7CH_3$

Table 1.3: Examples of the main families of amphiphilic block copolymers commercially available used in the synthesis of mesoporous materials.

Low MW surfactant	Amphiphilic block copolymer
Solution and mesophase behaviour	
Molecular / monodisperse	Polymeric / can be polydisperse
Head + chain structure object shape controlled by the *g* packing parameter	Enormous range of architecture: linear, branched, star, ... shape controlled by χ_{ij}, N, f_{ij} (i,j = 1...n)
Simple micelle-like or bicontinuous mesostructure	Possibility of complex multiscale mesostructures
Micellisation driven by hydrophilic-hydrophobic character	Micellisation driven by hydrophilic-hydrophobic character, block, size and conformation
Cosolvent swelling modifies curvature	Differential swelling of domains by cosolvents
Used in the design of mesostructured materials	
"Hard" well-defined hybrid interfaces	"Blurry" interfaces, possibly swollen by the inorganic phase
Thin walls (about 1 nm)	Thick walls (2-10 nm)
Walls not entangled with the template	Walls entangled with the template ("multiphase")
Pore size limited by micelle shape	Pore size tailorable modifying polymerisation degree, monomer nature, polymer fraction

Table 1.4: Key aspects of low molecular weight surfactants and block copolymers.

Self-assembly of block copolymers can be regarded as a phase separation whose driving force lies in the chemical incompatibility between the chemically different blocks. The entropy of mixing per unit volume of chemically different high molecular weight A_n and B_n homopolymers is generally small, and it scales inversely with molecular weight, so even small structural differences between A and B contribute to increasing the free energy and result in phase separation. The parameter used to estimate immiscibility is the so-called Flory-Huggins interaction parameter:

$$\chi_{AB} = \left(\frac{Z}{k_B T} \right) \left[\varepsilon_{AB} - \frac{1}{2} \left(\varepsilon_{AA} + \varepsilon_{BB} \right) \right]$$

which gives an indication on the increase in the Gibbs free energy when two A and B monomers are in contact, expressed in thermal energy units, k_BT. Z is the number of nearest neighbour monomers and ε_{AB} is the interaction energy between A and B monomers. Positive χ_{AB} values indicate a repulsion between A and B, thus contributing to phase separation, whereas a negative χ_{AB} indicates a favourable entropic term towards miscibility. When there are no significant A–B interactions (as in the case of hydrogen or electrostatic interactions) χ_{AB} is positive (a typical value is 0.1). χ_{AB} also scales inversely with temperature, therefore higher temperatures favour mixing.

In amphiphilic block copolymers, the different A and B units are covalently linked, therefore long-range hydrophobic-hydrophilic repulsion and short-range covalent attraction coexist. Indeed, these are competitive forces that are the basis of the formation of aggregated self-assembled structures.

Microphase separation theories make large use of a simple parameter in order to quantify the driving force leading to ordered phases, that is $N\chi$, where N is the polymerisation degree and χ is the sum of χ_{AB} over all A and B monomers. $N\chi$ can give an idea of the segregation degree of the block copolymer: when $N\chi \leq 10$ the system is governed by entropic terms and a disordered phase is formed; when $N\chi > 10$, enthalpic terms prevail and a disorder-to-order transition is observed [18]. We also need a parameter to take into account geometric factors: for a di-block A–B copolymer, the parameters f_A and f_B describe the copolymer's composition, where $f_A = N_A/N$, $f_B = N_B/N$, $f_A + f_B = 1$. Strictly speaking, in block copolymer-based systems the self-assembled mesophase symmetry is not predictable on purely geometric grounds, in that one has to take into account also chemical and structural factors, expressed by the terms χ_{ij}, N, f_{ij}, where i and j vary with the number of blocks (for a di-block copolymer i=A, j=B).

Other effects must be considered in order to formulate a comprehensive predictive theory. In order to maximise the distance between incompatible blocks, the organic chains adopt stretched configurations, which generate a restoring force (analogous to Hooke's law, but entropic in origin). For a block constituted by N monomers in a stretched configuration and spaced by R, this force can be expressed as:

$$F_e = \frac{3k_B T R^2}{2Na^2}$$

where a is a characteristic length of the monomer which depends on the local chain structure.

Finally, the aggregation number Z can be defined as the number of macromolecules that concur in micelle formation. Experimental results yield an empirical law:

$$Z = Z_0 N_A^{\alpha} N_B^{-\beta}$$

where Z_0 is a constant depending on the type of copolymer, N_A and N_B are the polymerisation degrees for blocks A and B, α and β are equal to 2 and 0.8, respectively (with slight variations according to the system). This equation can describe the aggregation number for di- and tri-block, graft and star copolymers. Besides, it holds also for ionic and non-ionic small molecular weight surfactants.

To summarise, the stability of different morphologies in a block copolymer solution is the result of multiple enthalpic (interaction of incompatible blocks) and entropic (chain stretching, spatial frustration) contributions to the Gibbs free energy. It can be described by the parameters χN (tendency towards block segregation) and f (chemical composition). Simulations obtained by self-consistent field theory allow calculating the free energy of block copolymer solutions according to their composition, and they are generally in good agreement with experimental data. Nevertheless,

to a first approximation, simpler geometric parameters like the packing factor *g* can be used in order to get a rough indication about which micelle shape the system will preferentially form.

The degree of complexity of the structures formed by block copolymers increases dramatically as the number of different blocks *N* increases. In di-block copolymers, χ_{AB}, *N* and *f* are generally sufficient to univocally determine the phase diagram, whereas in tri-block copolymers a larger number of parameters must be known: at least three interaction parameters (χ_{AB}, χ_{BC}, χ_{AC}) and two compositional parameters (f_A, f_B). Moreover, other factors are introduced, which depend on copolymer architecture, for example branching, side groups, etc. As a consequence, whereas in di-block copolymers only hexagonal, cubic, lamellar structures are typically observed, in tri-block copolymers diverse and more exotic symmetries are experimentally found. As *N* is increased, the complexity of the structure increases exponentially.

Experimental data show that a variety of structures that are not predicted by this model can be obtained from the same copolymer. Experimentally, it can be noted that a solvent that has a selective affinity for one block can vary the range of stability of the predicted structures, or produce new ones. This can be explained by the selective volume increase of one block and the subsequent change in micelle curvature.

Ivanova et al. [19] presented the study of Pluronic P105 block copolymer (EO_{37}-PO_{58}-EO_{37}) in the presence of selective solvents. This copolymer should give lamellar structures, as the PEO:PPO weight ratio is 1:1. However, as water concentration is raised, PEO blocks are selectively swelled, therefore a planar interface becomes unfavoured and micelles with finite curvature form: the system responds to progressively higher water concentration by forming cylindrical micelles with 2d-hex packing (49–68 wt% P105), and spherical micelles with cubic symmetry (25–46 wt% P105). A further degree of freedom can be provided by a selective co-solvent. In the work cited, three co-solvents are chosen according to their different polarity: ethanol (CH_3CH_2OH), propylene glycol (CH_2OH-$CHOH$-CH_3) and glycerol (CH_2OH-$CHOH$-CH_2OH). Small-angle X-ray scattering (SAXS) measurements point out that, although all three co-solvents are polar and are miscible with water, they are localised in different domains in the mesophase: glycerol is localised in polar micro domains far from the PEO-PPO interface, whereas propylene glycol and ethanol partially swell the PEO or PPO blocks. This causes a decrease in lattice constant and a different micelle curvature.

In 1998, Stucky's research group at Santa Barbara, CA, was the first to report the use of non-ionic tri-block copolymers of poly(ethylene oxide)-poly(propylene oxide)-poly(ethylene oxide) (PEO-PPO-PEO) as the templating agents in the synthesis of mesoporous silica [20]. Pore sizes were as high as 30 nm when Pluronic surfactants were employed. Since the pH was below the isoelectric point of silica (pH<2) the silica precursors were positively charged, and the hybrid interface can be

described as $(S^0H^+)(X^-I^+)$, where the water-surfactant interaction is due to hydrogen bonds between the oxygen atoms in PEO blocks and the hydrogen atoms in water.

The interactions between block copolymers and inorganic precursor have a central role in the formation of the hybrid NBBs that will self-assemble to form the ordered mesostructure [21]. Hydrogen bonds between the polyether group $-[CH_2\text{-}O\text{-}CH_2]_n-$ of the hydrophilic PEO blocks and the polar solvent molecules are responsible for attractive interactions between the copolymer and the polar solvent. The hydrophobic character of PPO block can be explained by the presence of a methyl side group, which prevents the formation of a PEO-water hydrogen bond because of its steric hindrance. Thus, micelles have a central PPO hydrophobic core and a hydrophilic corona made of PEO and inorganic species.

Melosh et al. have determined that in silica monoliths templated by Pluronic F127 self-assembly occurs at F127 concentrations higher than 40 wt%. The lack of order at lower concentrations leads to the conclusion that strong, hydrogen bond-like interactions are formed between Si-O-Si oligomers and both PEO and PPO polyethers, as pointed out by NMR data. As long as F127 concentration is low, these interactions inhibit microphase separation and a nearly homogeneous mixture of block copolymer in the silica network is observed. When surfactant concentration is raised, PPO-PPO (surfactant-surfactant) interactions prevail over hydrophobic PPO-SiO_2 (surfactant-inorganic) interactions, resulting in phase separation and increase in the degree of order [22]. In all examined cases, a strong interaction was observed between the PEO block and the silica polymer.

Besides playing a major role in determining the formation of the HI, the interaction between silica species and PEO blocks are responsible for the creation of micro-porosity in the final mesoporous material. In fact, when the silica-PEO interaction is strong, the hydrophilic blocks will be partially or totally interpenetrated with the inorganic phase. Considering a PEO-PPO block copolymer, three scenarios can be discerned according to the entity of the interactions at the hybrid interface (Figure 1.7).

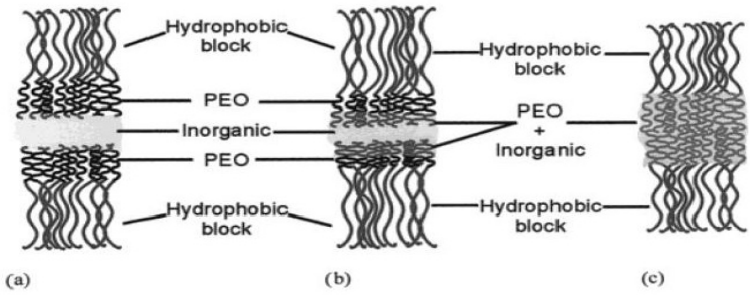

Figure 1.7: Three possible structures of a hybrid material composed of an inorganic phase and a nonionic amphiphilic block copolymer with PEO as the hydrophilic block. (a) Three-phase system (i.e. inorganic, PEO, and hydrophobic block), (b) gradual transition from a two-phase to a three-phase system, and (c) two-phase system (PEO/inorganic and hydrophobic block).

(1) PEO blocks form a layer interposed between the inorganic phase and the PPO core (three-phase model). (2) PEO chains totally interpenetrate the inorganic phase (two-phase model), where each single PEO chain functions as a single macromolecule template and yields a micropore upon calcination. (3) The PEO chains interpenetrate the inorganic network according to the three-phase model until saturation is reached, and phase separation occurs according to the two-phase model; in this case both micro-porosity and an increase in pore size are observed (mixed model).

Recent work in silica and titania mesostructured films [23] showed that it is possible to obtain different phases by varying the template/silica volume fraction ($V_{TS}=V_{templ}/(V_{templ}+V_{SiO2})$). This offers an advantage in that the synthesis design can be based upon surfactant/solvent rather than on much more complicated surfactant/silica/solvent phase diagrams. One can design the synthesis of a mesostructured film by: (1) locating the surfactant concentration for the desired mesophase in the surfactant/solvent phase diagram, (2) using this concentration as V_{TS}, (3) calculating the quantity of surfactant V_{templ} to introduce in the coating solution (obtained from the equation of V_{TS} defined above).

However, the solvent role is indeed important. Recent work in oriented silica membranes [24] reveals that worm-like or hexagonal phases can be obtained in conditions where cubic phases are expected (V<70% for F127 [25]). In these 'silicatropic' hybrids, the final mesostructure can be tailored by the water contents in solution (h), at a constant V_{TS}. The crucial role of h can be envisaged as follows: the mesostructure is not only directed by the V_{TS}, but also by the amount of the silica–template interface. Water helps to 'fold' the template in a more curved form [26], but also generates more hydrophilic silanol ends. A more hydrophilic HI (water/inorganic) tends to maximize interactions with the hydrophilic block, and enhance curvature.

1.3 Mesoporous silica films

The first mesoporous materials were synthesised in the form of powders through precipitation mechanisms. These materials were useful in applications such as catalysis and sorption, but when other applications were devised, such as sensors and low dielectric constant interlayers (due to the ordered nanometric porosity and the high specific surface area of as much as ~1000 $m^2 \cdot g^{-1}$), they opened the way to the synthesis of mesoporous films.

If one considers the publications on mesoporous films, one can note that siliceous systems constitute the largest part. The reasons are manifold: (1) there is a historical reason, as many researchers come from the zeolite world and as such they are much more familiar with the silicon

and the aluminium chemistry rather than, say, transition metal chemistry; (2) silica films obtained by sol-gel routes are less problematic with respect to other oxides, because the self-assembly process can be controlled more easily due to low hydrolysis-condensation rates of silica precursors (e.g. alkoxides, chlorides); (3) the stability of the Si-C bond opens several perspectives on hybrid organic-inorganic materials, as well as on the possibility of grafting a number of chemical functionalities on the mesopore surface due to the presence of Si-OH groups.

1.3.1 Evaporation induced self-assembly

To date, the most widely employed technique in the synthesis of mesoporous films is: evaporation-induced self assembly (EISA). This definition was coined by Brinker and co-workers in 1999 to indicate a new synthesis process where mesophase formation is triggered by solvent evaporation rather than precipitation reactions [27]. The starting point in the EISA technique is the preparation of a dilute solution containing the inorganic precursors (generally a metal/metalloid alkoxide or salt) and the organic templating agents (surfactant or macromolecular amphiphilic block copolymers). The solvent is an alcohol (generally ethanol or methanol) and small amounts of water may be added. EISA is most often used in combination with the dip-coating deposition technique (or, less frequently, with spin-coating). In dip-coating, a substrate is dipped into the solution and extracted at a constant speed (typically, few $mm \cdot s^{-1}$). Due to the solution-substrate wettability, a liquid layer is formed on the substrate, whose thickness depends on the extraction speed and the viscosity of the solution. As the solvent evaporates from the liquid layer, the inorganic precursors undergo condensation and cross-linking processes, thus forming a gel, which can be defined as a phase constituted by a more or less condensed inorganic network within which residual solvent molecules form an interconnected liquid phase. In spin-coating, few drops of the precursor solution are placed on a substrate, which is then spinned at a constant angular speed (typical values: few thousands of rpm). Thus, a homogeneous film is spread on the substrate due to the centrifugal force. Because films were prepared exclusively by dip-coating in this doctorate work, we will refer to this deposition technique.

In the EISA technique, solvent evaporation occurring in the first seconds after deposition causes an increase in the concentration of non-volatile (organic and inorganic) species in the film. This triggers both self-assembly and inorganic cross-linking, which therefore act concurrently. Thus, evaporation is not the driving force for self-assembly as such, but rather keeps the system on a pathway where self-assembly can occur during film formation. A more thermodynamic synthetic control allows for the formation of better ordered mesostructures, whereas an increasing kinetic control leads to the formation of ill-defined or disordered mesostructures. The complexity and the

rapidity of the concurring phenomena during solvent evaporation justify what is commonly defined race towards order: indeed, it is a sort of challenge in that the organic phase must form an ordered self-assembled mesophase before inorganic polycondensation stops it. That is why one needs to decrease inorganic reactivity, for example adjusting the pH near to the isoelectric point. Thermal treatments can follow the deposition step in order to promote further condensation, mechanically stabilise the mesostructure and remove the surfactant (Figure 1.8).

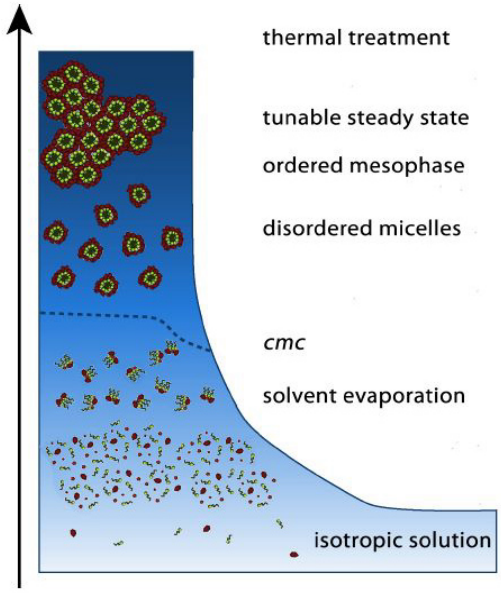

Figure 1.8: Scheme of the formation of a mesostructured film by evaporation-induced self-assembly. The arrow indicates the time line. Step 1: In the isotropic solution condensation is slowed down and the non-volatile precursors are free surfactant molecules and inorganic oligomers. Step 2: Solvent evaporation triggers the formation of surfactant-inorganic units. Step 3: Evaporation is complete and the film equilibrates its water content with the environment. Step 4: The thermal treatment stabilises the mesostructure.

Further operations that may be performed on films include chemical grafting of functional groups or molecules on the mesopore surface in order to change the physicochemical properties (e.g. grafting of organic groups in order to increase hydrophobicity) or the functional properties (e.g. inclusion of metallic [28] or semiconductor [29] nanoparticles within the mesopores for photocatalysis and sensing). To summarise, a reproducible synthesis of mesoporous materials via EISA requires control on three levels: (1) chemical composition of the precursor solution, (2) deposition process, (3) post-treatments performed on the film. The remainder of this section tackles these synthetic and processing parameters.

1.3.2 Precursor solution

Solvent. The choice of solvent must meet at least three requirements: (1) the solution must completely wet the substrate in order to ensure good film homogeneity; (2) the solvent must be volatile to promote a fast increase in concentration of the non-volatile species; (3) it must be a good

solvent for the organic and inorganic precursors. Generally, ethanol is the preferred choice, as it can wet both hydrophilic and hydrophobic substrates, it is volatile, and it can easily dissolve amphiphilic block copolymers as well as inorganic alkoxides and metal salts. An organic additive can be used to selectively swell a region of the block copolymer causing a change in micelle shape and volume.

Inorganic precursors. In the synthesis of mesoporous silica, alkoxysilanes such as tetraethoxysilane (TEOS) are widely employed. Small quantities of an organically-substituted alkoxysilane, called organo-alkoxysilane, may be added to TEOS. In organo-alkoxysilanes one or more hydrolysable groups are substituted by organic groups which are not hydrolysable due to the high stability of the Si-C bond. Therefore, these organic groups eventually end up covalently linked to the final inorganic framework, and a wide variety of mesoporous or mesostructured hybrid organo-silica products can be obtained. Inorganic reactivity can be controlled by varying the pH. This is most clear in silicon alkoxides: less ordered mesophases are obtained at high pH values (5–7), where condensation is fast and prevails over mesostructure formation. A low pH favours hydrolysis and inhibits condensation, therefore permitting a better mesostructure organisation. Working in high dilution conditions, silica condensation is further inhibited and the solution is very stable in time (up to several months).

Water. This is truly a multipurpose component of the precursor solution. In silica-based systems it takes part in alkoxide hydrolysis and condensation. For small values of h=[H_2O]/[Si], no mesostructure or a wormlike mesophase forms, whereas too high h values may lead to uncontrolled condensation and poor order. A typical value found in the synthesis of silica is h=5–10, which is relatively independent of the type of inorganic precursor (a silicon alkoxide or a salt). Water molecules are adsorbed on the hydrophilic crown of the micelles, increasing the hydrophilic head-group area and thus decreasing the geometric packing factor g. In this way an increase in hybrid interface curvature is observed and the formation of spherical micelles rather than cylindrical is favoured. Besides, water favours the formation of silanols at the hybrid interface which contribute to strengthening the interactions between inorganic precursors and surfactant. In general, the role of water at the hybrid interface is of key importance in the synthesis of all mesostructured films.

Structure-directing agent. The choice of type and quantity of surfactant has been shown to be a key parameter in order to obtain a final mesostructure with a given symmetry. Parameters that have to be taken in to account to predict the final mesostructure symmetry are the packing factor g and the surfactant volume fraction. Such parameters can be overwhelmed by other factors, as the water content in the solution, relative ambient humidity, evaporation rate and presence of solvent with different polarity. In particular, the amount of relative humidity is crucial in determining

mesostructure formation, in that it can diffuse from the environment into the film, affecting the interactions at the hybrid interface and exerting a critical role on micelle curvature. Furthermore, the presence of solvents other than those reported in the phase diagrams can influence the chemistry of these systems, and mesophase symmetries different than those reported in the phase diagram can be formed. Finally, EISA synthesis conditions are dramatically affected by kinetic factors, whereas a phase diagram refers to a system in its thermodynamic equilibrium. Polycondensation increases film viscosity and reduces micelle mobility, therefore the mesophase in a film is typically in a metastable state, out of thermodynamic equilibrium. In practice, the molar ratio s=[surfactant]/[inorganic] is generally reported in research works rather than the surfactant/inorganic volume fraction. In fact, s is considered more as a heuristic parameter, often determined through educated guesses in a trial-and-error fashion, where different quantities of surfactant are systematically varied, and the characterisation of the films thus obtained are used as a feedback to formulate a "working recipe". The s values are on the order of magnitude of 0.01 for ionic surfactants, whereas for high MW block copolymers (e.g. Pluronic type) they can be as low as 10^{-3} or 10^{-4}.

Catalyst. When an alkoxide is used as the inorganic precursor, a catalyst increases the kinetics of hydrolysis or condensation. There is a fundamental difference between basic and acid catalysts, in that the former favour hydrolysis and inhibit condensation, whereas the latter favour condensation and inhibit hydrolysis [7]. In the synthesis of mesoporous films, an acid catalyst is generally used, as it ensures good quality and homogeneity of the film. In particular, HCl is the choice in most cases as its high volatility ensures full evaporation once its function is not required any more and therefore it does not remain in the film as impurity. Furthermore, its evaporation causes the pH inside the film to increase, which favours condensation reactions, stiffening the mesostructure.

Ageing. Hydrolysis and polycondensation reactions of inorganic precursors in the coating solution cause the formation and growth of oligomeric species (NBBs). In the case of silica, these can be constituted by cyclic, linear or branched structures, depending on the composition and pH. The size of these oligomers increases as a function of time. Because the size of these NBBs is critical in mesostructure formation, it is of crucial importance to control ageing of the coating solution (identified as the time interval between preparation of the solution and its use in the dip-coating). Experimental results have demonstrated that ageing is a critical parameter which can affect deeply the degree of order of the final mesostructure. Structural information on silica oligomers can be inferred from ^{29}Si NMR measurements on solutions. The notation Q_i is generally adopted, where i represents the number of O atoms bonded to a single Si atom and $0 < i < 4$. Grosso et al. have observed a trend in Q_i concentration depending on the solution (TEOS, CTAB, HCl, H_2O in EtOH)

ageing time. This trend was compared to the degree of order of the final mesostructure in films obtained by dip-coating with the aged solutions. The most ordered mesostructures are observed when the concentration of Q_2 and Q_3 is highest, corresponding to an ageing time of 6–7 days [31]. Too long an ageing leads to the formation of large silica oligomers that are not capable of accommodating the curvature at the hybrid interface during mesophase formation, whereas too short an ageing does not result in the formation of well-defined NBBs, which again leads to poor order.

1.3.3 Film deposition

The film deposition step is no less critical than the preparation of the precursor solution, because in this stage inorganic condensation and self-assembly take place, driven by the local thermodynamic and kinetic conditions and ultimately triggered by the fast evaporation of the solvent. It has been suggested that the depart of solvent from the film-air interface causes an increase in concentration of the inorganic and the organic non-volatile species, which undergo self-assembly and condensation reactions and form a mesostructure. As the rate of evaporation is faster at the film-air than at the film-substrate interface, non-volatile species become more concentrated in the former than in the latter regions, triggering diffusive processes due to the concentration gradient within the film. Therefore, while solvent evaporates, the composition of the film is not univocally determined, but rather there exist several compositions in different regions, which constantly evolve with time until most solvent is evaporated.

Though it is practically impossible to calculate the exact composition as a function of space and time, there is one phenomenon that can give insight on what occurs within the film during the evaporation process: mesophase transition. Performing in situ small angle X-ray scattering (SAXS) measurements during dip-coating, one can obtain a time-resolved sequence of diffraction patterns which inform us on the structural evolution of the forming mesophase. The sequence: lamellar phase - 3d hexagonal - cubic is typically observed, corresponding to the sequence: isotropic – spherical micelles - cylindrical micelles - lamellar phase observed in the surfactant-solvent phase diagram for increasing concentrations [30].

Different mesophases can be obtained by varying solvent evaporation rate. For high evaporation rates, the simultaneous presence of different mesophases can be observed, an effect that can be ascribed to different compositions at different depths caused by high concentration gradient: since evaporation occurs at the film-air interface, non-volatile concentration is higher in this region, thus giving an ordered phase sooner than in the region close to the substrate. As different compositions generally correspond to different stable symmetries in the phase diagram, different or overlapped

diffraction patterns are observed. Where solvent is less present (close to the film-air interface) inorganic condensation may form a solid barrier that prevents further evaporation, thus multiple mesostructures are likely to be "frozen" in their metastable states: an ordered structure is formed near the surface and a wormlike or totally disordered region within the film.

There is evidence that structural rearrangements in the mesophase occur even long after the solvent evaporation step. Experimentally, in situ SAXS measurements point out that mesophase transitions can be induced by the external environment well after solvent evaporation, most typically by a variation in relative humidity (RH). Mesophase transitions reflect structural rearrangements in mesophase architecture, which are observed to be reversible as long as the film viscosity is low (i.e. as long as the inorganic network has a low degree of cross-linking). Therefore, we can identify a time interval between film deposition and when inorganic condensation hinders mesophase rearrangements, this latter represents a broad time interval itself since inorganic condensation is a continuous process, in which kinetics varies according to the system in question. If RH is sufficiently high, water is encouraged to stay inside the film, or a diffusive motion occurs from the environment into the coating. Water is preferentially localised in the hydrophilic part of the film, i.e. on the hydrophilic coronas of micelles and in between. During this dynamic equilibrium state, condensation progressively takes place, stabilising the inorganic framework around the spherical micelles and avoiding further phase transitions when the viscosity is too high. This state of as-deposited mesostructured films is called tuneable steady state (TSS). This time interval depends on the chemical composition of the film and may last up to few hours.

Because the amount of water in a film depends critically on RH, it is useful to derive a relation between them, especially if an estimate of V_{inorg} is needed in order to calculate the copolymer volume fraction. This is often accomplished by resorting to experimental techniques; unfortunately, the quantity of matter in films is too low, so determining the total volume fraction of water is a difficult task and other systems than thin films are used. Indicatively (and for the system studied by the authors) a correspondence between RH and water content expressed as h=[H_2O]/[Si] can be found, corresponding to h=0.5, 4, 7 for RH=20%, 40%, 70%, respectively.

There is a direct proportion between film thickness and the speed at which the substrate is extracted from the solution (pulling rate) in the dip-coating process. It is due to surface tension effects occurring at the solution-film-air interface, which become less critical when extraction speed is increased. In terms of mesostructure order, a lower degree of order is generally observed when extraction speed is increased. This can be explained considering that condensation is fastest at the film-air interface (*vide supra*): a high concentration gradient is set up and further evaporation from the bottom of the film is inhibited if the topmost layer is too cross-linked [31].

1.3.4 Thermal treatment

Thermal treatment has the double purpose of promoting inorganic condensation and decomposing the organic phase in order to free the mesopores (calcination). Generally, mild treatments with thermal ramps and steps are preferred: abrupt treatments at high temperatures may cause mechanical stress in the sample which can damage the mesostructure and lead to macroscopic cracking. A phenomenon that is always observed is thermal shrinkage: because the film is pinned to the substrate, the contraction occurs exclusively along the direction perpendicular to the substrate (out of plane), whereas the contraction parallel to the substrate (in plane) is negligible. As a consequence, calcination somewhat alters the shape of mesopores: this is evident in spherical pores, which become oblate spheroids.

CHAPTER 2

In-situ characterisation techniques

The phenomena leading to the formation of a mesostructured film can be divided into (1) chemical reactions and physical processes in the precursor solution, (2) intermediate liquid-solid state at the onset of polycondensation and self-assembly, (3) tuneable steady state, thermal treatment and final product. It is evident that discontinuous ex-situ techniques can be used to sample only a part of the global self-assembly process. However, because mesostructure formation occurs during dip-coating and is often a matter of seconds rather than minutes or hours, the study of this part requires the use of in-situ techniques with special configurations. This study plays a central role to understand thoroughly the physics and chemistry underlying templated self-assembly in mesostructured films. Because a description of all characterisation techniques utilised in the research on mesostructured materials falls outside the scope of this thesis, the present chapter provides both theoretical and technical information on the in-situ techniques employed in the experimental part of this doctorate work.

2.1 Small angle X-ray scattering

2.1.1 X-ray diffraction

One of the most used techniques to carry out structural characterisation of solid materials is X-ray diffraction. When an electromagnetic wave impinges on the sample, it interacts with the electron clouds and undergoes elastic scattering phenomena. If the electron density is arranged periodically, as in a crystal lattice, the scattered waves add up and give constructive and destructive interference, and their intensity is recorded by a detector as a function of the exit angle. Diffraction effects are generally only noticeable for waves whose wavelength is of the order of the feature size of the diffracting objects, thus for crystal lattices with periodicity on the order of the Å, X-rays are used.

A visual way to rationalise X-ray diffraction by an ordered crystal lattice is provided by the so-called Bragg's interpretation. A given crystal is constituted by regular arrays of atoms spaced by fixed distances d. The crystal can be decomposed into any number of different planes, due to the periodicity of the crystal lattice. As the wave enters the crystal, some portion of the wave is

reflected by the first layer, while the rest continues through to the second layer, and so on. By the definition of constructing interference, the separately reflected waves remain in phase if the difference in the path length of each wave is equal to an integer multiple of the wavelength. This condition is expressed by the well-known Bragg's law:

$$2d_{hkl}\sin\theta = m\lambda \tag{2.1}$$

where d_{hkl} is the periodicity of a given family *hkl* of planes (d-spacing), θ is the incidence and exit angle, *m* is an integer and λ is the wavelength. Let us now examine in detail the physics of X-ray diffraction by a crystal [32].

The electron density in a periodic lattice *n*® is invariant under lattice translation, so that $n(\mathbf{r})=n(\mathbf{r}+\mathbf{R})$, where $\mathbf{R}=u_1\mathbf{a_1}+u_2\mathbf{a_2}+u_3\mathbf{a_3}$ is a vector of the crystal lattice which indicates the periodicity of crystallographic planes, $\mathbf{a_1},\mathbf{a_2},\mathbf{a_3}$ are the base vectors in the direction of the three crystal axes, and u_1,u_2,u_3 are integers. The density function $n(\mathbf{r})$ can be represented as a Fourier series:

$$n(r)=\sum_G n_G \exp(iG\cdot r) \tag{2.2}$$

It can be demonstrated that the set of Fourier coefficients $n_{\boldsymbol{G}}$ is

$$n_G = V_C^{-1}\int_{cell} dV n(r)\exp(-iG\cdot r) \tag{2.3}$$

where V_c is the volume of a cell of the crystal. The vectors **G** of the Fourier sum in Equation 2.2 are described by $\mathbf{G}=v_1\mathbf{b_1}+v_2\mathbf{b_2}+v_3\mathbf{b_3}$, where v_1,v_2,v_3 are integers and the axis vectors $\mathbf{b_1},\mathbf{b_2},\mathbf{b_3}$ are expressed by:

$$b_1 = 2\pi\frac{a_2\times a_3}{a_1\cdot(a_2\times a_3)} \tag{2.4}$$

Each vector defined by Equation 2.4 is orthogonal to two axis vectors of the crystal lattice, thus $\mathbf{b_i}\cdot\mathbf{a_j}=2\pi\delta_{ij}$ The vector **G** is the reciprocal lattice vector: every crystal structure has both a crystal lattice and a reciprocal lattice associated with it, which describes the periodicity of matter according to a Fourier sum (Equation 2.2). The reciprocal lattice, therefore, can be seen as the lattice in the Fourier space associated with the crystal, and each point in the reciprocal lattice corresponds to a set of lattice planes (*hkl*) in the real space lattice. The reciprocal lattice itself is a Bravais lattice: the direction of the reciprocal lattice vector corresponds to the normal to the real space planes, and the magnitude of the reciprocal lattice vector is equal to the reciprocal of the interplanar spacing of the real space planes.

From Equation 2.2, and considering an invariant crystal translation $\mathbf{R}=u_1\mathbf{a_1}+u_2\mathbf{a_2}+u_3\mathbf{a_3}$ it follows that

$$n(r) = n(r+R) = \sum_G \exp(iG \cdot r)\exp(iG \cdot R) \tag{2.5}$$

The exponential can be expressed using vectors of the direct ($\mathbf{a_i}$) and the reciprocal lattice ($\mathbf{b_i}$):

$$\exp(iG \cdot R) = \exp[i(v_1 b_1 + v_2 b_2 + v_3 b_3) \cdot (u_1 a_1 + u_2 a_2 + u_3 a_3)] = \exp[2\pi i(v_1 u_1 + v_2 u_2 + v_3 u_3)] \tag{2.6}$$

The argument of the exponential is $2\pi i$ times an integer, being the sum of products of integers, therefore:

$$\exp(iG \cdot R) = 1 \tag{2.7}$$

An incident wave $\exp(i\mathbf{k_i}\cdot\mathbf{r})$ of wavevector $\mathbf{k_i}$ is coherently scattered by a diffusion centre (i.e. electron density) and the scattered wave $\exp(i\mathbf{k_f}\cdot\mathbf{r})$ emerges with a wavevector $\mathbf{k_f}$. The scattering vector, or momentum transfer, is defined as:

$$\mathbf{q} = \mathbf{k_f} - \mathbf{k_i} \tag{2.8}$$

The amplitude F of the wave scattered from a volume element is proportional to the integral over the crystal of $n(\mathbf{r})$dV times the phase factor $\exp[i(\mathbf{k_i} - \mathbf{k_f})\cdot\mathbf{r}]$, therefore:

$$F = \int dV n(r)\exp[i(k_i - k_f)\cdot r] = \int dV n(r)\exp(-iq \cdot r) \tag{2.9}$$

We introduce the Fourier components of $n(\mathbf{r})$ (Equation 2.2) into Equation 2.9 to obtain:

$$F = \sum_G \int dV n_G \exp[i(G - q)\cdot r] \tag{2.10}$$

From Equation 2.10 it follows that the scattering amplitude is maximum when $\mathbf{q}=\mathbf{G}$, in other words there is diffraction when the momentum transfer vector is a vector of the reciprocal lattice. Therefore, a diffraction pattern of a crystal is a map of the reciprocal lattice of the crystal, and by recording the diffracted intensity as a function of the exit angle, we sample a region of the reciprocal lattice.

In elastic scattering the energy of the incident wave is conserved, so that the magnitudes k_i and k_f are equal, thus $k_i^2 = k_f^2 = k^2$. From this and from Equation 2.8 it follows that $(\mathbf{k_i}+\mathbf{G})^2 = k_f^2$, or

$$-2k \cdot G = G^2 \tag{2.11}$$

which is called the von Laue diffraction condition.

It can be demonstrated [33] that the vector $\mathbf{G} = h\mathbf{b_1} + k\mathbf{b_2} + l\mathbf{b_3}$ is perpendicular to (hkl) planes, and that $d_{hkl} = 2\pi/|\mathbf{G}|$. As a consequence, and because $k = 2\pi/\lambda$, Equation 2.11 may be written as:

$$2\,|k|\,|G|\cos(\pi - \theta) = 2kG\sin\theta = G^2 \Rightarrow 2\frac{2\pi}{\lambda}\sin\theta = \frac{2\pi}{d_{hkl}} \tag{2.12}$$

which is the Bragg condition for diffraction (Equation 2.1): $\lambda = 2d_{hkl}\sin\theta$.

Let us now consider a sphere drawn in the reciprocal space, centred on the origin of the incident wavevector $\mathbf{k_i}$ of radius $k = 2\pi/\lambda$, so that it passes through the origin O of the reciprocal space. According to Equation 2.11, there will be some wave vector $\mathbf{k_f}$ satisfying the von Laue condition

($\mathbf{q}=\mathbf{k_f}-\mathbf{k_i}=\mathbf{G}$) if and only if some reciprocal lattice point (other than the origin *O*) lies on the surface of the sphere. In this case we have diffraction, and we observe a Bragg reflection from the family of direct lattice planes perpendicular to that reciprocal lattice vector **G**. The sphere construction is called the Ewald construction, and the sphere is called the Ewald sphere. It can be noted that $q/2=k\sin\theta$, therefore $q/2=2\pi/\lambda \sin\theta$, which, considering Equation 2.1, becomes $q=2\pi/d$. The factor 2π is often dropped in the crystallographer's notation, so that $\exp(2\pi i\mathbf{G}\cdot\mathbf{R})=1$, and we have:

$$q = \frac{1}{d} \tag{2.13}$$

This is a simple relation between the scattering vector and the d-spacing of reflection *hkl*.

2.1.2 Small angle X-ray scattering on mesostructured films at synchrotron facilities

The periodicity considered so far, described by the electron density function $n(\mathbf{r})$, was assumed to be due to the ordered disposition of atoms in a crystal lattice. However, in principle nothing prohibits us from considering $n(\mathbf{r})$ as any electron density periodicity, invariant under a given lattice translation $n(\mathbf{r})=n(\mathbf{r}+\mathbf{R})$. Mesostructured materials are no exception, in that the ordered arrangement of the mesophase provides an electron density contrast between the inorganic and the organic phase which can be described by $n(\mathbf{r})$. The same holds for mesoporosity, where $n(\mathbf{r})$ describes the periodicity of the inorganic walls. As a consequence, the interaction of X-ray radiation with mesostructured and mesoporous materials gives diffraction and information on the symmetry of the ordered mesophase can be inferred. Since the feature size of a mesostructure is typically ~10 nm, using incident X-rays of wavelength ~1 Å will give diffraction at 2θ angles in the range 0.1–1°. On this principle are based small-angle X-ray scattering (SAXS) techniques. The "small-angle" refers to the angular range of the scattered beams, containing information on the structure in the reciprocal space in the nanometre range.

SAXS on mesostructured materials is often performed at synchrotron facilities. A synchrotron is a particular type of cyclic electron accelerator in which the magnetic and the electric fields are carefully synchronised with the travelling particle beam. Electrons are accelerated to high speeds in several stages to achieve a final energy that is typically in the GeV range. The electrons are stored in an ultrahigh vacuum ring on a closed loop and thus circle the ring a vast number of times. The electrons are forced to travel in a closed loop by strong magnetic fields provided by devices such as bending magnets, undulators and wigglers. The magnets also need to repeatedly recompress the Coulomb-exploding space charge electron bunches. The change of direction is a form of acceleration and thus the electrons lose energy as electromagnetic radiation. This is similar to a radio antenna, but with the difference that the relativistic speed changes the observed frequency due

to the Doppler effect by a factor γ~1000. A resonant cavity repeatedly accelerates the electrons to fill the energy loss. Another dramatic effect of relativity is that the radiation pattern is also distorted from the isotropic dipole pattern, expected from non-relativistic theory, into a narrow cone in the forward direction tangent to the particles orbit. This makes synchrotron radiation sources the brightest known light sources. The planar acceleration geometry makes the radiation linearly polarized when observed in the orbital plane, and circularly polarized when observed at a small angle to that plane. The emitted radiation is channelled through beamlines to experimental workstations. Synchrotron facilities provide radiation from the far infrared through the visible, near-ultraviolet, vacuum-ultraviolet, soft X-ray, and hard X-ray parts of the electromagnetic spectrum, extending up to 100 keV and beyond, depending on the electron beam energy and on the intensity of the applied magnetic fields.

Regarding mesostructured films, there are a few aspects of synchrotron radiation that have made small angle scattering studies very effective. These are: very small beam divergence, high beam flux, and in some cases energy tuneability. It is crucial to have small beam divergence in order to isolate weak scattering at very small angles from the direct beam which is orders of magnitude stronger. The flux of a synchrotron source is usually several orders of magnitude higher than those from conventional X-ray sources, therefore a diffraction pattern can be acquired in short times, typically on the order of 500 ms, making it possible to perform time-resolved in-situ experiments during dip-coating. When beam energy is tuneable, it is possible to conduct anomalous small-angle X-ray scattering.

2.1.3 SAXS measurements at the ELETTRA synchrotron facility

All SAXS experiments presented in this thesis were conducted at the Austrian beamline at the ELETTRA synchrotron in Trieste. The photon source is the 57-pole NdFeB hybrid wiggler, which delivers a very intense radiation between 4 and 25 keV, of which three discrete energies (5.4, 8 and 16 keV) can be selected by a flat double crystal (111 Si) monochromator in optics hutch 1 and focused by a double focusing toroidal mirror in optics hutch 2 (Figure 2.1).

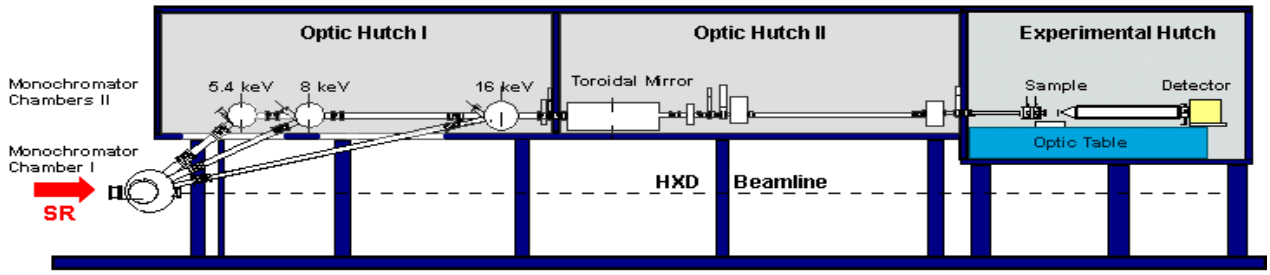

Figure 2.1: Scheme of the Austrian SAXS beamline at Elettra: synchrotron radiation (SR) is monochromated by a flat double crystal in optics hutch 1 and focused by a toroidal mirror in optics hutch 2. Downstream of the optics hutches is the experimental hutch.

The entire beamline is controlled via a software interface developed with LabView. Typically, for an electron energy in the storage ring of 2 GeV, an intensity of 200 mA and a selected energy of 8 keV, the flux density at the sample is $2.5 \cdot 10^{11}$ photons$\cdot s^{-1} \cdot mm^{-2}$. The optical table in the experimental hutch allows optimisation of the sample-to-detector distance with respect to SAXS resolution and sample size setup, as well as installation of specialised sample equipment (Figure 2.2). A two-dimensional CCD detector (Photonic Science, UK) is used for data acquisition.

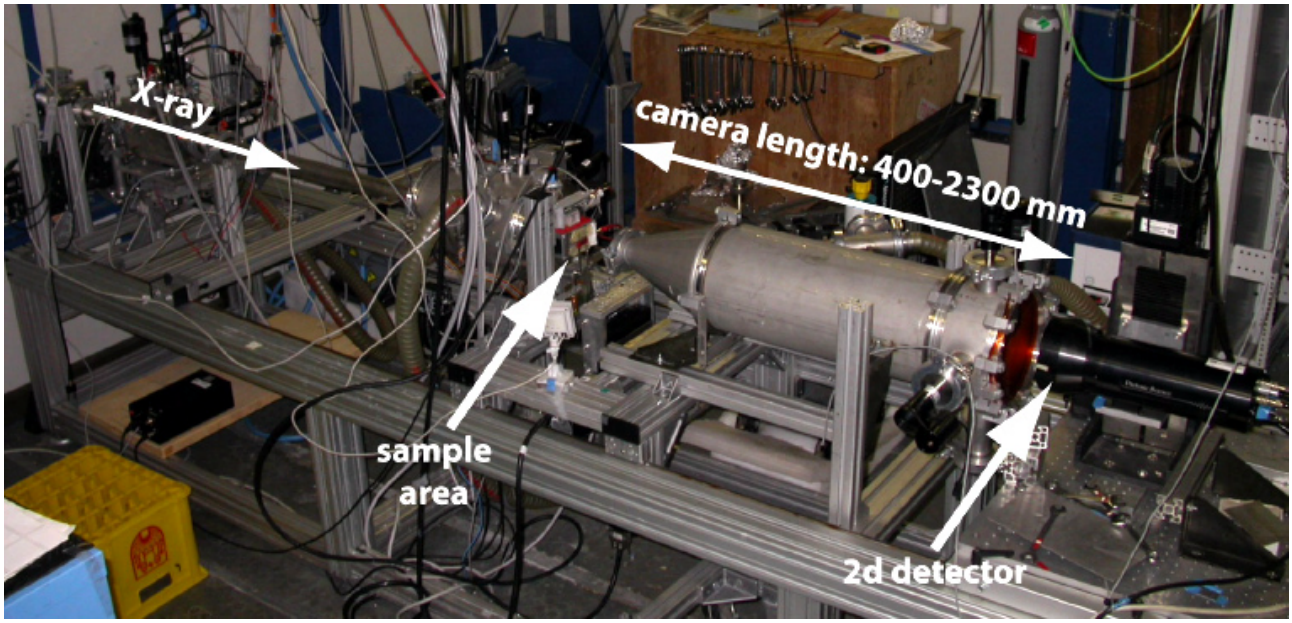

Figure 2.2: Experimental hutch with optical table: the incident and scattered waves propagate in vacuum tubes with kapton windows; the camera length (sample-to-detector distance) can be varied by moving the CCD detector and using vacuum tubes with different length.

Before starting a measurement session, the sample-to-detector distance is adjusted in order to ensure that the diffracted beams be well separated from the direct beam, and a sufficiently large area of the reciprocal space be sampled by the CCD detector. The beam stopper must be correctly positioned in order to prevent the direct beam from hitting the detector, as this may cause irreversible damage to the CCD array. In a typical collection of a SAXS pattern, the sample is placed on a sample holder, which can be rotated via a servo motor from the control room, so that the angle of incidence can be varied. It is of utmost importance that a diffraction pattern of a calibration standard be acquired for each setup of the beamline. Diffraction standards provide a tool to determine accurately the beam centre position and the sample-to-detector distance. Without such a calibration it is not possible to perform quantitative data analysis such as cell constant calculation. We used a silver behenate powder standard ($CH_3(CH_2)_{20}COOAg$, d-spacing=58.38 Å) [34] in a capillary glass: the ring-like diffraction pattern is used in the data analysis software. Diffraction patterns are acquired using the CCD detector provided with a software-triggered fast shutter positioned upstream. Image-Pro® Plus

is used as the CCD control software. At first, a low acquisition time is selected (e.g. 100 ms) in order to avoid saturation which could damage the detector, then it can be increased so that less intense diffraction signal is acquired (e.g. from higher diffraction orders).

The diffraction pattern of a mesostructured film depends not only on the mesostructure symmetry and orientation, but also on the experimental measurement conditions, such as the angle of incidence. In general, the model of the monocrystal-like mesostructure is not true for "real" films. These are almost always composed of micron-sized mesostructured domains which possess an orientational disorder around the axis perpendicular to the substrate, this is a feature common to nearly all mesostructured films that is also called planar disorder. Thus, mesostructured films typically have out-of-plane order, but lack in-plane order. This is true if we consider a sufficiently large region investigated by the impinging beam: at the SAXS beamline at ELETTRA this is typically on the order of the millimetre, therefore $\sim 10^3$ mesostructured domains are sampled.

There are essentially two configurations used in the acquisition of SAXS patterns of mesostructured films: the angle of incidence of the X-ray beam impinging on the sample may be set to either small angle (slightly above the critical angle, i.e. 0.2–0.3°) or perpendicular to the film surface (90°). These two configurations are referred to as grazing and transmission incidence, respectively, and yield information on the out-of-plane and in-plane mesostructure order. When the sample is in grazing incidence (grazing incidence SAXS, or GISAXS) the detector acquires out-of-plane reflections that are not accessible by transmission mode, whereas in transmission mode in-plane reflections are sampled which cannot be recorded in grazing incidence. Due to the lack of global in-plane order, the reciprocal lattice is a collection of concentric rings, centred on the axis perpendicular to the substrate. These rings can be thought as the infinite replication of the spots around the axis perpendicular to the substrate and intersecting the origin. When the Ewald sphere slices the ring-like reciprocal lattice in grazing incidence, the intersection is constituted by spots, whereas in transmission mode the intersection is constituted by rings (Figure 2.3), thus the detector records spots in the former case and rings in the latter case.

The choice of substrate depends on whether we are working in grazing incidence or transmission mode. In transmission mode the diffracted beams must travel through the substrate and towards the detector, therefore a thick substrate (e.g. 400 μm Si wafer, soda-lime glass) cannot be used and thin substrates must be resorted to (e.g. 50 μm Si wafer). In fact, the transmitted intensity fraction of a 8 keV radiation (corresponding to a wavelength of 1.54 Å) on a 400 μm Si wafer is only $\sim 10^{-3}$ (with respect to the incident intensity). Using a 50 μm Si wafer however the transmitted intensity fraction increases to 0.5. In grazing incidence, substrate thickness is not an issue, as the diffracted beams do not traverse the substrate, therefore either thick or thin substrates can be used.

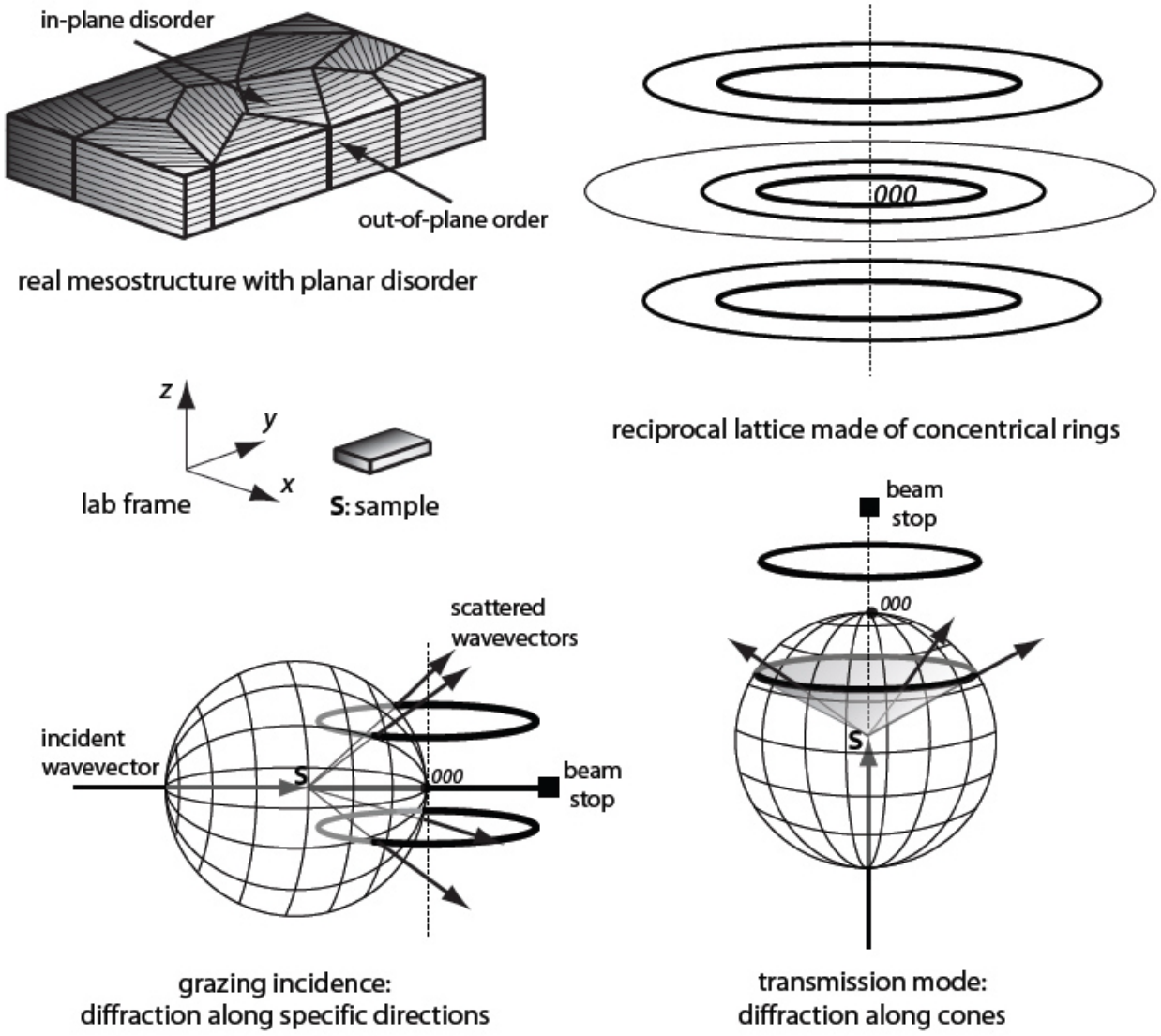

Figure 2.3: Real mesostructure with in-plane misorientation of ordered mesostructured domains: the reciprocal lattice can be pictured as a collection of concentric rings, whose intersection with the Ewald sphere gives either spots or rings depending on whether the measurement is in grazing incidence or in transmission mode.

In order to conduct in-situ experiments at the SAXS beamline of ELETTRA to investigate mesostructure formation upon solvent evaporation during dip-coating in the first seconds after film deposition, a dip-coater was specifically built. A vessel containing the solution is moved vertically by a linear guide and the sample is kept at a fixed position to ensure that the probed region of the sample is not changed during the whole experiment. The linear guide is moved by a direct current motor which is remotely controlled through a controller interfaced with a PC. The linear guide provides micrometric control on the movement and speed when raising and lowering the solution vessel, as well as vibration damping. The dip-coater is enclosed in an airtight cabinet into which dry or wet air can be pumped in order to control relative humidity.

Diffraction patterns are stored in 12-bit TIFF files which can readily manipulated with software Fit2d. This is a general purpose and specialist data analysis software developed at the European Synchrotron Research Facility (ESRF), used on most beamlines at ESRF and other synchrotron facilities, as well as by many other crystallography groups throughout the world [35]. Fit2d is used for both interactive and batch data processing, and includes important image analysis tools such as intensity scaling, one-click d-spacing calculation, 1-d integration, calibration and correction for detector distortions. Diffraction patterns taken in grazing incidence and transmission mode give a first hint on the presence of an ordered mesostructure and its planar disorder. A first visual inspection can give a clue on the mesostructure symmetry group if this is known from the literature or from previous data, especially for a trained eye, but a more accurate attribution of the pattern to a space group can be performed by software simulations, for example with CMPR, or with Nanocell. CMPR [36] is a multipurpose program that can be used for displaying diffraction data, as well as manual auto-indexing and peak fitting. Nanocell [37] is an interesting code written for Mathematica® by Prof. Hillhouse's research group specifically for mesostructured films, and which takes into account dynamical effects involving multiple reflection-refraction effects in the film. The diffraction pattern is then indexed according to its space group by assigning *hkl* indices to each spot in the pattern. After that, the d-spacings of each spot are measured so that cell parameters can be calculated.

2.2 Fourier-transform infrared (FTIR) spectroscopy

2.2.1 Interaction of infrared radiation with matter

When electromagnetic radiation passes through matter (solid, liquid or gas), certain frequencies are absorbed, thus from the measurement of the intensity absorbed by the sample under investigation at different incident energies it is possible to perform qualitative and quantitative analysis. Spectroscopic techniques are based on such kind of interaction. The infrared (IR) portion of the electromagnetic spectrum ranges from 0.78 to 1000 μm of wavelength. In this case, the wavelength is usually indicated by the wavenumber, expressed in cm^{-1}, corresponding to the number of electromagnetic field oscillations in 1 cm. The IR range is divided into three regions: the near-, mid- and far-IR, named for their relation to the visible spectrum. The far-IR, (400–10 cm^{-1}) lying adjacent to the microwave region, the mid-IR region (4000–400 cm^{-1}) and the near-IR (14000–4000 cm^{-1}).

Infrared spectroscopy exploits the fact that molecules have specific frequencies at which they rotate or vibrate (vibrational modes) corresponding to discrete energy levels. In order for a vibrational mode in a molecule to be IR active, it must be associated with changes in the electric dipole moment. For example, charge distribution in a HCl molecule is not symmetrical, in that Cl has a higher electronic density than H, thus the molecule is said to be polar. As the HCl molecule starts to vibrate, the dipole momentum changes and a restoring electric field is set up. If there is a match between the frequency of the incident electromagnetic radiation and the resonance frequency of the HCl molecule, energy is transferred to the HCl molecule and a decrease in the transmitted intensity is observed. By varying the incident energy in small steps and recording the intensity transmitted through the sample, a wavenumber vs. absorbed intensity spectrum can thus be obtained, showing absorption bands. Band intensities can expressed as absorbance (A), defined as

$$A = \log_{10}\left(\frac{I_0}{I}\right) = -\log_{10}(T) \tag{2.14}$$

where I_0 and I are the intensities of the incident beam and of the beam transmitted through the sample, respectively, and $T=I/I_0$ is the transmittance.

The resonant frequencies of a molecule are determined by the shape of the molecular potential energy surfaces, the masses of the atoms and by the associated vibronic coupling. In particular, in the Born-Oppenheimer and harmonic approximations, i.e. when the molecular Hamiltonian corresponding to the electronic ground state can be approximated by a harmonic oscillator in the neighborhood of the equilibrium molecular geometry, the resonant frequencies are determined by the normal modes corresponding to the molecular electronic ground state potential energy surface. Nevertheless, the resonant frequencies can be in a first approach related to the strength of the bond, and the mass of the atoms at either end of it. Thus, the frequency of the vibrations can be associated with a particular bond type. Simple diatomic molecules have only one bond, which may stretch. More complex molecules have many bonds, and vibrations can be conjugated, leading to infrared absorptions at characteristic frequencies that may be related to chemical groups.

Vibrational motions fall into two categories: stretching, when there is a change in the interatomic distance along the bond axis, and bending, when there is a change in the angle between two bonds. Stretching and bending modes can be further divided into six types of vibration: symmetrical and antisymmetrical stretching, scissoring, rocking, wagging and twisting, as shown in Figure 2.4. In general, a molecule consisting of n atoms has a total of $3n$ degrees of freedom, corresponding to the Cartesian coordinates of each atom in the molecule. In a nonlinear molecule, 3 of these degrees are rotational and 3 are translational and the remaining correspond to fundamental vibrations; in a linear

molecule, 2 degrees are rotational and 3 are translational. The net number of fundamental vibrations is therefore $3n-6$ for nonlinear molecules and $3n-5$ for linear molecules.

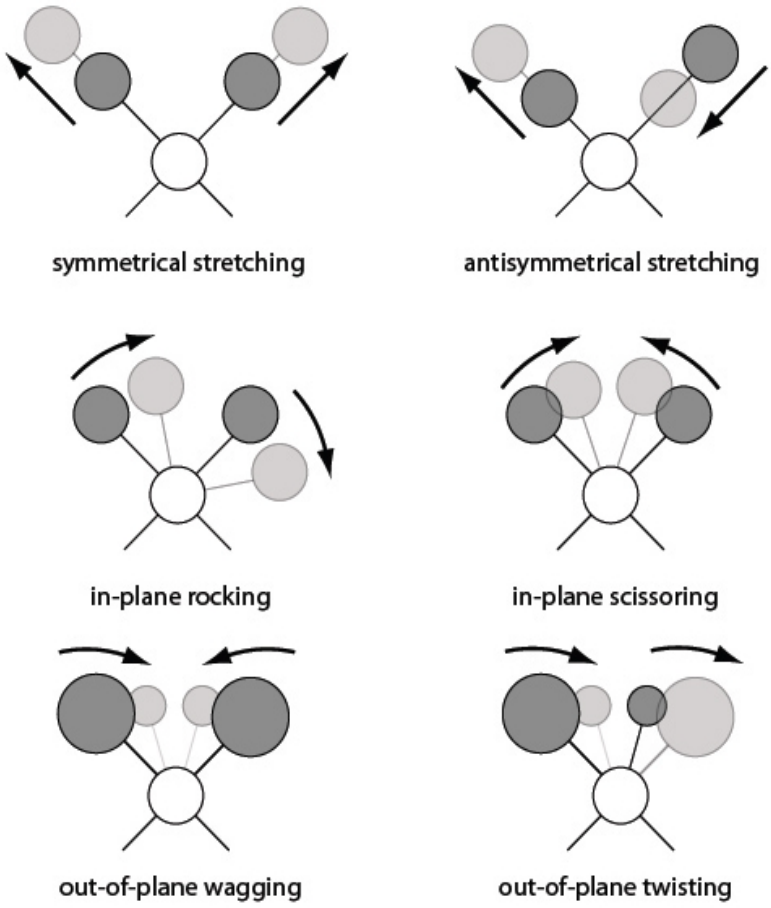

Figure 2.4: Examples of vibrational modes of a diatomic molecule: the first two ones are stretching modes (symmetrical and antisymmetrical), the others can be classified as bending modes (rocking, scissoring, wagging, twisting).

The stretching frequency of a bond can be calculated by considering a simple mechanical model, where two masses m_1 and m_2 are linked by a spring. A perturbation of one mass along the spring axis, such as a movement of y from its equilibrium position, causes a restoring force $F=-ky$ which is proportional to the mass displacement, the proportionality constant being the spring constant k. Thus a vibration is set up, called simple harmonic movement. Since we are dealing with atoms and chemical bonds instead of masses and springs, we need to resort to quantum mechanics: as stated above, the molecular Hamiltonian corresponding to the electronic ground state can be approximated by a harmonic oscillator in the neighborhood of the equilibrium molecular geometry (Figure 2.5, left). Solving the Schrödinger equation for this system with the harmonic potential leads to the well-known energy quantization, which can be expressed as:

$$E = \hbar\left(n + \frac{1}{2}\right)\sqrt{\frac{k}{\mu}} \tag{2.15}$$

where n is the vibrational quantum number, which is a positive integer, and μ is the reduced mass $\mu = m_1 m_2 / m_1 + m_2$. The transition energy from level 1 to level 2 is equal to the transition energy from level 2 to level 3, and so on. Thus, according to the selection rule $\Delta n = \pm 1$ only one absorption band should be observed for each molecular vibration, but this is in contrast with experimental data. Therefore, we have to make some correction to the harmonic model, introducing anharmonic terms: in particular, when the displacement of the two atoms is not so small to be considered a perturbation, the harmonic approximation does not hold. For example, when the atoms get too close, the potential energy increases dramatically because of electrostatic repulsion; on the other hand, when the atoms are too far away, the interatomic distance is so large that dissociation can occur (Figure 2.5, right). This can be solved analytically, however the solutions are quite complicated and fall outside the scope of this description of IR spectroscopy. In practice, there are several factors increasing the number of absorption bands, such as: overtone bands (absorption at frequencies representing the fundamental frequencies at the multiples of the fundamentals), combination bands (two fundamental vibrations interact and are influenced by radiation at the combined frequency, vibrational-rotational bands (the single vibrational band is accompanied by a series of smaller bands at lower and higher frequencies, especially in gas phase), and harmonic coupling bands (interaction from adjacent groups of nearly identical oscillation frequencies produces a series of bands quite apart from those normally expected).

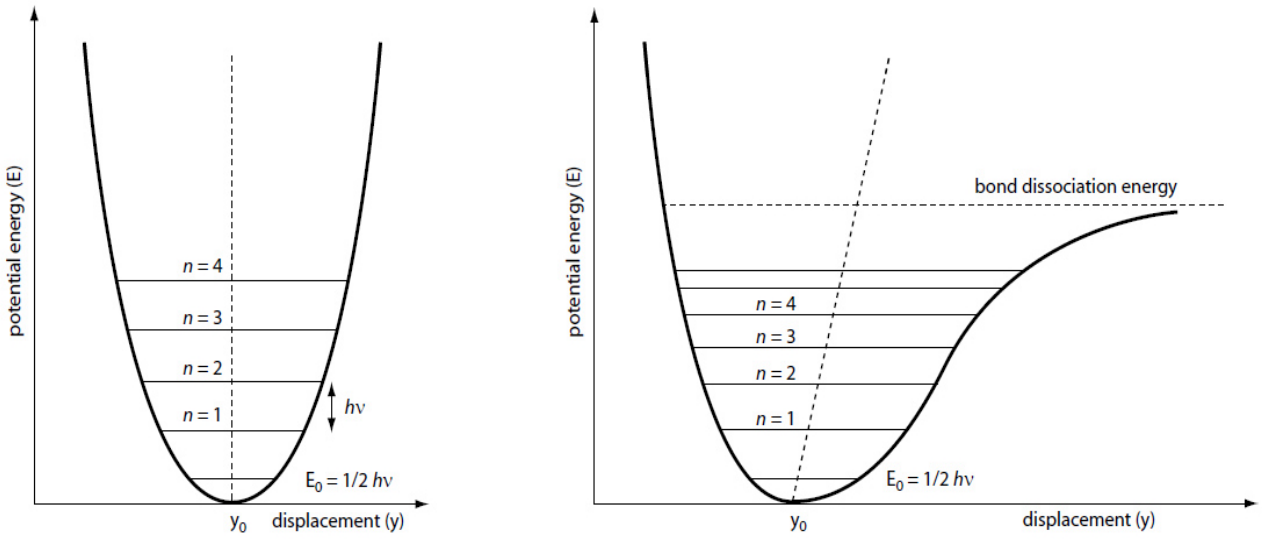

Figure 2.5: *Left:* Energy curve for a vibrating spring with quantum mechanical behaviour. *Right:* energy curve for an anharmonic oscillator, showing the vibrational levels for a vibrating bond.

2.2.2 FTIR spectroscopy: data acquisition and Fourier transformation

The essential piece of optical hardware in a FTIR spectrometer is the interferometer. The basic scheme of an idealized Michelson interferometer is shown in Figure 2.6A. Infrared light emitted by a source is directed to a device called the beam splitter, because it ideally allows half of the light to pass through while it reflects the other half. The reflected part of the beam travels to the fixed mirror M_1 through a distance L, is reflected there and hits the beam splitter again after a total path length of $2L$. The same happens to the transmitted part of the beam. However, as the reflecting mirror M_2 for this interferometer arm is not fixed at the same position L but can be moved very precisely back and forth around L by a distance x, the total path length of this beam is accordingly $2(L=x)$. Thus when the two halves of the beam recombine again on the beam splitter they exhibit a path length difference or optical retardation of $2x$, i.e. the partial beams are spatially coherent and will interfere when they recombine. The beam leaving the interferometer is passed through the sample compartment and is finally focused on the detector D.

The quantity actually measured by the detector is thus the intensity $I(x)$ of the combined IR beams as a function of the moving mirror displacement x, the so-called interferogram (Figure 2.6B). The interferometer produces and recombines two wave trains with a relative phase difference, depending on the mirror displacement. These partial waves interfere constructively, yielding maximum detector signal, if their optical retardation is an exact multiple of the wavelength:

$$2x = n\lambda \quad (n = 0,1,2,...) \tag{2.16}$$

Minimum detector signal and destructive interference occur if $2x$ is an odd multiple of $\lambda/2$. The complete dependence of $I(x)$ on x is given by a cosine function:

$$I(x) = S(\nu)\cos(2\pi\nu x) \tag{2.17}$$

Where we have introduced the wavenumber $\nu=1/\lambda$, which is more common in FTIR spectroscopy, and $S(\nu)$ is the intensity of the monochromatic line located at wavenumber ν.

Equation (2.17) is extremely useful for practical measurements, because it allows very precise tracking of the movable mirror. In fact, all modern FTIR spectrometers use the interference pattern of the monochromatic light of a He-Ne laser to control the change in optical path difference (Figure 2.6C). This demonstrates how the IR interferogram is digitized precisely at the zero crossings of the laser interferogram. The accuracy of the sample spacing Δx between two zero crossings is solely determined by the precision of the laser wavelength itself. As the sample spacing $\Delta\nu$ in the spectrum is inversely proportional to Δx, the error in $\Delta\nu$ is of the same order as in Δx. Thus, FTIR spectrometers have a built-in wavenumber calibration of high precision (practically about 0.01 cm^{-1}). This advantage is known as the Connes advantage.

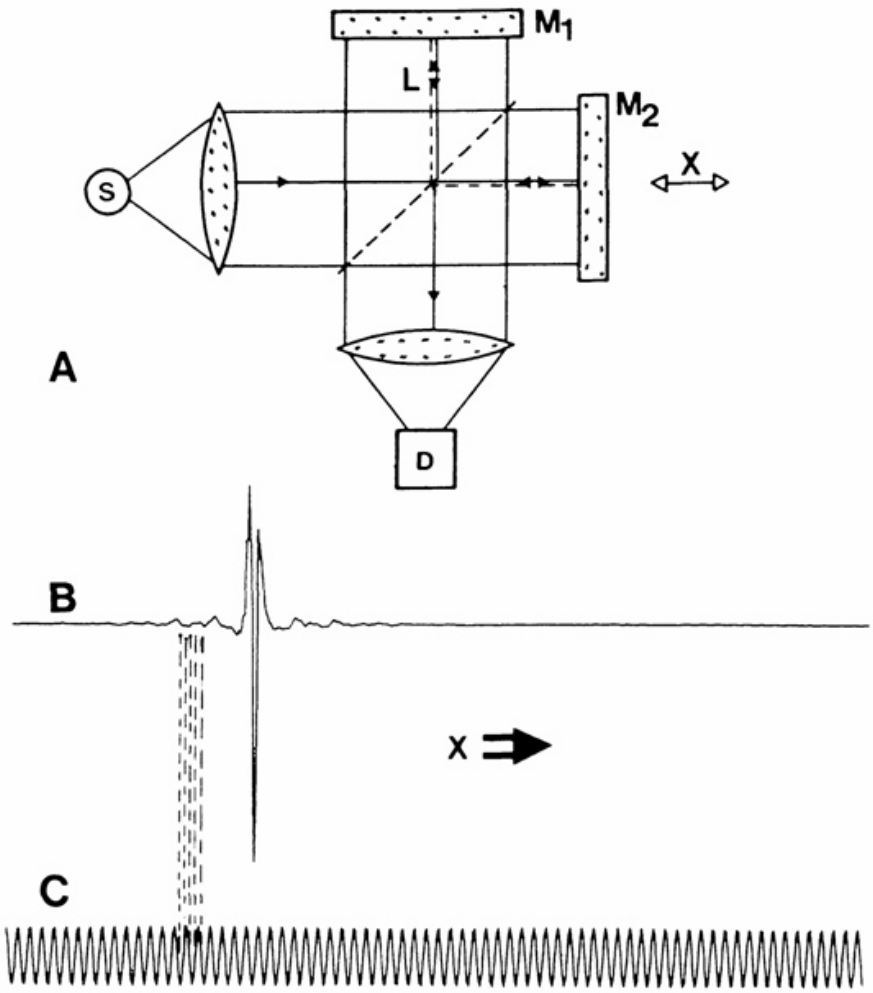

Figure 2.6: A) Schematics of a Michelson interferometer, S: source, D: detector, MI: fixed mirror, M2: movable mirror, X: mirror displacement, B) Signal measured by detector D. This is the Interferogram. C) Interference pattern of a laser source. Its zero crossings define the positions where the interferogram is sampled (dashed lines).

Besides its high wavenumber accuracy, FTIR has other features, which make it superior to conventional (dispersive) IR. The so-called Jacquinot or throughput advantage arises from the fact that the circular apertures used in FTIR spectrometers have a larger area than the linear slits used in grating spectrometers, thus enabling higher throughput of radiation. In conventional spectrometers the spectrum $S(\nu)$ is measured directly by recording the intensity at different monochromator settings ν, one ν after the other. In FTIR, all frequencies emanating from the IR source impinge simultaneously on the detector. This accounts for the so-called multiplex or Fellget advantage. The measuring time in FTIR is the time needed to move mirror M_2 over a distance proportional to the desired resolution. As the mirror can be moved very fast, complete spectra can be measured in fractions of a second, so this is a great advantage for fast time-resolved measurements. Finally, the Fellget and Jacquinot advantages permit construction of interferometers having much higher resolving power than dispersive instruments.

Data acquisition yields the digitized interferogram *I(x)*, which must be converted into a spectrum by means of a mathematical operation called Fourier transformation (FT). Generally, the FT determines the frequency components making up a continuous waveform. However, if the waveform (the interferogram) is sampled and consists of *N* discrete, equidistant points, one has to use the discrete version of the Fourier transformation (DFT):

$$S(k\Delta\nu) = \sum_{n=0}^{N-1} I(n\Delta x)\exp(i2\pi nk/N) \tag{2.18}$$

Where the continuous variables x, ν have been replaced by $n\Delta x$ and $k\Delta\nu$, respectively. The spacing $\Delta\nu$ in the spectrum is related to Δx by

$$\Delta\nu = 1/(N * \Delta x) \tag{2.19}$$

The DFT expresses a given function as a sum of sine and cosine functions. The resulting new function $S(k\Delta\nu)$ then consists of the coefficients (called the Fourier coefficients) necessary for such a development. Alternatively, if the set $S(k\Delta\nu)$ of Fourier coefficients is known, one can easily reconstruct the interferogram $I(n\Delta x)$ by combining all cosines and sines multiplied by their Fourier coefficients $S(k\Delta\nu)$ and dividing the whole sum by the number of points *N*. This is stated by the formula for the inverse discrete Fourier transformation (IDFT):

$$I(n * \Delta x) = (1/N)\sum_{n=0}^{N-1} S(k * \Delta\nu)\exp(-i2\pi * nk/N) \tag{2.20}$$

After storing measured data, the DFT and IDFT must be calculated numerically by a computer. For n=0, the exponential in (2.20) is equal to unity. For this case, expression (2.20) states, that the intensity $I(0)$ measured at the interferogram centerburst is equal to the sum over all *N* spectral intensities divided by *N*. This means the height of the center burst is a measure of the average spectral intensity. In practice, equation (2.18) is seldom used directly because it is highly redundant. Instead a number of so-called fast Fourier transforms (FFTs) are in use, the most common of which is the Cooley-Tukey algorithm. The aim of these FFTs is to reduce the number of complex multiplications and sine and cosine calculations appreciably, leading to a substantial saving of computer time. The small price paid for the speed is that the number of interferogram points *N* cannot be chosen at will, but depends on the algorithm. In the case of the Cooley-Tukey algorithm, which is used by most FTIR manufacturers with slight modifications, *N* must be a power of two. The final spectrum is obtained from the interferograms not only by performing the FT, but also by adding other mathematical operations, such as: zero-filling, phase correction and apodization, but they will not be discussed in this thesis.

To obtain a transmittance spectrum, three steps are necessary: (1) An interferogram measured without sample in the optical path is Fourier transformed and yields the so-called single channel

reference spectrum $R(\nu)$; (2) An interferogram measured with a sample in the optical path is Fourier transformed and yields the so-called single channel sample spectrum $S(\nu)$; (3) The final transmittance spectrum $T(\nu)$ is defined as the ratio $T(\nu)=S(\nu)/R(\nu)$ and the absorbance spectrum $A(\nu)$ can be obtained by the formula (2.14).

2.2.3 FTIR measurements at DAΦNE and ELETTRA synchrotron facilities

Most of the IR measurements presented in this doctorate work have been performed at the SINBAD (Synchrotron INfrared Beamline at Daϕne) beamline [38] installed at the DAΦNE synchrotron of Laboratori Nazionali di Frascati of the Istituto Nazionale di Fisica Nucleare and a minor part of them at the SISSI (Source for Imaging and Spectroscopic Studies in the Infrared) beamline [39] installed at the ELETTRA synchrotron in Trieste.

The SINBAD beamline extracts IR radiation from the electron beam passing through a bending magnet of the DAΦNE electron-positron storage ring. The beam energy is 0.51 MeV and current can reach values up to 1.8 A, which makes this source one of the most brilliant and brightest in the world. The first mirror of the beamline has an acceptance (HxV) of 20x30 mrad which allows the collection of IR radiation from the near-IR through the far-IR, the beam is then collimated and focused into the laboratory by six gold mirrors. In the focus position a wedged diamond window separates the beamline from the laboratory, where a Bruker Equinox 55 FTIR interferometer is installed (Figure 2.7). The interferometer has been modified to work in a maximum vacuum of 10^{-5} mbar and in the sample compartment a cryostat for measurements in the 4-500 K temperature range can be used. At a lateral exit port of the interferometer a Bruker Hyperion 3000 IR microscope is installed and it is equipped with both a single element mercury-cadmium-telluride detector and a 64x64-pixel focal plane array detector for imaging. These instruments are also equipped with many accessories to perform measurements on different kind of samples (solid samples, liquids, gases) and with different sampling techniques (transmission, reflection, attenuated total reflection, diffuse total reflection) and they can exploit both the diffraction-limited brilliant synchrotron source and the conventional sources.

The SISSI beamline extracts IR radiation from the electron beam passing through a bending magnet of the ELETTRA storage ring. The beam energy is 2.4 GeV and current reaches a maximum value of 300 mA. The first mirror of the beamline (composed of four mirrors) has an acceptance (HxV) of 70x25 mrad and collects both the bending magnet and a part of the edge radiation, so the IR beam intensity is peaked in the mid-IR range and the SISSI beamline is mainly suitable for IR microscopy investigations. At the end of the beamline two FTIR interferometers are installed: (1) a Bruker Vertex 70 with a Bruker Hyperion 3000 microscope equipped with a single element and a 64x64-

pixel focal plane array detector; (2) a Bruker IFS 66v/S with a Bruker Hyperion 2000 microscope with just the single element detector. Also in this case both instruments can work with synchrotron radiation and conventional sources and are equipped with many accessories for different kind of samples and measuring conditions.

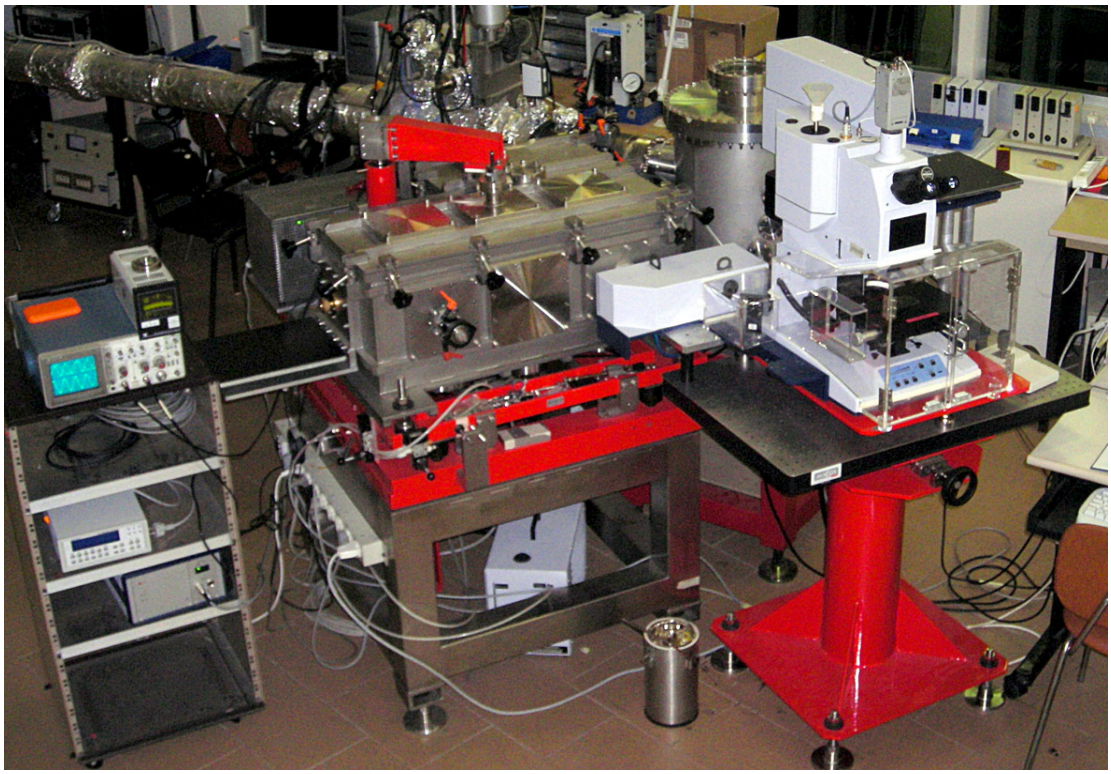

Figure 2.7: Experimental station of SINBAD beamline at DAΦNE: it includes a Bruker Equinox 55 FTIR interferometer modified to work in vacuum and a Bruker Hyperion 3000 microscope.

2.2.4 Two-dimensional correlation spectroscopy

In an IR spectroscopic measurement, an IR beam is applied to the system of interest. The characteristic interaction between the beam and system constituents, such as different chemical groups, is represented in the form of a spectrum and then analyzed to elucidate the detailed information about the system. In 2D correlation spectroscopy, an additional external perturbation is applied to the system during the spectroscopic measurement. This external perturbation stimulates the system to cause some selective changes in the state, order, surroundings, etc. of system constituents. The overall response of the stimulated system to the applied external perturbation leads to distinctive changes in the measured spectrum. This spectral variation induced by an applied perturbation is referred to as a *dynamic spectrum* in 2D correlation. Any spectroscopic experiment, which utilizes an external perturbation to generate some form of dynamic spectra, is a good potential candidate for benefiting from 2D correlation analysis, but any transient experiment, such

as chemical reactions, may also be analyzed by this method, so this is the case of in-situ IR characterization of mesoporous films during EISA.

The basic concept of *perturbation-based* two-dimensional spectroscopy applicable to infrared was proposed first by Noda in 1986 [40,41,42]. This new form of 2D spectroscopy has evolved to become a very versatile and broadly applicable technique [43,44]. In the generalized 2D correlation spectroscopy scheme, a series of perturbation-induced dynamic spectra are collected first in a sequential order during the process. Such a set of dynamic spectra is then transformed into a set of 2D correlation spectra by cross-correlation analysis. One often finds that 2D correlation spectra provide useful information which is not readily available from or at least not apparent in the original set of conventional 1D spectra. This is the prime motivation behind constructing 2D correlation spectra.

Let us consider a perturbation-induced variation of a spectral intensity $y(\nu, t)$ observed during a fixed interval of some external variable t between T_{min} and T_{max}. While this external variable t in many cases is the conventional chronological time, it can also be any other reasonable measure of a physical quantity. The variable ν can be any appropriate spectral index used in the field of spectroscopy, i.e. the wavenumber in IR.

The *dynamic spectrum* $\tilde{y}(\nu,t)$ of a system induced by the application of an external perturbation is formally defined as:

$$\tilde{y}(\nu,t) = y(\nu,t) - \tilde{y}(\nu) \quad \text{for} \quad T_{min} \le t \le T_{max} \tag{2.21}$$

$$\tilde{y}(\nu,t) = 0 \quad \text{otherwise}$$

where $y_{av}(\nu)$ is the *reference spectrum* of the system. While selection of a proper reference spectrum is not strictly specified, in most cases, it is customary to set $y_{av}(\nu)$ to be the *stationary* or *averaged* spectrum given by

$$y_{av}(\nu) = \frac{1}{T_{max} - T_{min}} \int_{T_{min}}^{T_{max}} y(\nu,t)dt \tag{2.22}$$

The fundamental concept governing 2D correlation spectroscopy is a quantitative comparison of the patterns of spectral intensity variations along the external variable t observed at two different spectral variables, ν_1 and ν_2, over some finite observation interval between T_{min} and T_{max}. The 2D correlation spectrum can be expressed as

$$X(\nu_1,\nu_2) = \langle \tilde{y}(\nu_1,t) \cdot \tilde{y}(\nu_2,t') \rangle \tag{2.23}$$

The intensity of 2D correlation spectrum $X(\nu_1,\nu_2)$ represents the quantitative measure of a comparative similarity or dissimilarity of spectral intensity variations $\tilde{y}(\nu,t)$ measured at two

different spectral variables, ν_1 and ν_2, during a fixed interval. The symbol < > denotes for a cross-correlation function designed to compare the dependence patterns of two chosen quantities on t .

In order to simplify the mathematical manipulation, $X(\nu_1,\nu_2)$ is treated as a complex number function

$$X(\nu_1,\nu_2)=\Phi(\nu_1,\nu_2)+i\Psi(\nu_1,\nu_2) \tag{2.24}$$

comprising two orthogonal (i.e., real and imaginary) components, known respectively as the *synchronous* and *asynchronous* 2D correlation intensities.

The generalized 2D correlation function given below

$$\Phi(\nu_1,\nu_2)+i\Psi(\nu_1,\nu_2)=\frac{1}{\pi(T_{\max}-T_{\min})}\int_0^{\infty}\tilde{Y}_1(\omega)\cdot\tilde{Y}_2^{*}(\omega)d\omega \tag{2.25}$$

formally defines the synchronous and asynchronous correlation intensity introduced in Equation (2.24). The term $\tilde{Y}_1(\omega)$ is the forward Fourier transform of the spectral intensity variations $\tilde{y}(\nu_1,t)$ observed at a given spectral variable ν_1 with respect to the external variable t. It is given by

$$\tilde{Y}_1(\omega)=\int_{-\infty}^{+\infty}\tilde{y}(\nu_1,t)e^{-i\omega t}dt=\tilde{Y}_1^{\mathrm{Re}}(\omega)+i\tilde{Y}_1^{\mathrm{Im}}(\omega) \tag{2.26}$$

where $\tilde{Y}_1^{Re}(\omega)$ and $\tilde{Y}_1^{Im}(\omega)$ are, respectively, the real and imaginary component of the Fourier transform. The conjugate of the Fourier transform $\tilde{Y}_2^{*}(\omega)$ of the spectral intensity variation $\tilde{y}(\nu_2,t)$ observed at another spectral variable ν_2 is given by

$$\tilde{Y}_2^{*}(\omega)=\int_{-\infty}^{+\infty}\tilde{y}(\nu_2,t)e^{+i\omega t}dt=\tilde{Y}_2^{\mathrm{Re}}(\omega)-i\tilde{Y}_2^{\mathrm{Im}}(\omega) \tag{2.27}$$

Once the appropriate Fourier transformation of the dynamic spectrum $\tilde{y}(\nu,t)$ defined in the form of Equation (2.21) is carried out with respect to the variable t , Equation (2.25) will directly yield the synchronous and asynchronous correlation spectrum, $\Phi(\nu_1,\nu_2)$ and $\Psi(\nu_1,\nu_2)$.

The intensity of a synchronous 2D correlation spectrum $\Phi(\nu_1,\nu_2)$ represents the simultaneous or coincidental changes of two separate spectral intensity variations measured at ν_1 and ν_2 during the interval between T_{min} and T_{max} of the externally defined variable t . A synchronous spectrum is a symmetric spectrum with respect to a diagonal line corresponding to coordinates $\nu_1=\nu_2$. Correlation peaks appear at both diagonal and off-diagonal positions. The intensity of peaks located at diagonal positions mathematically corresponds to the autocorrelation function of spectral intensity variations observed during an interval between T_{min} and T_{max}. The diagonal peaks are therefore referred to as autopeaks, and the slice trace of a synchronous 2D spectrum along the diagonal is called the autopower spectrum. The magnitude of an autopeak intensity, which is always positive, represents the overall extent of spectral intensity variation observed at the specific spectral variable ν during

the observation interval between T_{min} and T_{max}. Cross peaks located at the off-diagonal positions of a synchronous 2D spectrum represent simultaneous or coincidental changes of spectral intensities observed at two different spectral variables ν_1 and ν_2. It is often useful to construct a correlation square joining the pair of cross peaks located at opposite sides of a diagonal line drawn through the corresponding autopeaks to show the existence of coherent variation of spectral intensities at these spectral variables. While the sign of autopeaks is always positive, the sign of cross peaks can be either positive or negative. The sign of a synchronous cross peak becomes positive if the spectral intensities at the two spectral variables corresponding to the coordinates of the cross peak are either increasing or decreasing together as functions of the external variable during the observation interval. On the other hand, a negative sign of the cross peak intensity indicates that one of the spectral intensities is increasing while the other is decreasing.

The intensity of an asynchronous spectrum represents sequential or successive, but not coincidental, changes of spectral intensities measured separately at ν_1 and ν_2. Unlike a synchronous spectrum, an asynchronous spectrum is antisymmetric with respect to the diagonal line. The asynchronous spectrum has no autopeaks, and consists exclusively of cross peaks located at off-diagonal positions. By extending lines from the spectral coordinates of cross peaks to corresponding diagonal positions, one can construct asynchronous correlation squares. An asynchronous cross peak develops only if the intensities of two spectral features change out of phase with each other. The sign of an asynchronous cross peak becomes positive if the intensity change at ν_1 occurs predominantly before that at ν_2 in the sequential order of t . On the other hand, the peak sign becomes negative if the change at ν_1 occurs predominantly after ν_2. However, this sign rule is reversed if the synchronous correlation intensity at the same coordinate becomes negative, i.e., $\Phi(\nu_1,\nu_2)<0$.

There are exceptions to the interpretation rules of 2D correlation spectra discussed above. Moreover, the proper interpretation of complex features not related to intensity changes, such as band position shift and line broadening, needs a separate discussion. Generally, real-world spectral data often contain various imperfections, distortions, and noise interfering with the pertinent information. One of the most serious problems in 2D correlation spectroscopy is the appearance of artifacts in 2D maps. Spectral noises, baseline fluctuations, and band shifts are three major causes for the artifacts and misleading features. To avoid the artifacts produced by noise, some pre-treatment methods are useful. Several methods have been proposed that allow one to discriminate the real peaks from the artifacts in 2D maps and they have been applied in the treatment of data presented in this thesis. However, all of these subjects will not be treated here, but further reading can be reference #[45].

CHAPTER 3

Advanced characterisation of mesoporous silica films

In this chapter we apply the concepts and techniques described in the previous chapters to synthesize and characterize mesoporous silica films and membranes. This study has been conducted with the twofold purpose of acquiring insight into the basic self-assembly mechanism and tuning some physicochemical properties of such systems. In particular, time-resolved FTIR and SAXS techniques have been applied, also simultaneously, in-situ during film formation by EISA, to understand thoroughly the physics and chemistry underlying templated self-assembly in mesostructured films.

3.1 Mesoporous silica films

3.1.1 Synthesis protocol

The synthesis protocol of inorganic mesoporous silica films was obtained in a previous work, it consisted in the optimisation of the type and quantity of precursors in the initial sol (quantity and type of solvent, organic and inorganic precursors, quantity of water, ageing), as well as processing parameters (relative humidity, dip-coating pulling rate, thermal treatment) [46].

The inorganic precursor is tetraethoxysilane (TEOS), which was chosen because of its low kinetics of hydrolysis and condensation. Ethanol was selected as the solvent because of good wettability with the substrates (either Si wafers or glass slides) and compatibility with TEOS. Hydrochloric acid was selected as the catalyst in a concentration such that the solution pH was set near to the isoelectric point of SiO_2 ($pH_{iep} \sim 2$) in order to ensure stability of the sol increasing shelf life. A poly(ethylene oxide)-block-poly(propylene oxide)-blockpoly(ethylene oxide) amphiphilic block copolymer, commercially available from BASF as Pluronic™ F127 was selected as the templating agent due to its optimal self-assembly properties.

The precursor solution is prepared in two steps: a first solution (mother solution) is prepared mixing 3.08 ml EtOH and 4.26 ml TEOS, and adding 0.355 ml of a 0.768 M HCl solution. This sol is stirred for 60 minutes, then a templating slution is added, which is obtained by mixing 15 ml EtOH, 1.3 g Pluronic F127 and 1.5 ml of a 0.057 M HCl solution. The molar ratios are reported in Table

3.1. This solution is aged for about 7 days at room temperature to allow for a slight pre-condensation of the silane units (formation of the inorganic nano building blocks, NBBs, of suitable size), after which it is ready to be deposited. SAXS experiments showed that 7 days is the ageing time to achieve the maximum degree of order of the deposited films.

The typical choice for the substrates is Si wafers (100-oriented, p-type, B-doped, thickness 400 μm) because they are suitable for SAXS (either thin or thick substrates), TEM (good thermal dispersion and mechanical stability) and FTIR (transparent to IR radiation) measurements.

Dip-coating at low relative humidity (RH ~ 20%) yields mesostructured films with optical quality. This was determined by in situ SAXS experiments on mesostructured silica films: faster pulling rates yield thicker and less ordered films and vice versa. The maximum degree of order was achieved by selecting the minimum speed of the dip-coater: 2.3 mm/s.

	TEOS	EtOH	H_2O	HCl	F127
Mother	1	2.78	1.04	$1.43 \cdot 10^{-2}$	-
Templating	-	1	0.32	$3.32 \cdot 10^{-4}$	$3.76 \cdot 10^{-4}$
Final	1	16.32	5.42	$1.9 \cdot 10^{-2}$	$5 \cdot 10^{-3}$

Table 3.1: Molar ratios of the mother, templating and final solutions used in the preparation of mesoporous silica films.

3.1.2 Structural characterisation

SAXS experiments showed that as-deposited films are organised into a cubic phase with spherical micelles when deposition is carried out at RH around 20%, whereas a two-dimensional hexagonal symmetry with cylindrical micelles is formed at higher RH. For RH values different than these, wormlike (disordered) structures are formed.

Crystallography software CMPR3 was employed to analyse the SAXS patterns in transmission mode. The SAXS pattern of a sample treated at 60°C, acquired in transmission mode, presented diffraction rings (Figure 3.1). This pattern was integrated radially from the beam centre in order to obtain a 1-D plot of intensity vs. 2θ. The "HKLGEN" function of CMPR was used, which generates a list of the allowed reflections for a given set of unit cell constants and extinction conditions. It is possible to specify symmetry by space group and specify preferential orientation with respect to a substrate. A sample treated at 60°C was chosen because the structure at this temperature is assumed to be undistorted. Inspection of the intensity vs. 2θ plot obtained by radial integration of the SAXS pattern revealed that the interplanar distances d_{002} and d_{202} were representative of a cubic cell, because the ratio between the two d-spacings was found to be $d_{002}:d_{202}=1:\sqrt{3}$. Next, the GISAXS patterns of samples thermally treated at different temperatures were analysed using CMPR.

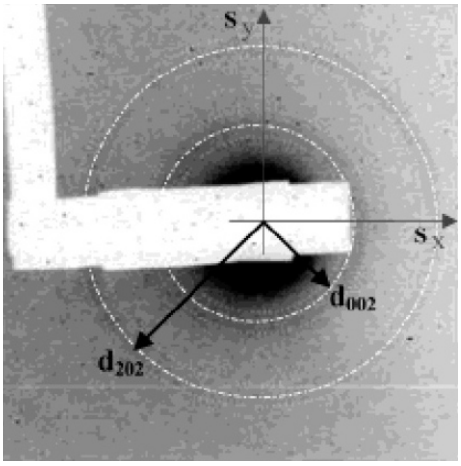

Figure 3.1: SAXS pattern in transmission mode of a mesostructured silica film treated at 60°C.

The best fit for the undistorted structure observed at 60°C corresponded to a body-centred cubic lattice having *Im3m* symmetry group oriented with the (110) plane parallel to the substrate, i.e. the direction [110] of the unit cells is normal to the film surface The *Im3m* unit cells form domains which are randomly oriented around the axis perpendicular to the substrate. This common feature of mesostructured films is commonly known as planar disorder and consists in the presence of out of plane order. The GISAXS patterns of samples treated at increasing temperatures show the increase of the out of plane spots (perpendicular to the film surface), whereas the in plane spots (parallel to the film surface) remain substantially unaltered. This corresponds to the uniaxial contraction of the mesostructure in the out of plane direction. This feature is commonly observed in mesostructured films [47,48] and is also known as thermal shrinkage. Two different symmetries that can originate from the uniaxial distortion of an *Im3m* structure along [110], namely *Fmmm* and *Fddd* which are both orthorhombic structures. The only symmetry that gave results matching the experimental SAXS patterns corresponded to the *Fmmm* symmetry group oriented with the (100) face parallel to the substrate. A list of the allowed *hkl* Miller indices and the corresponding coordinates (d-space and 2θ) were obtained as the best fit for the *Fmmm* cell. These reflection coordinates were transferred to the cylindrical coordinates observed in the GISAXS diffraction experiments (s_x and s_y), with the constraint for cell parameters: c= a√2. Two-dimensional plots were thus obtained for each pattern. Figure 3.2 shows the experimental GISAXS pattern superimposed with the simulation output by CMPR software referring to a film treated at 250°C. On the contrary, considering the SAXS patterns at 200°C, it can be noted that the *Im3m* to *Fmmm* transition is not yet marked, likely because the surfactant has not been removed and hinders shrinkage acting as a scaffold for the inorganic framework. The cell parameters were calculated for the *Fmmm* cell and resulted to be a = 21 nm, b = 18 nm and c = 29.7 nm.

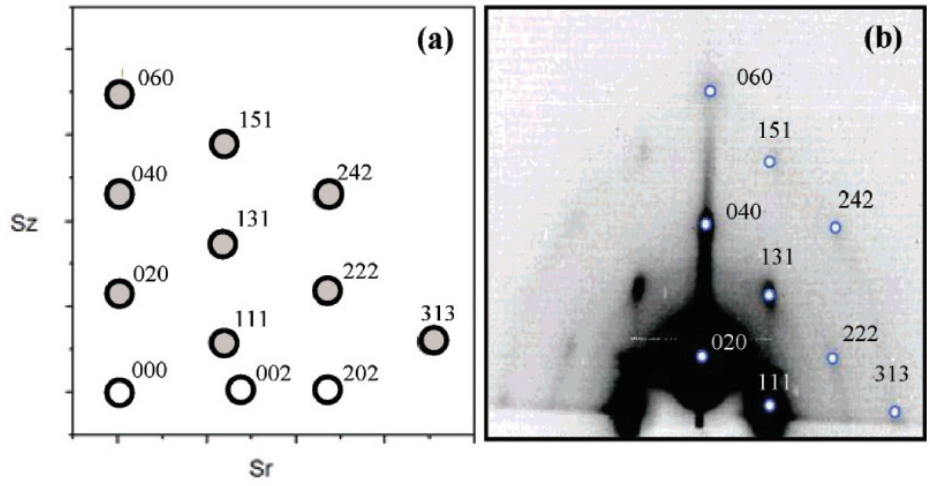

Figure 3.2: Comparison between a computer-simulated image utilising the CMPR programme, of an Fmmm structure with cell parameters a= 21nm, b= 18nm and c= 29.7nm (a), and the GISAXS pattern of a mesoporous silica film synthesised at RH=20% and treated at 250°C with the Fmmm indexing (b). Note that the a and c cell parameters of the Fmmm structure are such that c= a √2, which confirms the Im3m to Fmmm transition through a thermal shrinkage in the direction perpendicular to the substrate ([110] direction of the Im3m structure).

By using a transmission electron microscope (TEM), cross-sectional pictures of the samples were obtained. They reveal the ordered arrays of mesopores in the films. In Figure 3.3 it is possible to discern the 100 projection of the cubic *Im3m* structure and the 4-fold symmetry axis. Moreover, it can be noted that two ordered zones are located at the film-air and film-substrate interfaces, but at the centre of the film the mesopores become less defined and give rise to a wormlike or disordered region. This is due to inorganic condensation which may form a solid barrier that prevents further evaporation at the film-air interface, thus multiple mesostructures are likely to be "frozen" in their metastable states. The disordered central region does not affect deeply the GISAXS patterns (only a diffuse ring passing through the spots is visible, indicating a disordered region) because of the small penetration depth of X-rays in this configuration (the angle of incidence is slightly above the critical angle of the film), so only the first arrays of mesopores are probed. A line profile analysis was conducted on the ordered region of the film by loading a representative TEM image in the image manipulation software, the open source software "ImageJ" [49] and the "plot profile" tool was used to display a two-dimensional graph of the intensities of pixels along a line passing through the centres of 10 pores. The pore width was calculated as the FWHM of the curves in the plot, the analysis gave an estimated pore size of 5×3 nm with an error of 0.7 nm. The pores have an elliptical cross section due to uniaxial shrinkage.

The mesoporous silica films thus obtained exhibit an excellent thermal stability in a wide range of temperatures and it has been shown that the mesostructure remains organised up to the temperature of 950°C [46]. FTIR spectroscopy showed that this high thermal stability is correlated with a progressive strengthening of the SiO_2 framework during thermally-induced polycondensation

reactions and structural rearrangements of 4-fold rings present in the silica walls. The mesostructure after annealing at 850°C is free from silanols and maintains a high degree of order.

The synthesis protocol of mesoporous silica films described above allows obtaining mesoporous films with framework composition of silica or hydrated silica, with a content of hydroxyl groups which can be roughly tuned with the thermal treatment. However, the TEM image reported in Figure 3.3 shows that the film is not well ordered. To increase the degree of order, because deposition parameters had already been optimised in a previous work, we intervened at a molecular level, working on the precursor solution to construct different NBBs which could be able to build up a more defined mesostructure.

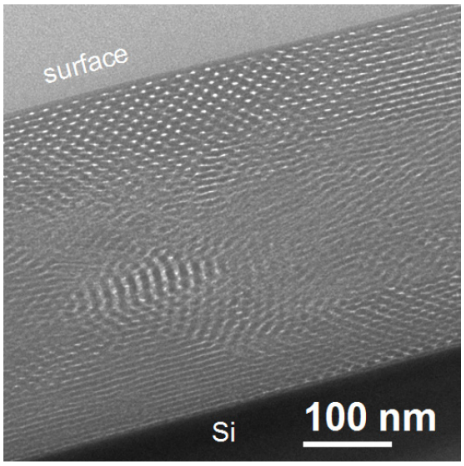

Figure 3.3: Transmission electron microscopy image in cross-section of a mesoporous silica film calcined at 350°C. Note the presence of a well-ordered phase at the film-air interface, a wormlike region at the centre of the film and a layered zone at the film-substrate interface.

3.2 Methyl-functionalized mesoporous silica films

3.2.1 Synthesis protocol

In order to increase the degree of order of the films, the precursor solution was modified by replacing part of TEOS with a hybrid precursor, that is methyl-triethoxysilane (MTES). It has three hydrolysable ethoxy (OCH_2CH_3) groups and a non-hydrolysable CH_3 group which is covalently bonded to the central Si atom. The use of organically modified alkoxysilanes in the synthesis of mesoporous silica films allows for a better compatibility between the precursor and the organic surfactant by lowering the interfacial energy at the silica-surfactant interface. We chose MTES because methyl groups are the smallest modifying organic chemical units, providing the advantage of keeping the perturbation to the initial (non-hybrid) system to the minimum extent possible.

Samples with variable MTES:TEOS volume ratios were synthesised, using the protocol described in the previous section. The volume ratios were chosen in a range of values, considering that a too

large quantity of MTES would result in a high degree of order, but because MTES contains a non-hydrolysable methyl group, the resulting silica network would be less interlinked, therefore mechanically more unstable. Finally, the volume ratio that gave the best results in terms of mesostructural degree of order was MTES : TEOS = 0.56 : 1. This case will be presented in the reminder of this section.

The mother solution is prepared mixing 3.08 ml of EtOH, 2.84 ml of TEOS, 1.42 ml of MTES and 0.355 ml of a 0.768 M HCl solution. This sol is stirred for 60 minutes, then a templating solution with 15 ml of EtOH, 1.3 g of Pluronic F127 and 1.5 ml of a 0.057 M HCl solution is added. The final molar ratios are: TEOS : MTES : EtOH : H_2O : HCl : Pluronic F127 = 1: 0.56 : 15.56 : 5.20 : 0.018 : $5 \cdot 10^{-3}$. Films were synthesised by dip-coating and treated at 60°C for 1 hour. Subsequently, they were treated at temperatures ranging from 60 to 1000°C, with 1 hour dwell time at the final temperature, in order to study the evolution of mesophase symmetry and framework chemistry with temperature.

3.2.2 Structural characterisation

The GISAXS characterisation data of films treated at 60, 200, 400, 600°C are reported in Figure 3.4. A large number of spots is clearly visible in thermally treated films, extending to the second and third order, while no diffuse ring is present. This is an indication that the films possess a high degree of order. The film treated at 60°C shows only spots belonging to the first order, probably because the electron contrast between the framework and the block copolymer phase is not large enough, whereas at 200°C part of the templating agent has already been removed thus increasing electron contrast and diffraction signal.

In order to identify the mesostructure, we used the GISAXS pattern of the film treated at 200°C because of the presence of a large number of diffraction spots. The spots were obtained from images taken with different exposure times (from 200 ms to 2 s), which were merged into a low-saturation level diffraction image keeping the original positions in the detector. To support the identification of the mesophase, we used the TEM cross-sectional images of the film (obtained by a field-emission gun FEI TECNAI F20 SuperTwin FEG-(S)TEM microscope operating at 200 kV), which showed a 2-fold symmetry axis, probably originating from a 4-fold axis in the as-deposited film which is then broken by the thermal shrinkage (Figure 3.5 a and d). This observation suggested a cubic, tetragonal or orthorhombic symmetry. Then the fast-Fourier transforms of the images were analysed, finding that the patterns are compatible with a *I4/mmm* body-centred tetragonal (BCT) structure (Figure 3.5 b, c, e and f). Finally we performed a simulation of the GISAXS diffraction spots, which gave the s_x and s_y positions of the spots according to the input cell parameters of the

I4/mmm symmetry, X-ray wavelength and sample-to-detector distance, so a graph could be output and superimposed to the experimental GISAXS pattern.

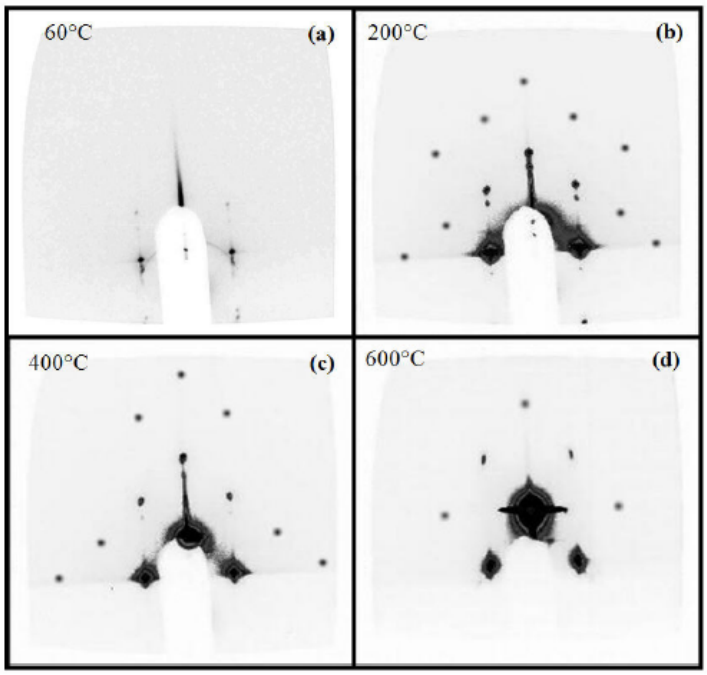

Figure 3.4: GISAXS images of the mesostructured films upon thermal calcination at (a) 60°C, (b) 200°C, (c) 400°C and (d) 600°C.

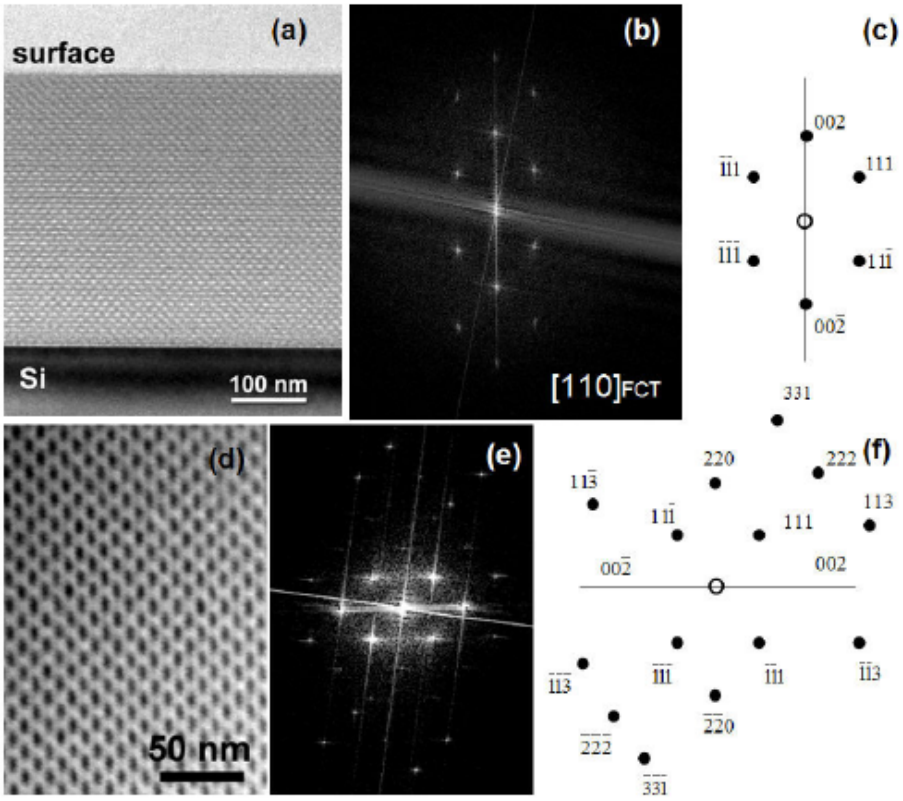

Figure 3.5: (a) Bright-field cross-section TEM image, (b) its Fourier transform, and (c) the correspondent indexation along the [110] direction. (d) Dark-field cross-section TEM image that is rotated 90° with respect to the image in subfigure a, (e) its Fourier transform, and (f) the correspondent indexation along the [110] direction.

Figure 3.6 shows that there is good agreement between the simulated (yellow circles) and the experimental data. Some spots appear to match precisely with the simulated data (red hollow circles) whereas other spots appear shifted with respect to the predicted positions (green hollow circles). This discrepancy affects the spots which are closer to the s_x axis, which are generated by small angle reflections. At first we attributed this discrepancy to a secondary phase in a region of the film, however TEM micrographs reveal a homogeneous mesophase symmetry, therefore we concluded that these shifts are caused by the impinging X-ray and outgoing diffracted beams which undergo multiple reflection events at the film-air and film-substrate interfaces and refraction inside the film, resulting in an alteration in the exit angle which appears to be closer to the s_x axis than it actually is.

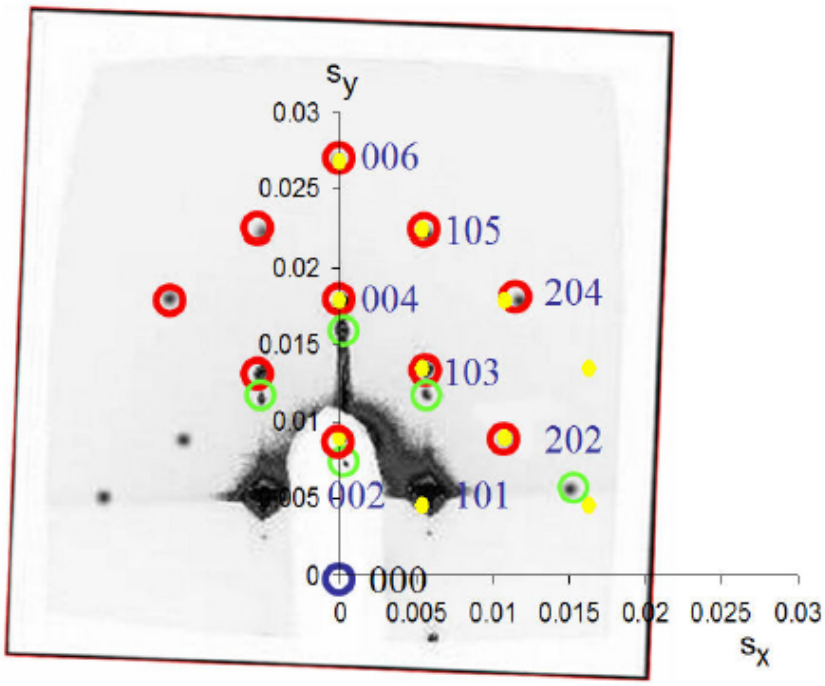

Figure 3.6: Comparison between the GISAXS image of a sample calcined at 200°C and the superimposed simulated spots.

The GISAXS data of the films treated at temperatures higher than 200°C present similar patterns, with a decrease in the d-spacing values of the out-of-plane spots (i.e. along the s_y axis) and no variation in the in-plane spot positions (i.e. along the s_x axis). For all of the patterns (60, 200, 400 and 600°C) the cell parameters were calculated for the corresponding *I4/mmm* structures and we noted that the in-plane *a* cell parameter did not vary significantly upon thermal treatment, whereas the out-of-plane *c* parameter decreased markedly. The *c* cell parameter (calculated by Nanocell software) varied from 23 to 14 nm, whereas *a* =19 nm was unaffected within the error bar.

Therefore, we concluded that a phase transition occurred during thermal treatment between two tetragonal *I4/mmm* symmetries, that is $a < c$ to $a > c$ and the transition temperature was around 450°C. The thermal shrinkage perpendicular to the film surface can be observed in TEM images (Figure 3.5): a deformation of the spherical pores is clearly visible, and the shape of mesopores in calcined samples becomes ellipsoidal.

3.2.3 Spectroscopic characterisation

Information on the presence of specific chemical species in the films was provided by Fourier-transform infrared (FTIR) spectroscopy. This technique gives important insight on the chemical nature of the film and on the self-assembly process. FTIR spectra have been analysed according to the main vibrational modes of interest, reported in Table 3.2.

FTIR absorption spectra of films treated at 60, 200, 400 and 600°C are shown in Figure 3.7. The presence of methyl groups is revealed by the absorption peaks at 1276 cm^{-1} attributed to the C-H symmetrical stretching in CH_3, and 2977 cm^{-1} attributed to antisymmetrical stretching [50]. The intensity of these bands decreases at higher temperatures, indicating a removal of methyl groups from the mesostructure, at 600°C only about 20% of the methyl groups remain in the films due to Si-C cleavage [51]. The calcination of the films is accompanied by a decrease in intensity of the Si-OH stretching band around 950 cm^{-1} and the shift to lower wavenumbers of the Si-O-Si antisymmetric stretching mode around 1070 cm^{-1}, indicating strengthening of the silica network due to polycondensation [52]. The latter band is composed of several overlapped contributions and is generally very difficult to deconvolute [53]. In the present case a clear attribution is more complicated by the overlapping with the absorption bands in the 1050–1175 cm^{-1} interval, which are the most intense modes observed in a pure Pluronic F127 spectrum [54] (in particular, C-O-C stretching at 1110 cm^{-1}, C-C stretching at 1150 cm^{-1}, CH_2 rocking at 1160 cm^{-1}; see Figure 3.8).

The presence of a weak and broad absorption band around 600 cm^{-1}, which is assigned to vibrations of four-member rings within the ring plane (Si-O stretching vibrations coupled with O-Si-O and Si-O-Si bending vibrations) [55], indicates that 4-fold cyclic species are present in the silica framework. We suppose that the vibrational mode at 1135 cm^{-1} is mostly due to antisymmetric stretching (Si-O-Si) in strained 4-fold siloxane rings [56] because Pluronic is nearly completely removed upon thermal calcination at 400°C, as shown by the disappearing C-H stretching bands in the 2700–3000 cm^{-1} region. The formation of 4-fold rings in gels prepared in acidic conditions from MTES is well documented both for powders [57] and films [51] and has been also observed in silica mesostructured films prepared from block copolymers [46].

Wavenumber (cm^{-1})	Vibrational mode
	SiO_2
460	TO_1 (transverse-optical) rocking motion of the O atoms perpendicular to the Si-O-Si plane
800	TO_2 symmetric stretching of Si-O-Si
1070	TO_3 antisymmetric stretching of Si-O-Si
1250	LO_3 (longitudinal optical) higher-frequency shoulder of TO_3
930	Si-OH stretching
550-640	Broad band associated with residual cyclic structures, mainly 4-fold and 6-fold siloxane rings
	Alkoxide
2976	Antisymmetric stretching $\nu_a(CH_3)$
2929	Antisymmetric stretching $\nu_a(CH_2)$
2890	Symmetric stretching $\nu_s(CH_3)$
1365	Antisymmetric rocking δ_a(HCH)
1296	Twisting CH_2
1168	Rocking $\delta(CH_3)$
1106,1103	Antisymmetric stretching ν_a(C-C + C-O)
1082,1080	Antisymmetric stretching ν_a(SiO-CO)
965	Rocking $\delta(H_3CO + COC)$
793	Stretching ν(Si-O + C-O)
670	Symmetric stretching $\nu_s(SiO_4)$
481	Rocking δ(CCO)
	EtOH
3380	Stretching ν(OH) of H-bonded hydroxyls
2975	Antisymmetric stretching $\nu_a(CH_3)$
2894	Symmetric stretching $\nu_s(CH_3)$
1457	Antisymmetric rocking δ_a(HCH)
1274	Twisting CH_3
1090	Antisymmetric stretching ν_a(C-C + C-O), rocking δ(COH)
1049	Rocking $\delta(CCH_3 + COH)$
880	Symmetric stretching ν_s(C-C + C-O) in CH_3 and CH_2
442	Rocking δ(CCO)
	OH
3600-3300	H-bonded OH vibrations of alcohol (O-H stretching)
3500-3300	H-bonded H_2O (O-H stretching)
3800-3650	Stretching modes of OH groups not involved in H-bonding (isolated and terminal OH)
3750	Isolated surface OH
3690	Terminal OH, or partially involved in H-bonding
3650-3200	H-bonded silanols in chain (OH stretching)
1640	Scissor bending of molecular H_2O $\nu_b(H_2O)$
3250	First overtone, bending of molecular H_2O $2\nu_b(H_2O)$
	Organic template
3000-2800	Stretching C-H
2971	Antisymmetric stretching C-H in CH_3
2930	Antisymmetric stretching C-H in CH_2 groups, symmetric stretching C-H in CH_3 groups
2930-2900	CH_2 (methylene) chain symmetric stretching
2871	Symmetric stretching C-H in CH_2
1710	C=O stretching
1500-1300	C-H bending
1374	CH_3 symmetric stretching
1350	CH_2 wagging, C-C stretching in PEO chains
1343	Wagging CH_2
1281,1242	Twisting CH_2
1149	Stretching C-O-C
1113	Stretching C-O-C
1060	Stretching C-O-C, rocking CH_2
963	Rocking CH_2
947	Rocking CH_2, stretching C-O-C

Table 3.2: Assignments of the IR vibrational modes belonging to different chemical species in mesostructured and mesoporous thin films.

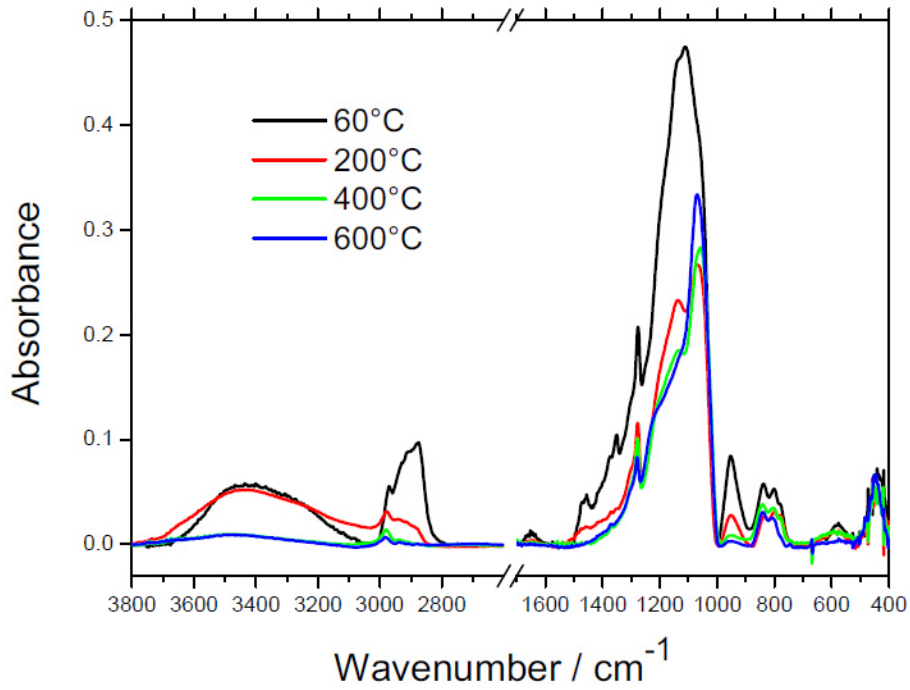

Figure 3.7: FTIR absorption spectra, collected in air, of films treated at 60, 200, 400 and 600°C.

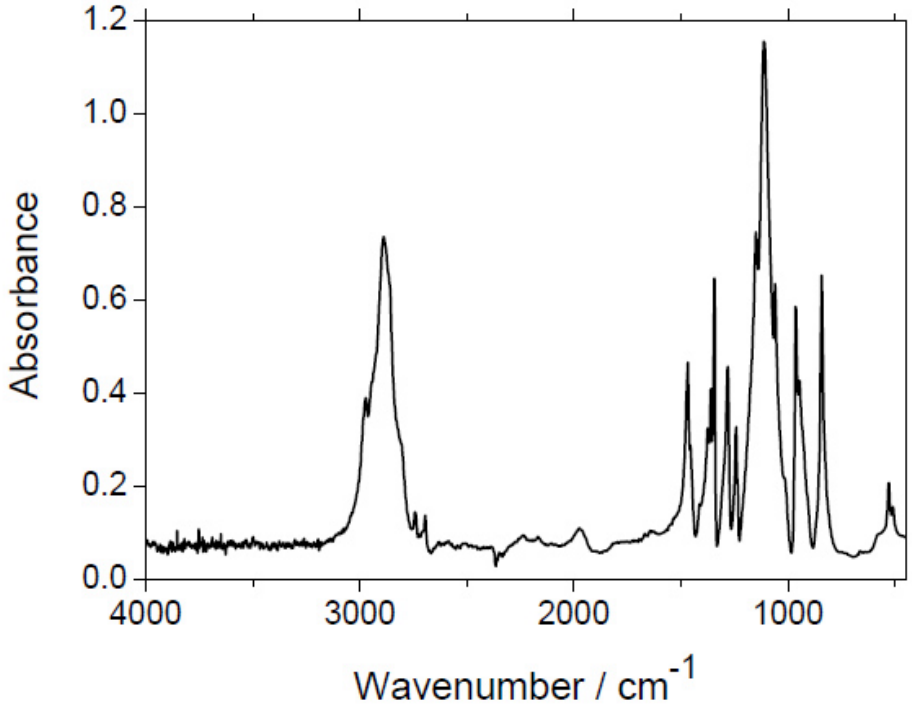

Figure 3.8: FTIR absorption spectrum of block copolymer Pluronic F127 diluted in a KBr pellet.

Calcination of the films causes dehydroxylation and a change in the amount of methyl groups present in the mesopores. These two processes are simultaneous and affect the hydrophobicity of the system and, hence, the ability to absorb water. To evaluate how the thermal calcination is affecting this process we have performed a deconvolution of the FTIR spectra in the range ~ 3000–

3800 cm^{-1} (Figure 3.9). To deconvolute the FTIR spectrum of the sample treated at 60°C we selected three components: (1) at the highest wavenumber assigned to terminal silanols, (2) at ~ 3350 cm^{-1} due to hydrogen-bonded silanols in chains that contain more than one pair of mutually H-bonded OH groups, and (3) at ~ 3250 cm^{-1} attributed to the first overtone of the 1640 cm^{-1} bending mode of molecular water $2\nu_b(H_2O)$ [52,58,59,60]. In the fit of the samples treated at higher temperatures (200, 400 and 600°C) we introduced another component due to the isolated silanols that are formed during dehydroxylation (~ 3650 cm^{-1}). The deconvolution shows a decrease in intensity of all the components after calcination at 200°C. The dehydroxylation is practically complete at 400°C, because only weak traces of terminal and isolated silanols are observed, without residual water. If the sample is treated at higher temperatures new silanols are formed and a small amount of water is absorbed (600°C).

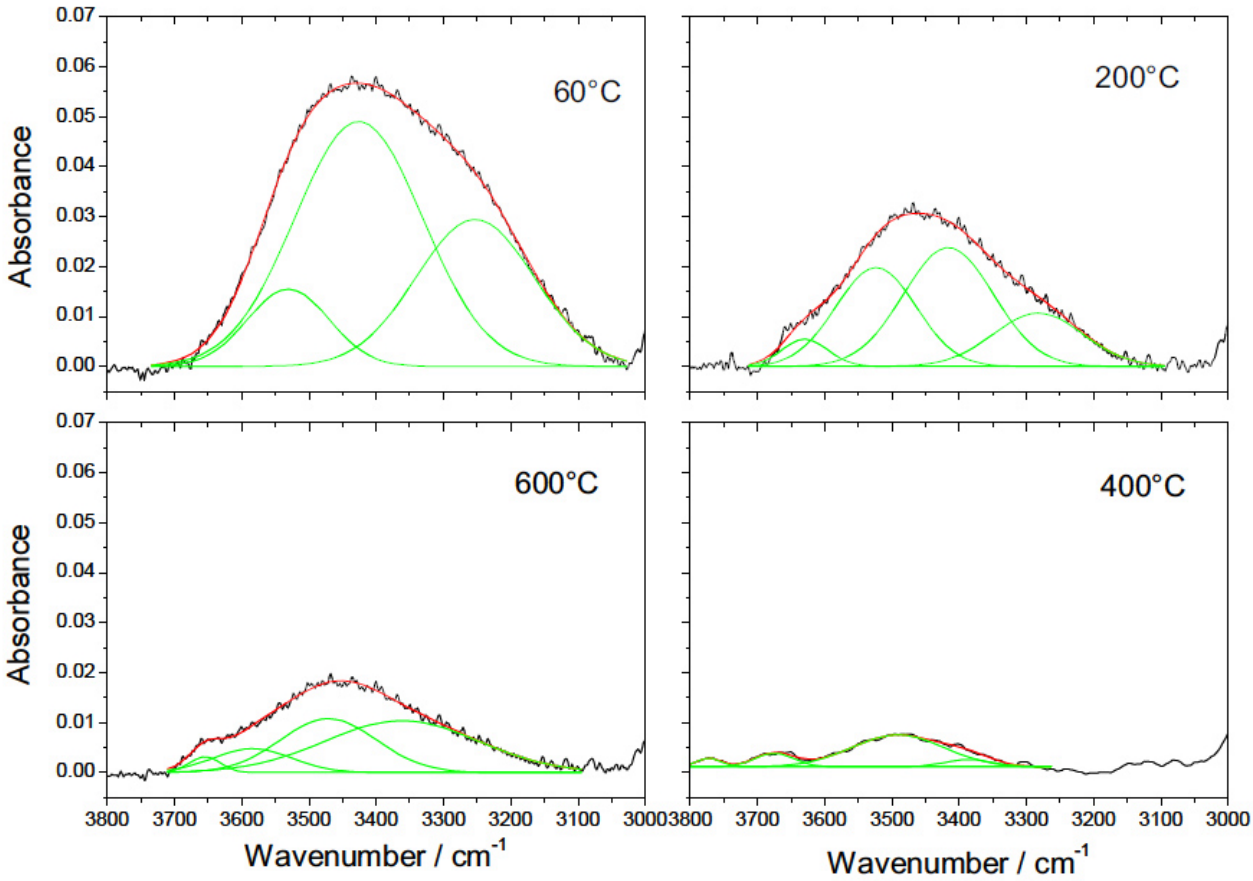

Figure 3.9: Deconvolution of the FTIR spectra in the range 3000–3800 cm^{-1} for films treated at 60, 200, 400 and 600°C.

This trend can be explained as follows. At 60°C the pores are filled with the block copolymer whose hydrophilic chains are able to absorb and retain water, at the same time the pore walls are covered with hydrophilic silanols. In these conditions, the hydrophobicity of methyl groups is largely shadowed. When the surfactant is completely removed upon calcination at 400°C, the pores

are covered only by methyl groups and the absorption of water is inhibited. At 600°C the methyl groups are removed forming silanols [61]. The curve obtained from the deconvolution that is assigned to the $2\nu_b(H_2O)$ contribution (overtone of the bending mode of molecular water at ~ 3200 cm^{-1}) was used to qualitatively investigate the change in water absorption during thermal calcination. A plot of the peak area vs. temperature shows that the presence of H_2O has a minimum at 400°C (Figure 3.10). The data obtained from the $\nu_b(H_2O)$ at 1640 cm^{-1} are in agreement with those calculated from the deconvolution, supporting the choice done for the fit.

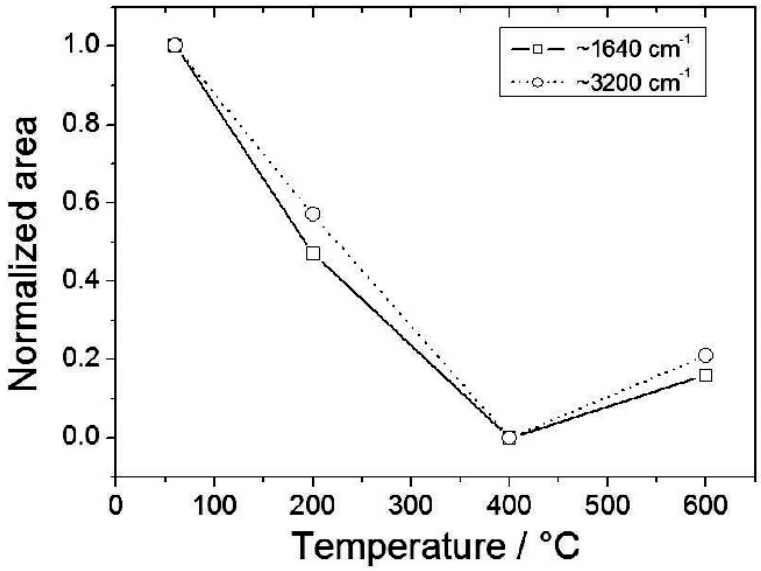

Figure 3.10: Area variation of peaks attributed to □$_b(H_2O)$ at 1640 cm^{-1} (hollow squares) and 2□$_b(H_2O)$ at 3200 cm^{-1} (hollow circles) as a function of film thermal treatment.

The transversal vibrational TO_3 mode (Si-O-Si antisymmetric stretching) at ~ 1070 cm^{-1} has a shoulder at ~ 1200 cm^{-1} (longitudinal LO_3 mode). With increasing temperature, the intensity of TO_3 shifts towards higher wavenumbers, indicating higher degree of silica polycondensation. This shift can be observed also in films obtained without MTES (i.e. where TEOS is the only silica source). However, the two shifts have a different trend, which can give insight into the polycondensation process. Figure 3.11 shows the wavenumber peak of the TO_3 mode for mesostructured silica (TEOS) and organosilica (TEOS-MTES) films. The slope of the organosilica films is steeper for temperatures below 700°C with respect to the silica films, whereas for temperatures above 700°C the two wavenumbers become similar. The shift of the TO_3 mode towards higher wavenumbers is related to the higher degree of crosslinking of the inorganic network. According to the central force model by Galeener [62] (Figure 3.12), the frequency *w* of the TO_3 mode is:

$$\omega^2 = \frac{k}{m_O}(1-\cos\theta) + \frac{4k}{3m_{Si}}$$

where m_O and m_{Si} are the O and Si masses, k is the constant of the stretching in Si-O-Si and q is the angle formed by the Si-O-Si bond. Increasing polycondensation degree, the average Si-O bond distance decreases and k increases; at the same time, the average θ increases, causing ω to increase.

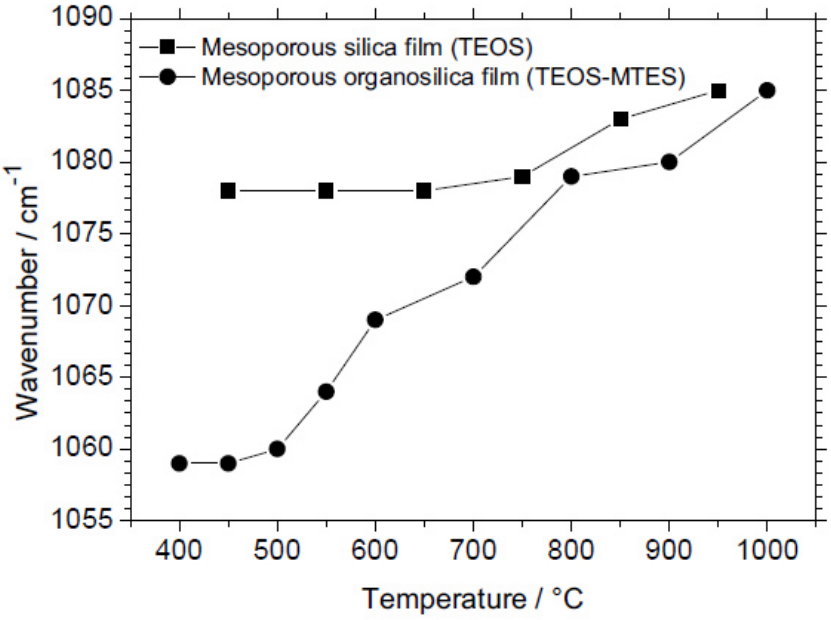

Figure 3.11: Trend of the TO_3 peak position as a function of temperature for mesoporous silica (TEOS) and organosilica (TEOS-MTES) films.

This observation suggests that the presence of non-hydrolysable methyl groups in the organosilica films is associated with a lower polycondensation degree than in silica films (for the same thermal treatment). The methyl groups inhibit further polycondensation until they are fully removed between 600 and 700°C: then the Si atoms can bond to four bridging oxygens thus increasing the overall polycondensation degree. The peak positions shift to a limit value of 1085 cm^{-1} (at ~ 1000°C), when silica densification is complete and the mesopores collapse due to silica viscous flow. Temperatures below 400°C (removal of organic template) were not considered in this analysis, as the overlap of the bands arising from the copolymer are superimposed to the TO_3 mode causing the wavenumber shift to be uncorrelated to the polycondensation degree.

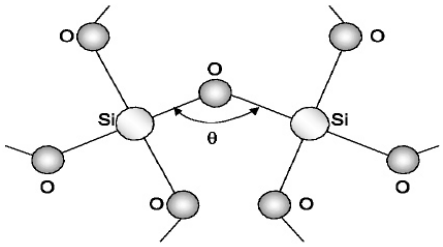

Figure 3.12: Scheme of local order according to Galeener's model.

Methyl groups perform an important role to help self-assembly, in that they affect the micelle-silica interface and the kinetics of the reactions of the species involved in EISA. The strong electrostatic and hydrophilic interactions between the silica and the PEO blocks are reduced by the presence of CH_3 in the silica oligomers. At the same time, k_{inorg} results smaller because of the presence of the non-hydrolysable Si-CH_3 groups, allowing for a high degree of organisation, so organisation of the micelles is not hindered by a more condensed inorganic network and a faster organisation occurs. In other words, we observe a twofold effect: (1) the inorganic condensation rate and condensation degree are lowered by the presence of non-hydrolysable units, so that only three bridging oxygens per Si atom can form a network instead of four as in TEOS; (2) the hydrophobic methyl units act as a "co-surfactant" between the inorganic units and the organic micelles.

These films are hygroscopic due to the high amount of hydroxyl groups and extremely high surface area. Contact angle measurements have not been performed, however Figure 3.13 gives a hint about the hydrophobicity of a hybrid (TEOS-MTES) mesoporous silica film compared to a silica (TEOS) mesoporous film. Moreover, the introduction of organic methyl groups into the inorganic framework decreases mechanical stress in the silica gel during solvent evaporation and densification: this reduces the probability of cracking and increases the critical thickness of the film (i.e. the maximum thickness that can be obtained without crack formation) to thicknesses greater than 1 μm.

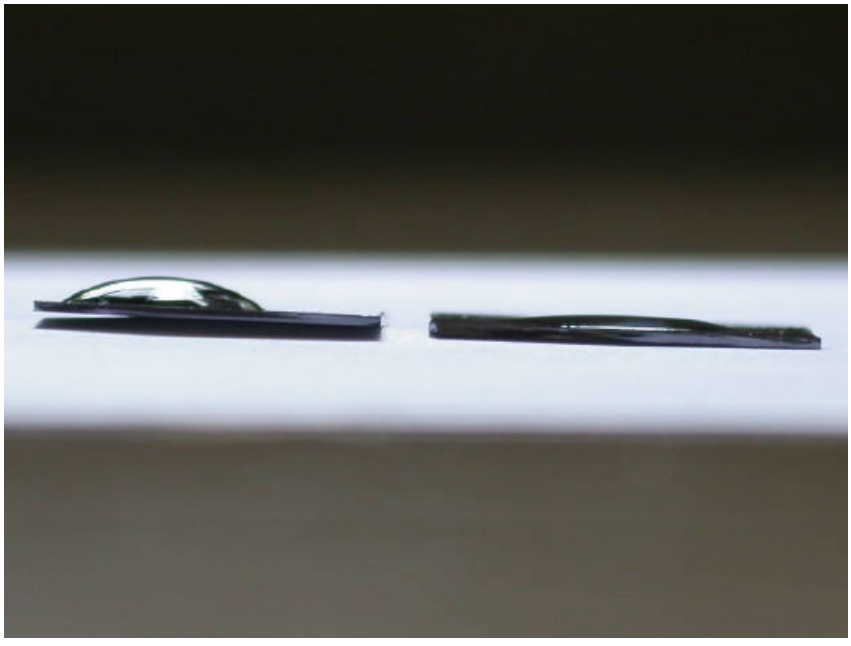

Figure 3.13: Different hydrophobicity of a hybrid mesoporous film (left) and inorganic silica mesoporous film (right). Note the different contact angle, higher in the hybrid film and lower in the inorganic one.

3.3 Hybrid mesoporous membranes

3.3.1 Synthesis protocol

Membranes are defined as thin physical barriers allowing selective transport of mass species. They must be prepared either on a porous support allowing transport of mass species, or as self-standing objects. Mesoporous and macroporous films and membranes have been studied extensively in the past decades and many of them have found commercial applications. Whereas there are many publications on mesoporous films and powders, only a small number of papers deal with mesoporous membranes. Soler-Illia et al. [24] report on the preparation of membranes synthesised starting from an acidic solution of alkoxysilane and an amphiphilic block copolymer (Pluronic F127 or P123). In this section we describe the study on silica and hybrid organosilica self-standing mesostructured and mesoporous membranes. We have performed structural characterisation by SAXS and studied the physicochemical properties of the pore surface and the mechanism of water adsorption-desorption by Fourier-transform infrared spectroscopy in vacuum at different partial air pressures.

Self-standing inorganic and hybrid organic/inorganic mesoporous silica membranes were synthesised by the EISA route, in the shape of disks with about 30 μm of thickness and 80 mm diameter. A precursor solution containing the silicon source and the templating agent (the same used in the preparation of silica and hybrid films, described in the previous sections) was poured into a polystyrene Petri dish and the solvent was allowed to evaporate slowly in a controlled environment (RH~40% and T=25°C) for approximately 60 days. After drying, the membranes could be detached from the bottom of the container using tweezers, then they were submitted to thermal treatment for surfactant removal. The membranes were calcined in a furnace under a chemical hood in order to remove the vapours originating from template decomposition, with a heating ramp of 1°C/min from room temperature to 350°C with a dwell time at 350°C of 12 hours. After calcination, the membranes became brittle and prone to breaking into fragments of several centimetres, partially losing their transparency. TEOS-MTES-F127 and TEOS-F127 membranes will be hereafter referred to as M and T, respectively.

3.3.2 Structural characterisation

As-prepared and thermally treated T and M membranes were broken into fragments so that they could be investigated by grazing incidence and transmission SAXS. Figure 3.14 shows a representative GISAXS pattern of an uncalcined M membrane. This GISAXS pattern was attributed to the cubic Im3m symmetry group as the result of simulations using the Nanocell software for

Mathematica. The M membranes yielded the same diffraction pattern, with a slight difference in the cell constant values. It is a = (16.3±1.1) nm for the as-prepared hybrid membrane and shows a contraction of 28% upon calcination. In the T membranes the cell constant is a = (18.0±1.0) nm and a contraction of 22% is induced by calcination. The shrinkage is isotropic, contrary to films, where uniaxial contraction perpendicular to the substrate is always observed.

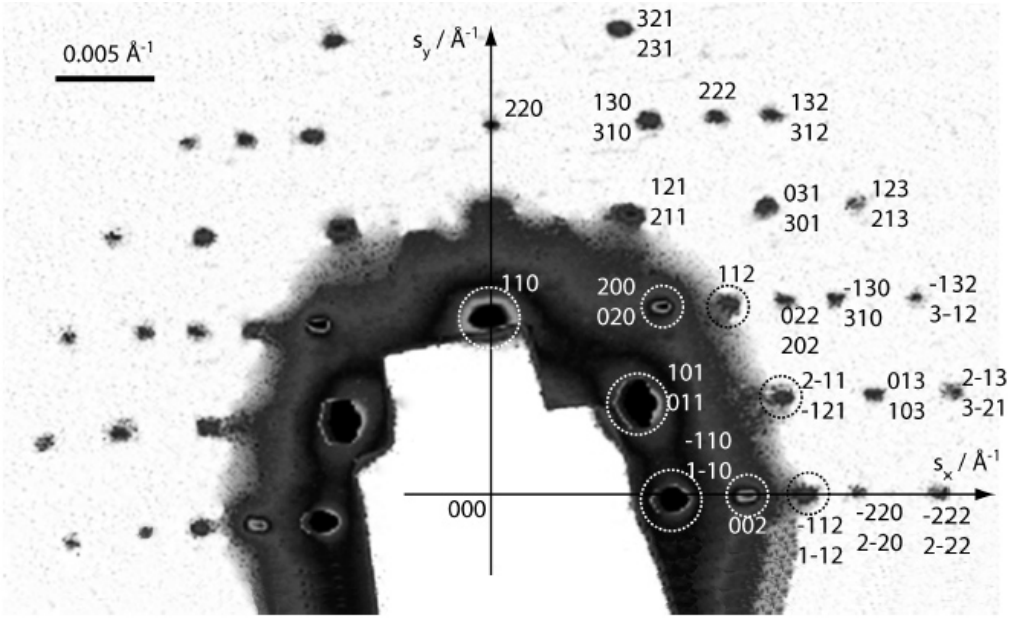

Figure 3.14: GISAXS diffraction pattern of the as-prepared organosilica membrane obtained from a solution containing TEOS and MTES as the Si source, and its full indexation according to the cubic Im3m symmetry.

In another experiment we have tried to increase the evaporation rate by placing the Petri dishes containing the precursor solutions under a chemical hood. In a few days the membranes dried, however they gave no appreciable signal in GISAXS measurements. This indicates that there is no ordered mesostructure in the membrane, suggesting that evaporation must be slow in order for self-assembly to occur and create an ordered pore array, and that objects thicker than films require slower solvent evaporation. Moreover, both the T and the M membranes show the same mesophase symmetry with a high degree of order and only a slight difference in the cell parameters, so, contrarily to films, the role of the methyl groups does not seem to be so critical to affect the final structure. This is probably due to the particularly slow solvent evaporation that may favour a more thermodynamic and less kinetic control on the formation of the mesostructure.

Different portions of the membranes were sampled by SAXS to ensure that the ordered mesophase extended in the whole membrane. The use of a sample holder equipped with an x-y stage system (parallel to the membrane surface) allowed the sampling of the T membrane along two orthogonal directions with steps of 10 mm (Figure 3.15). Nine different SAXS diffraction patterns, recorded in transmission mode, are shown in Figure 3.15 a, and the corresponding positions in the membrane

are reported in Figure 3.15 b. Comparing the SAXS patterns taken starting from the centre of the membranes towards the outer region, it is possible to detect the presence of the ordered mesophase in the central region of the membrane within a radius of 30 mm. The presence of spots both in the transmission and grazing diffraction patterns relative to this inner region shows that the mesostructure has both in-plane and out-of-plane order, which is a feature not commonly observed in mesoporous materials. The SAXS patterns show only a small rotation (around 3–4°) from the centre of the membranes (snapshot 5) to the external areas, corresponding to an in-plane rotation of the mesostructure (see Figure 3.15 c). In the outer region of the membrane (indicatively beyond the zone delimited by the 30 mm radius), the in-plane order is lost, but the out-of-plane order of the mesostructure is retained, as confirmed by the presence of diffraction rings in transmission mode (not shown in figure). This phenomenon is probably caused by an increase in the radius of curvature of the membrane surface, affecting the peripheral regions of the samples. Because the precursor sol wets the container's walls creating a meniscus, the final membrane thickness rises from 30 μm in the membrane centre to 48 μm at the edges. As already reported [63], the self-assembly of micelles starts from the interfaces, therefore the smaller radius of curvature can determine a gradient in the evaporation rate of solvent and, in turn, the loss of order.

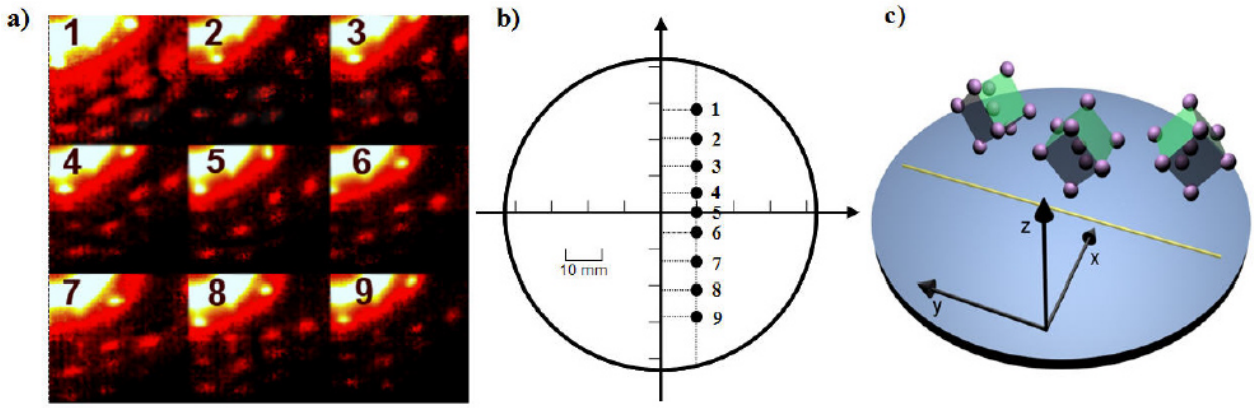

Figure 3.15: SAXS sampling (transmission mode) of the inorganic mesostructured membrane with steps of 10 mm (a) and drawing of the corresponding positions along the membrane diameter (b). Picture of the rotation of the mesostructure from the centre of the membranes (snapshot 5) towards the outer regions (c).

TEM images were collected to support the information provided by SAXS data. Figure 3.16 shows four representative bright field images of the M (a and b) and T (c and d) membranes thermally treated at 350°C, whereas the uncalcined samples did not give significant images due to the small electronic contrast between the framework and the templating phase. The presence of 4-fold symmetry axes suggests that the structure is cubic. By a line profile analysis on a representative TEM image showing the (100) projection plane (Figure 3.16 e) we estimated pore diameter and wall thickness as the average FWHM of the intensity distribution along a line passing through the

pore centres (red line in figure). Pore diameter in organosilica membranes is (6±1) nm and wall thickness is (3.3±0.5) nm. Thus the average centre-to-centre distance of two adjacent pores is ~ 4.5 nm. Due to the merging of planes, the (100) projection plane shows the pores both at the cube vertices and at the centre of the unit cell. Therefore, the interpore distance represents half the diagonal of a face of the cubic unit cell and must be multiplied by $2\sqrt{2}$ in order to get the cell parameter a, which gives $a \sim 12$ nm, a value in agreement with SAXS data. Similar results were obtained for the inorganic silica membranes.

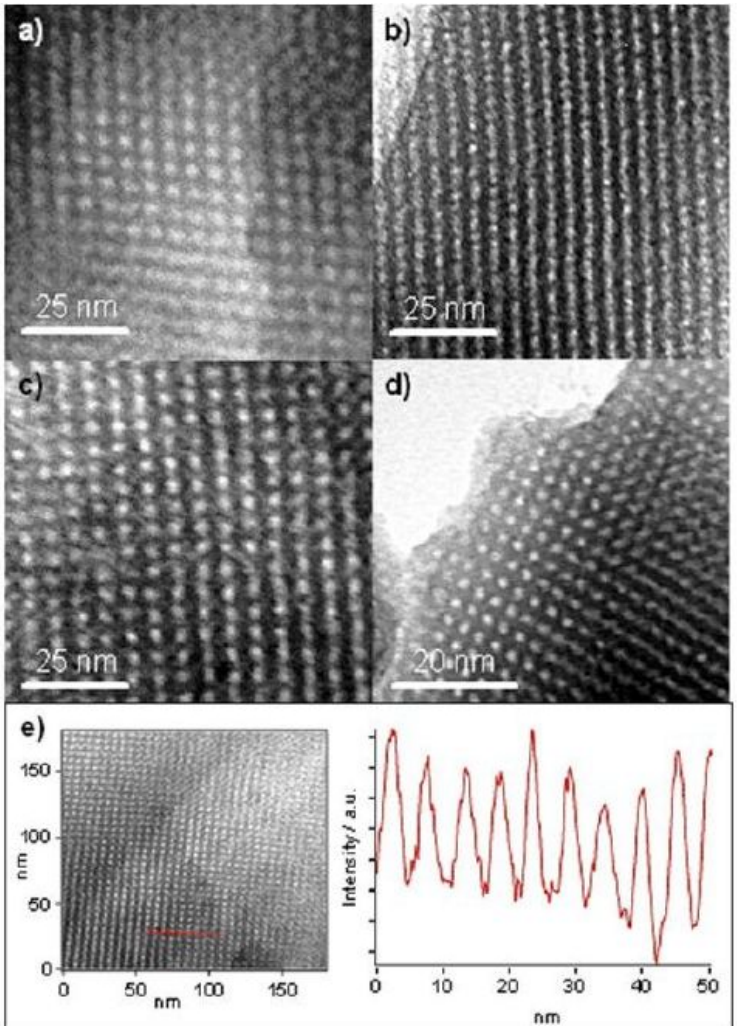

Figure 3.16: Bright field TEM images for samples calcined at 350°C. Four different images of T (a and b) and M (c and d) membranes are shown; (e) represents the line profile analysis (right side) of a M membrane to evaluate pore and walls dimensions.

3.3.3 Spectroscopic analysis at low pressure

FTIR spectroscopy of the membranes was performed at the synchrotron infrared beamline SINBAD at the INFN Laboratori Nazionali di Frascati. The equipment used was a Bruker Equinox 55 interferometer with a conventional Globar source. To investigate the desorption kinetics of chemical moieties physically adsorbed on the pore surface, the interferometer was equipped with a

vacuum chamber that worked down to 10^{-3} mbar. Measurements were carried out at different pressures in transmission mode using the interferometer working in the 500–6000 cm^{-1} range at a resolution of 4 cm^{-1}. A mercury-cadmium-telluride (MCT) detector cooled with liquid nitrogen and a KBr beam splitter were used.

Fig. 3.17 shows the FTIR absorption spectra of the T sample, calcined at 350°C, recorded in the 2800–3800 cm^{-1} range as a function of the pressure within the vacuum chamber. At atmospheric pressure the spectra are saturated so that the first significant spectrum was collected at 0.5 mbar.

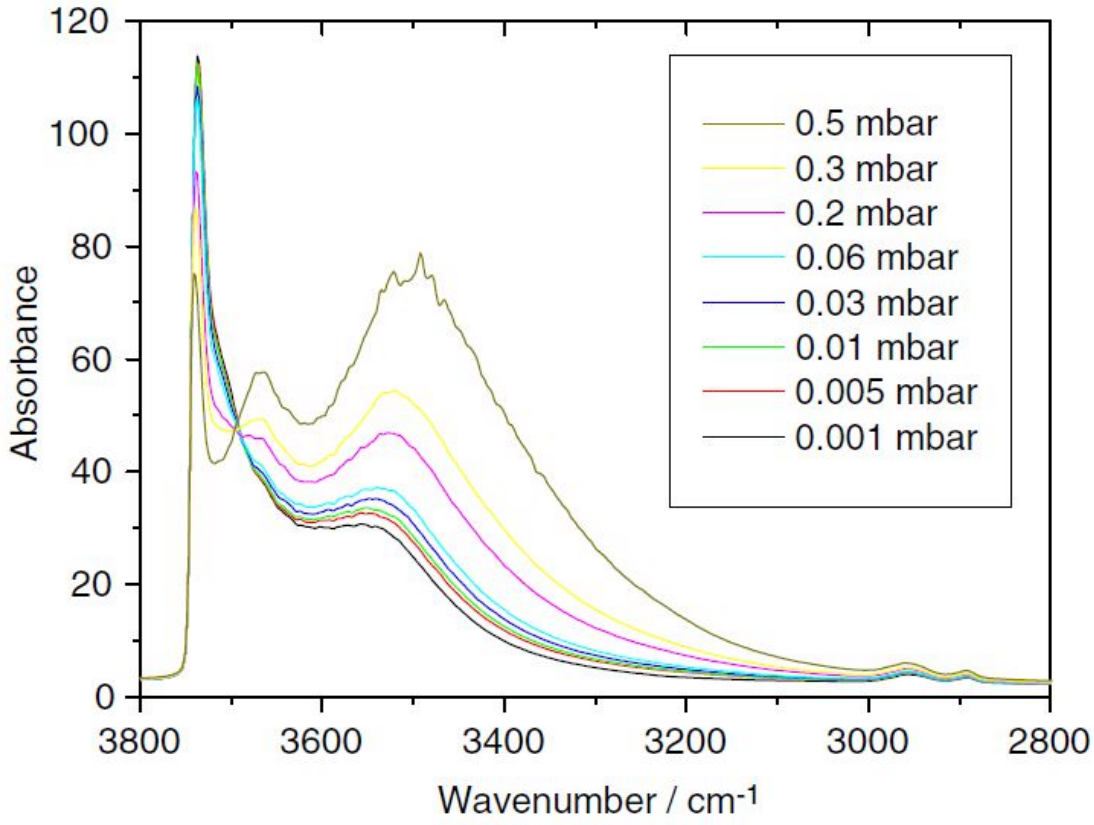

Figure 3.17: FTIR absorption spectra of the T silica membranes after calcination at 350°C, in the 2800–3800 cm^{-1} range, taken at decreasing pressures within the experimental chamber.

The relative intensity of the main vibrational modes [52,64] observed around 3500, 3650 and 3750 cm^{-1}, are directly affected by pressure. The broad band peaking around 3500 cm^{-1} decreases in intensity and shifts to higher energies as vacuum pressure is increased. The maximum of the band shifts from 3494 cm^{-1} in the spectrum recorded at 0.5 mbar, to 3547 cm^{-1} in the spectrum measured at 0.001 mbar. The shape of the ~3500 cm^{-1} band and its changes versus pressure suggest that different contributions are responsible for these variations. At ~3500 cm^{-1} there is a contribution (3510 cm^{-1} in silica glass [65]) from OH stretching of silanols that are hydrogen bonded to the oxygen of neighbouring silanols (ν_s(OH· · ·^{H}OSi)) [64], whilst the presence of adsorbed water vapours from the atmosphere gives rise to two bands in the 3000–3500 cm^{-1} region that overlap with the ν_s(OH) band of silanols. A first water band falls at higher energies, around 3450 cm^{-1}, and

is assigned to molecular water that is directly bonded to the silica network ($\nu_{as}(H_2O)$) or hydrogen-bonded to the silanol groups, $\nu_s(H_2O)$. Generally, the molecular water directly attached to the silica network is more strongly bonded than the silanol bonded water, but the two contributions are very difficult to separate. The second band due to molecular water that is assigned to the first overtone of the bending mode of H-bonded water ($2\nu_b$), falls at lower energy, around 3200 cm^{-1}. The changes observed in the low wavenumbers tail of the 3500 cm^{-1} band (the band shrinks and the tail disappears in the spectra from 0.5 up to 0.06 mbar) indicate the water removal at lower pressures (Fig. 3.17). In accordance, the intensity decrease and shift of the 3500 cm^{-1} band is also attributed to removal of residual H-bonded water.

We have used the band at 1628 cm^{-1} (ν_b, water bending) [66] to follow the desorption of water induced by the pressure changes (Fig. 3.18a). This band is not overlapped to other species and can give a direct semi-quantitative indication of water desorption. The asymmetric shape of the band suggests that different types of water are present within the membrane pores at ambient pressure. Following the literature, three different vibrational components due to molecular water can be observed: water molecules that aggregate with strong hydrogen bonding (~1676 cm^{-1}) (type I), water molecule clusters with moderate intensity of hydrogen bonding (~1654 cm^{-1}) (type II) and water molecules that interact with each other with weak hydrogen bonding (~1592 cm^{-1}) (type III) [67]. Generally, a lower absorption wavenumber is an indication of a decrease in the strength of the hydrogen bonding, and type III of hydrogen bond is so weak that the water involved can be considered as ‘‘free’’ water. Fig. 3.18b shows a deconvolution of the water band and the three components of water bending modes were resolved by Gaussian curves. Only two components are, however, resolved with a significant intensity (I and II). The component III is, instead, very weak, which is an indication that almost no ‘‘free’’ water is present within the pores. Whilst at ambient pressure the sample adsorbs water that is hydrogen bonded on the pore surface through the silanols, at 0.06 mbar the water is completely removed, in accordance with the spectra in Fig. 3.17 (3200 cm^{-1} component). Furthermore, because most of the water is easily desorbed at 0.5 mbar (Fig. 3.17), the amount of water directly bonded to the silica network is negligible. At higher wavenumbers, in the 3800–2800 cm^{-1} region, the FTIR spectra show three other vibrational modes, which change in intensity with the variation of the pressure: at 3670, at 3708 (shoulder) and at 3737 cm^{-1} (sharp) (Fig. 3.17). The 3670 cm^{-1} band is assigned to OH stretching of SiOH with a contribution from antisymmetric stretching of hydrogen bonded molecular water ($\nu_{as}(H_2O)$) [64]. The decrease in intensity of this band at higher vacuum pressures indicates that the contribution from molecular water is predominant. On the other hand, the intensity decrease of this mode is accompanied by a simultaneous increase of the 3708 and 3737 cm^{-1} bands. We attribute the 3708 cm^{-1} band to geminal

silanols and the 3737 cm^{-1} to isolated silanols [68]. The removal of the bridging water can induce a condensation between adjacent silanols that will form twin species or will give new isolated silanols.

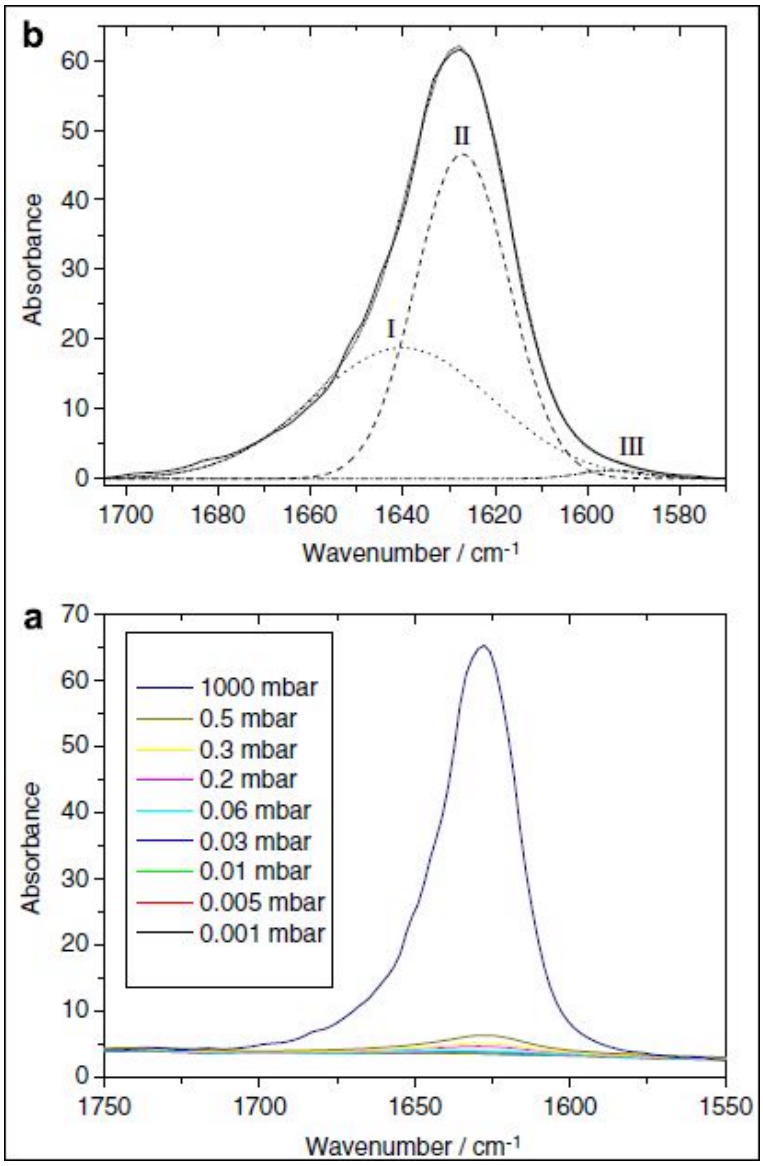

Figure 3.18: (a) 1628 cm^{-1} (δ_b, water bending) as a function of the pressure changes in the experimental chamber. (b) Deconvolution of the water band, the three components (I (dot line), II (dash line) and III (dash-dot line)) of water bending modes were resolved by Gaussian curves. The short dot line represents the three components Gaussian fit of the experimental data.

Fig. 3.19 shows the picture of the different silanol species and their changes activated by water desorption, as previously described. The FTIR measurements performed in vacuum vs. pressure directly confirm that the pores of the membranes are fully accessible from the external environment, as shown by the full removal of the adsorbed atmospheric water. The process of adsorption–desorption is also reversible and it appears related with the nature of the pore surface. On the basis of FTIR data it should be noted that at ambient pressure the pore surface, in silica based mesoporous materials, is in any case covered by at least one layer of hydrogen bonded atmospheric

water linked to the residual silanols. Such layer that is responsible for the high protonic conductivity of silica mesoporous materials and their application as electrochemical sensors [69,70].

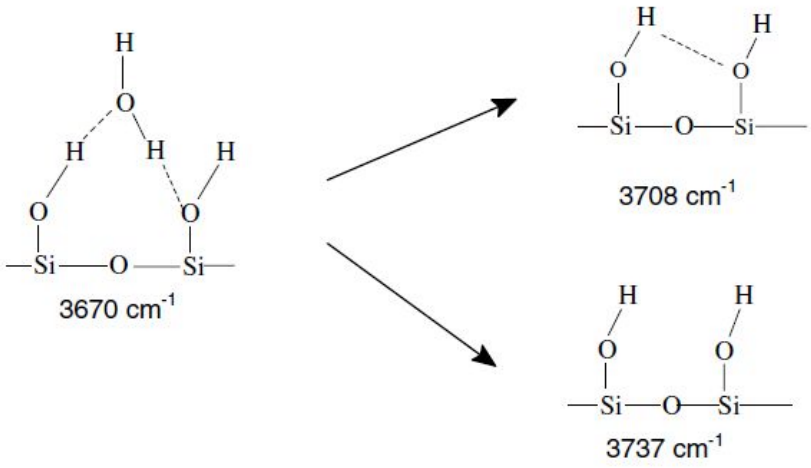

Figure 3.19: Drawing of the surface species detected by FTIR: the water molecules bridge two close silanols, which after water removal become isolated silanols or geminal silanols upon condensation.

The changes induced by the pressure and the correlation between the different species can be better described by 2D FTIR data analysis. 2D infrared spectroscopy has been applied to investigate the synchronous changes in the 3000-3800 cm^{-1} region induced by change of partial pressure. Fig. 3.20 shows the schematic contour map of the synchronous 2D FTIR correlation spectrum of the T sample. A colour scale is used to indicate the intensity changes.

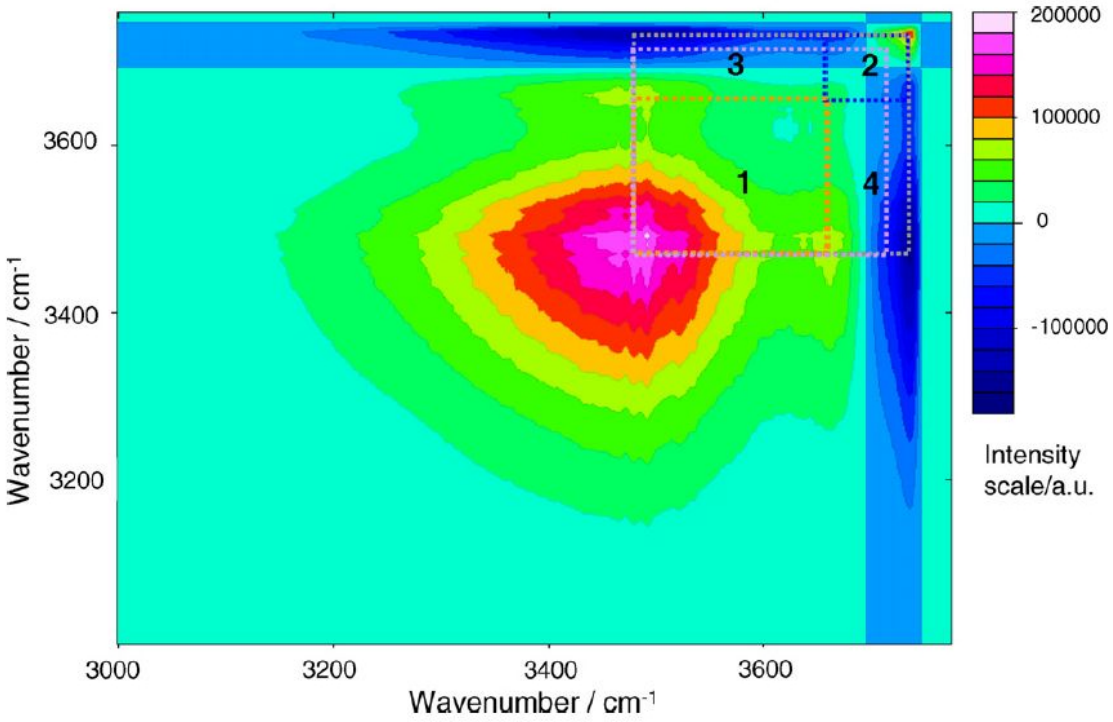

Figure 3.20: Schematic contour map of the synchronous 2D FTIR correlation spectrum of the T sample.

Four distinct autopeaks of different intensities are observed in the diagonal from right top to left bottom of the contour map, at the wavenumbers around 3500, 3650, 3710 and 3740 cm^{-1}. The autopeaks correspond to the region of the spectrum that show intensity variations induced by the change of the external variable, which in this case is pressure (from 0.5 mbar down to 0.001 mbar). The autopeaks are all positive, whilst the cross-peaks can be either positive or negative. Four correlation squares, joining pairs of cross-peaks located at the opposite sides of the diagonal line can be drawn, indicating the existence of coherent changes of spectral intensities with partial pressure. In particular, correlation squares (CS) between the autopeaks at 3500 and 3650 cm^{-1} (CS1), at 3650 and 3740 cm^{-1} (CS2), at 3500 and 3740 cm^{-1} (CS3) and 3500 and 3710 cm^{-1} (CS4) can be built. The correlation squares indicate a related origin of the spectral intensity changes by the pressure change on the membranes. Whilst the signs in the CS1 between the autopeaks at 3500 and 3650 cm^{-1} and the relative cross-peaks are all positive, in the other correlation squares (CS2 and CS3) the signs of the autopeaks are always positive and the signs of the cross-peaks always negative. The signs of the species in the CSs indicate that the reduction of the partial pressure is directly correlated with a decrease of hydrogen bonded water, which leads to the appearance of isolated Si–OH (CS3) or geminal silanols (CS4). The positive sign observed in both cross-peaks and autopeaks in CS1 indicate that the two species at 3500 and 3650 cm^{-1} show intensity changes with partial pressure in the same direction. They decrease or increase in intensity in accordance and this is a good support to the assignment of their origin to hydrogen bonded water.

The FTIR spectra of hybrid M membranes show a trend similar to that observed in the T membranes, but with some important differences. Fig. 3.21 shows the FTIR absorption spectra of the hybrid membrane after calcination at 350°C, in the 2800–3800 cm^{-1} range vs. pressure. The calcination temperature is effective in removing the surfactant, but at this temperature the methyl groups are not removed from the mesoporous membrane. The thermal treatment temperature (350°C) has been selected to allow surfactant removing without degradation of the methyl species [71,72]. In addition, the different behaviour with respect to water adsorption can also give a clue about the location of the hydrophobic methyl groups since the spectra are not saturated at ambient pressure, and at 300 mbar all the traces of residual adsorbed atmospheric water (~3200 cm^{-1} band) are removed. This suggests that most pore surface is covered by methyl groups [73] which make the pore surface of the M membranes partially hydrophobic. Thus, in M membranes a weaker signal is observed for adsorbed water, as opposed to T membranes where adsorbed water may even cause saturation of the FTIR spectra. This supports the fact that after removal of residual water no other changes on the pore surface can be observed and that isolated silanols do not react with each other.

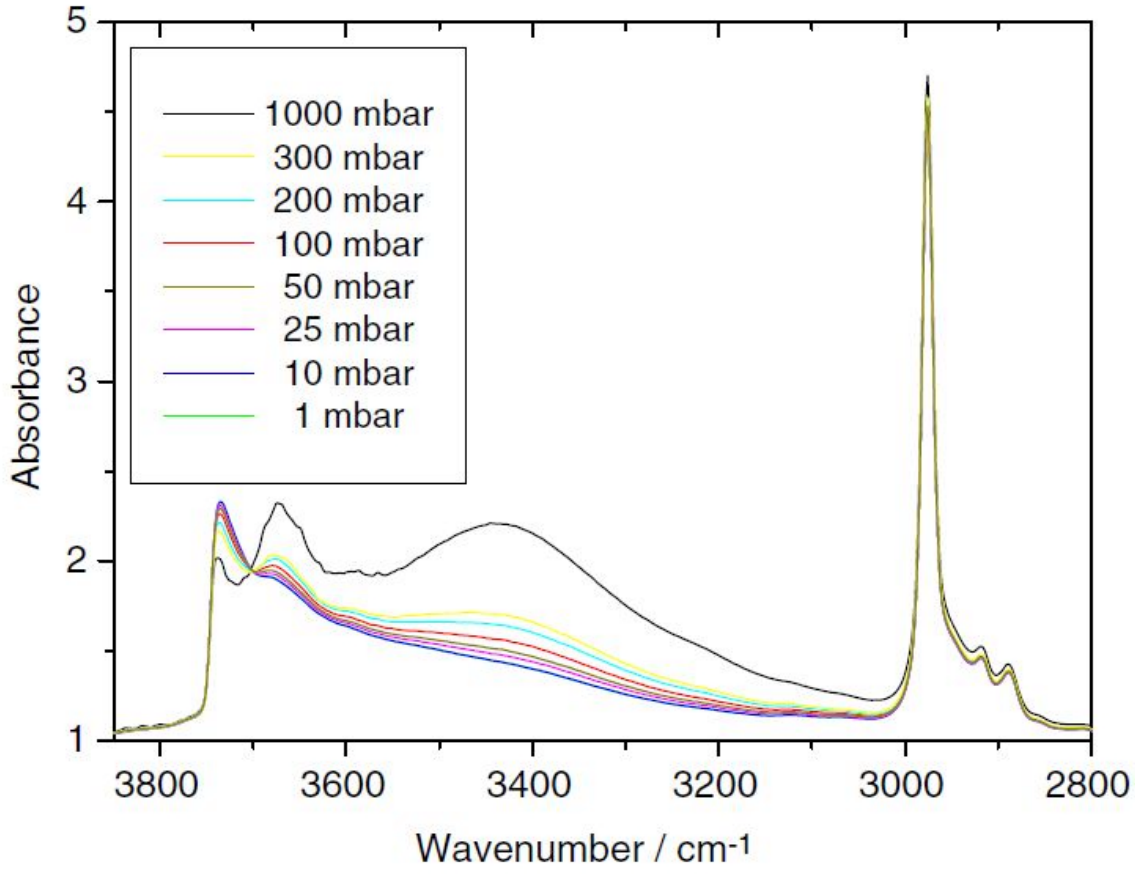

Figure 3.21: FTIR absorption spectra of the M membrane after calcination at 350°C, in the 2800–3800 cm^{-1} range, at decreasing pressures.

3.4 EISA of mesoporous silica films studied by in-situ time-resolved FTIR spectroscopy

Sol–gel processing of thin films involves time dependent phenomena which are basically driven by solvent evaporation (i.e. EISA). The possibility to follow in-situ as a function of time the evolution of the system can give a better knowledge of the process and the physics and chemistry beneath. Time-resolved analytical methods are important tools to follow the evolution of films deposited via a liquid phase because the overall process is also a typical time-dependent phenomenon. The time scale is generally in the order of several seconds, depending on the processing parameters, such as the withdrawal speed during dip-coating, the type of solvent and the amount of solvent employed, the relative humidity in the deposition room. In the simplest case ethanol as solvent and water for hydrolysis or as by product of the sol–gel reactions are present in the precursor sol; they have different evaporation rates and a fundamental role in the process. Time-resolved IR spectroscopy is a quite simple and relatively fast technique and it is the ideal tool to study the chemical processes

occurring during deposition of films by a liquid phase, as it allows time-resolved (from ms to s) and in-situ analysis of chemical phenomena correlated to solvent evaporation. We have applied this technique to several cases and we have obtained detailed insight views of the evaporation and related phenomena during the deposition of sol–gel silica films.

Silica sols were prepared using tetraethyl orthosilicate (TEOS), H_2O, ethanol (EtOH), HCl, and a triblock copolymer (Pluronic F127) as templating agent, with the following final molar ratios of reagents: TEOS : EtOH : H_2O : HCl : F127 = 1 : 24.48 : 14.70 : 0.11 : $7.6x10^{-3}$. To prepare the precursor silica sol, we prepared a stock solution by adding EtOH, TEOS, water, and HCl in this order in the following molar ratios: TEOS : EtOH : H_2O : HCl = 1 : 2.78 : 1.04 : $56.2x10^{-3}$. The sol was left to react for 1 hour under stirring at room temperature. A second solution was prepared by dissolving 1.3 g of Pluronic F127 in 15 cm^3 of EtOH and 1.5 cm^3 of acid aqueous solution (0.05 M HCl). The final sol was obtained by adding 7.7 cm^3 of the stock sol to the solution containing the block copolymer. The final solution was reacted for 24 hours under stirring and then it was aged at 28°C for 1 week.

Time-resolved in-situ IR analysis was performed at the synchrotron infrared beamline (SINBAD) at the Laboratori Nazionali di Frascati of the Istituto Nazionale di Fisica Nucleare (INFN) using a Bruker Equinox 55 and a conventional Globar source. The IR measurements were performed in the range of 500-6000 cm^{-1} with a resolution of 8 cm^{-1} in transmission configuration with a Bruker Hyperion 3000 microscope that was installed laterally with respect to the interferometer. A diamond disk was selected as substrate because of the excellent transmission in the 700-2000 cm^{-1} region [74]. A MCT detector (1 mm^2 size) cooled to the liquid nitrogen temperature and a KBr beam splitter were used. Before measuring each sample, a background spectrum of the diamond disk was recorded. Rapid scan time-resolved measurements were performed by a single scan per spectrum and an acquisition time of 133 ms followed by an interval of 160 ms before the beginning of the new measurement. A small drop of a controlled amount of the precursor sol (2-5 μL) was cast on the diamond disk, and immediately afterwards the measurement was started. The percent relative humidity (RH%) during the experiment was carefully monitored, and a special room was built around the microscope in order to control it. RH values were maintained lower than 40%.

The choice of the experimental conditions, to perform FTIR in situ experiments during the deposition of films from liquid phase, is particularly critical, because of the signal saturation and the process time scale. We have carefully selected the volume of the sol drop to be cast to get better reproducibility of the experiment and to avoid saturation of the signal. The intensities of the vibrational modes due to ethanol and water, especially at the first stage of the deposition process, are very intense and can easily saturate the detector. The selection of the sol drop volume is

therefore a critical issue, also because the evaporation rate is highly dependent on the sol volume; in smaller drops the evaporation is much faster. Several runs of the same experiments have been performed to test the reproducibility of the technique. Rapid scan time-resolved (RSTR) FTIR analysis allowed us to reach a good compromise in terms of signal-to-noise ratio and acquisition time rate. Application of time-resolved IR spectroscopy to a kinetic process, such as film deposition from a liquid phase, requires also a careful treatment and evaluation of the data. The film thickness, in fact, decreases with the time, as the evaporation of the solvent proceeds. This time-dependent change of film thickness induces a different light scattering from the sample and a shift of the baseline. Some "ghost" processes can appear, in this case, without a specific treatment of the single spectra recorded by RSTR infrared spectroscopy. We have extracted the spectra from the sequential 3D-RSTR file and introduced the baseline correction by a concave rubberband correction method (OPUS 5.5 software) using 64 baseline points and 20 iterations.

Another problem in performing FTIR in situ experiments during the deposition of films from liquid phase is the high overlapping of the vibrational modes of the different chemical species involved in the process. Understanding of the kinetics and the reactions needs separation of the different signals, in terms of resolution and intensity, which is very difficult to obtain. The formation of the silica walls, for instance, can be observed by the appearance of the Si-O-Si stretching modes (ν_{as}, 1070 cm^{-1}), which is, however, overlapped with signals from ethanol, TEOS, and the surfactant (see Figure 3.22). Three-dimensional spectra recorded by RSTR measurements give a possible alternative for visualizing the process in a simple and effective way. Of course, no direct information can be obtained about organization of the structure, and separate in situ experiments have to be performed by SAXS.

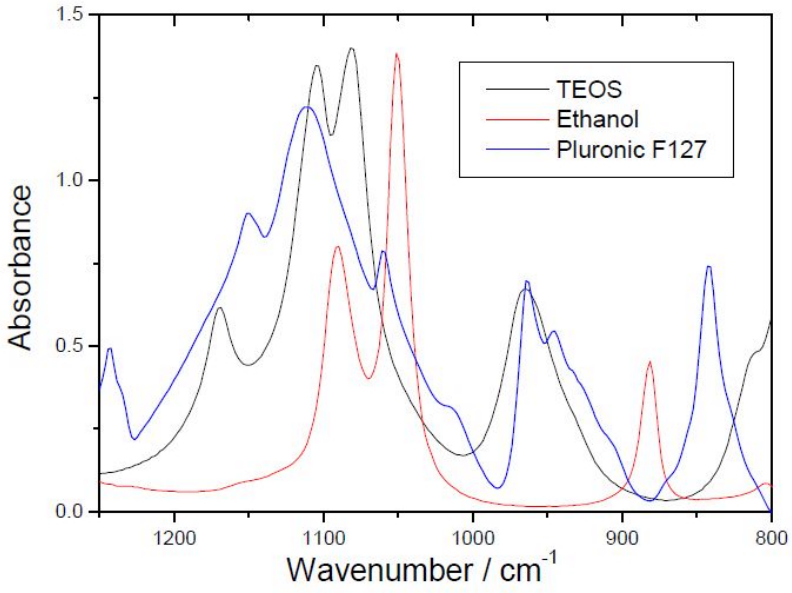

Figure 3.22: FTIR absorption spectra of liquid films of ethanol, TEOS and Pluronic F127.

The results of the RSTR measurements during casting of a silica film (with Pluronic F127 as templating agent) are shown in Figure 3.23. It is a 3D representation of the RSTR measurements, with the wavenumber and the time in the *x*- and *y*-axes, respectively, and the intensity changes in a colour scale. At the first stage of film formation, the solvent evaporation is the predominant process, and the ethanol signature (1044, 1095, and ~1400 cm^{-1}) saturates a great part of the other vibrational modes. The film is rich in water and ethanol, and the condensation process is not yet started. The end of this process is clearly recorded by RSTR; in fact, a discontinuity in the 3D spectra is observed after 38 s (dotted line in Figure 3.23). Interference fringes, due to the solvent evaporation, are observed in the first stage and disappear with completion of the process; throughout this stage the film shows a continuous decrease in thickness, as revealed by the increasing distance between the maxima of two adjacent interference fringes. There are basically two regions of interest, the 2700-3700 cm^{-1} region, with the OH stretching modes, and the 900-1700 cm^{-1} region, with the Si-OH band (around 950 cm^{-1}), the overlapped modes due to EtOH, Si-O-Si stretching, and Si-OR around 1100 cm^{-1}, and the bands due to ethanol and water around 1470 and at 1640 cm^{-1}, respectively [52].

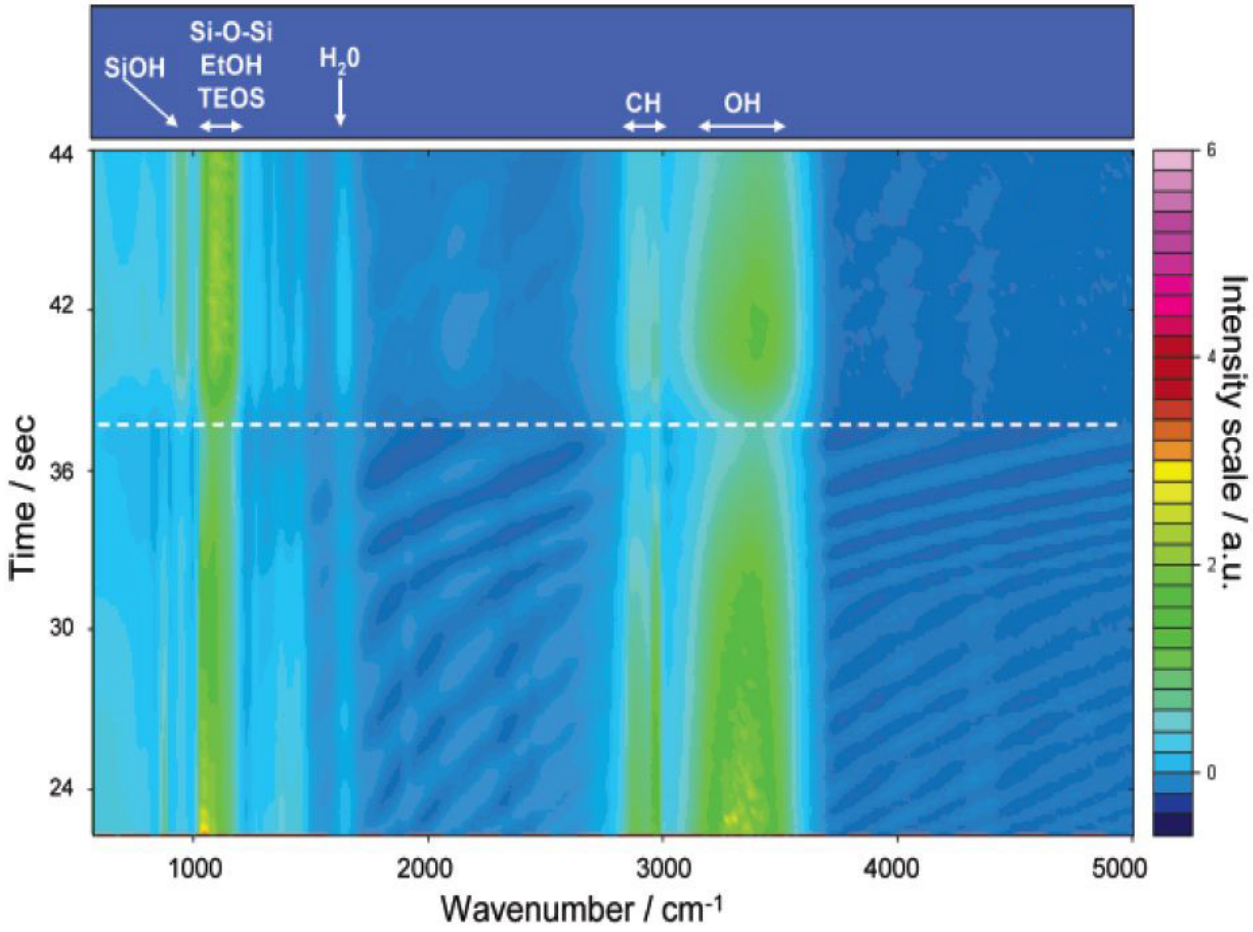

Figure 3.23: 3D-RSTR FTIR image obtained during the deposition by casting of a self-assembling silica film.

The second stage, which starts after an intermediate stage of few seconds, is characterized by the polycondensation reactions of silica. The increase in intensity of the band around 1100 cm^{-1} (ν_{as}, Si-O-Si) is an indication that the polycondensation reactions are forming a growing silica network. These reactions produce water that again enriches the film; an increase in the intensity of water vibrational bands (1640 and 3300 cm^{-1}) is observed together with the appearance of an intense Si-OH band. This last phenomenon seems contradictory, because condensation leads to the formation of siloxane bonds, Si-O-Si, at the cost of silanols, Si-OH. It can be, however, explained by the fact that even during condensation the hydrolysis can happen to a quite large extent. On the other hand, the formation of silanols can also be a source of water absorption from the external environment because the film also becomes more hydrophilic, increasing the water adsorption tendency. Together with the increase of the signal of water, after the beginning of polycondensation, an increase in intensity of the C-H stretching band (2700-2900 cm^{-1}) is observed. This is, however, produced by a not perfect correction of the time-dependent thickness effect, more than by a true chemical process associated with the film formation. While, in fact, in the 800-1400 cm^{-1} region baseline correction with thickness change is reliable because of the relatively sharp bands involved, in the 2700-3500 cm^{-1} interval this is more critical because of the presence of the very wide band due to O-H stretching that overlaps the C-H stretching region. It is also interesting to observe the different evolution with time of solvent evaporation and polycondensation. Evaporation appears as a slow, continuous process, while the abrupt increase in the signal intensity after the first stage shows that polycondensation is a much faster process.

We performed an other series of experiments in order to point out the effects of surfactant on kinetics of processes involved in EISA, so four different sols were prepared: (1) TEOS, H_2O, EtOH, HCl; (2) TEOS, H_2O, EtOH, HCl and Pluronic F127; (3) TEOS, MTES, H_2O, EtOH, HCl; (4) TEOS, MTES, H_2O, EtOH, HCl and Pluronic F127. Molar ratios were set as in the previous experiment, that is: TEOS : MTES : EtOH : H_2O : HCl : F127 = 1 : 0.56 : 24.48 : 14.70 : 0.11 : ($7.6x10^{-3}$). All the acquisition parameters and configuration were kept the same too, except the time interval between two spectra acquisition, which was set at 3 s. The in situ IR spectra measured during EISA are shown in Figure 3.24 (TEOS-MTES systems) and in Figure 3.25 (TEOS systems).

We have used the 1640 cm^{-1} vibrational mode to follow the change in water content in the films (insets in Figures 3.24 and 3.25). The results show that the trend is similar for all the systems and is related to sol-gel chemistry of film formation. An initial rapid evaporation is followed by a small increase in water content, in correspondence with silica polycondensation reactions, and a second evaporation stage. These results are not obvious as few authors, to explain EISA, were taking into account the real evolution of water content as a function of time. However, as we show here, the

water evaporation can be modelled using three different phases: (a) Fast Initial Evaporation (FIE); (b) Water Enrichment (WE) due to silica polycondensation and (c) Second Evaporation Stage (SES). After SES, however, not all the water is evaporated from the as deposited films, as clearly observed by the infrared spectra (not shown in the Figures). It is important to observe that, even if the trends in the four systems are the same, the evaporation times are different: the FIE phase slowed with presence of the surfactant.

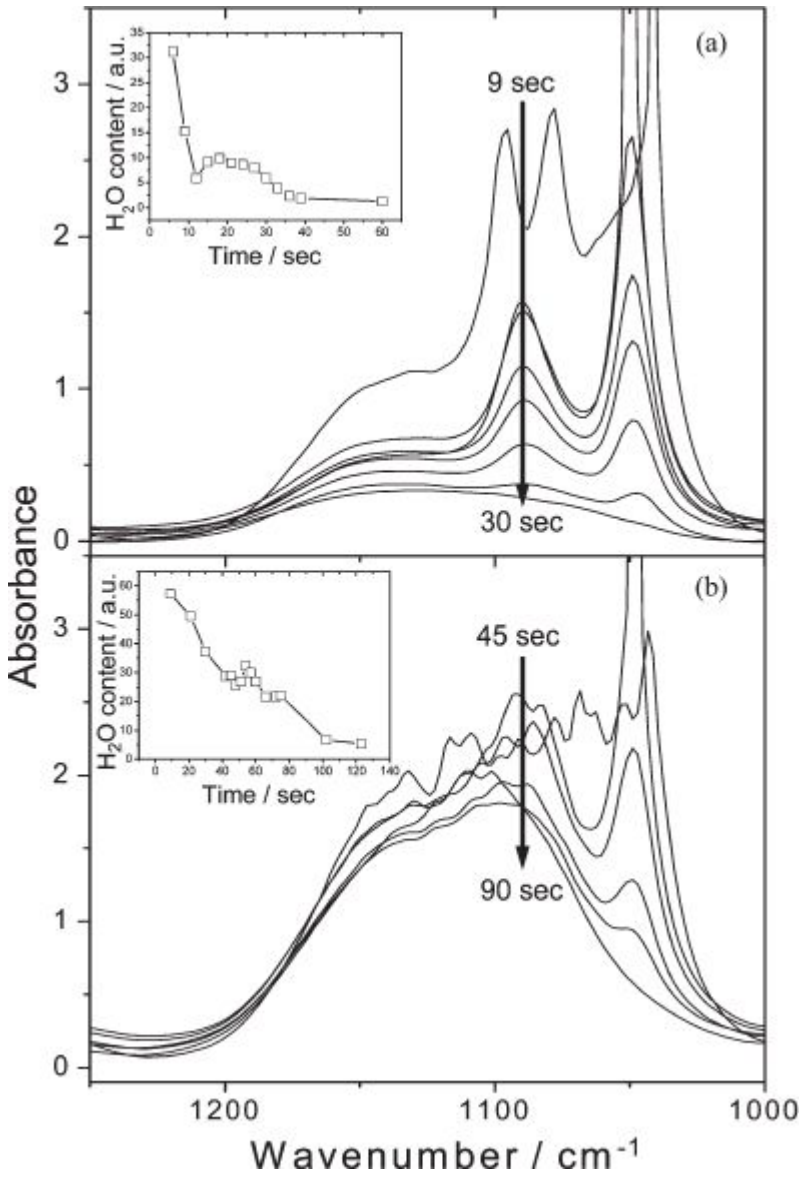

Figure 3.24: Infrared absorption spectra recorded at different times after film deposition for (a) TEOS–MTES and (b) TEOS–MTES–F127 systems. The variation of water content in the films, measured by the change in absorption area of the 1640 cm^{-1} band, is shown in the Figure insets.

The kinetics of silica polycondensation has been followed observing the IR transmission in the 1000–1250 cm^{-1} range. The first spectra are dominated by the strong signature of ethanol vibrational modes (1044 and 1095 cm^{-1}). The rapid evaporation of alcohol creates a water-rich film

and pushes the polycondensation reactions to form the silica network. The condensation rate of silica can be estimated using the Si–OC_2H_5 vibrations in TEOS and MTES as references. The unreacted alkoxides give rise to absorption bands at 1096 cm^{-1} (ν_{as} (C–O)) and 1048 cm^{-1} (ν_s (C–O)). To calculate the differences in the kinetics, we have assumed as a reference the moment when the 1048 cm^{-1} band is no longer detected. At this point only the main ν_{as} (Si–O–Si) vibrational mode around 1100 cm^{-1} due to silica is observed.

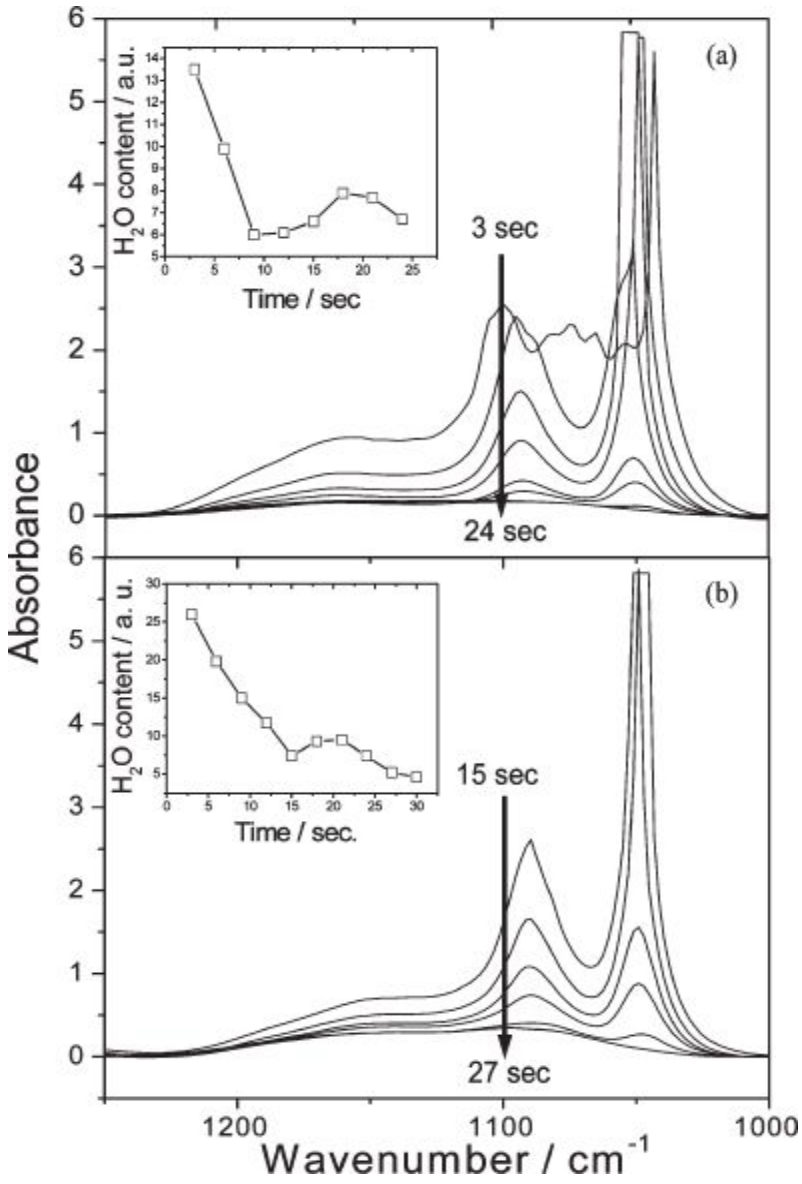

Figure 3.25: Infrared absorption spectra recorded at different times after film deposition for (a) TEOS and (b) TEOS–F127 systems. The variation of water content in the films, measured by the change in absorption area of the 1640 cm^{-1} band, is shown in the Figure insets.

The IR results show, therefore, that there is a significant trend also in the case of silicon alkoxides reaction kinetics. The presence of the surfactant slows down the silica polycondensation and this effect is crucial in the MTES–TEOS–F127 system. On the basis of these results, we can explain the

much increased tendency to form highly organized mesostructures during EISA. A slower rate of polycondensation gives, in fact, more time for the micelles to organize before a rigid network is formed and/or phase separation is observed. A comparison between the different kinetics of ethanol and water evaporation during EISA can be obtained from FTIR spectra using a 2D correlation analysis. Figure 3.26 shows the asynchronous spectra obtained correlating in 2D the absorption spectra of MTES–TEOS–F127. The two symmetric cross peaks out of diagonal are respectively negative (shaded area) and positive showing the time correlation between ethanol and water. The presence of a positive cross peak of ethanol around 1400 cm^{-1}, which is large because of the several overlapped bands due to ethanol in this interval, means that the intensity change of ethanol occurs predominantly before that of water at 1640 cm^{-1}.

These experiments show that the evolution of silica condensation, which is within a few tens of seconds, is not negligible to explain EISA, as supposed by other authors [75,76]. The silica polycondensation rate is, instead, a basic parameter to be taken into account during EISA: the IR measurements show, in fact, that longer polycondensation kinetics, even in this short time scale, give a better and easier organized mesostructure (see sections 3.1 and 3.2).

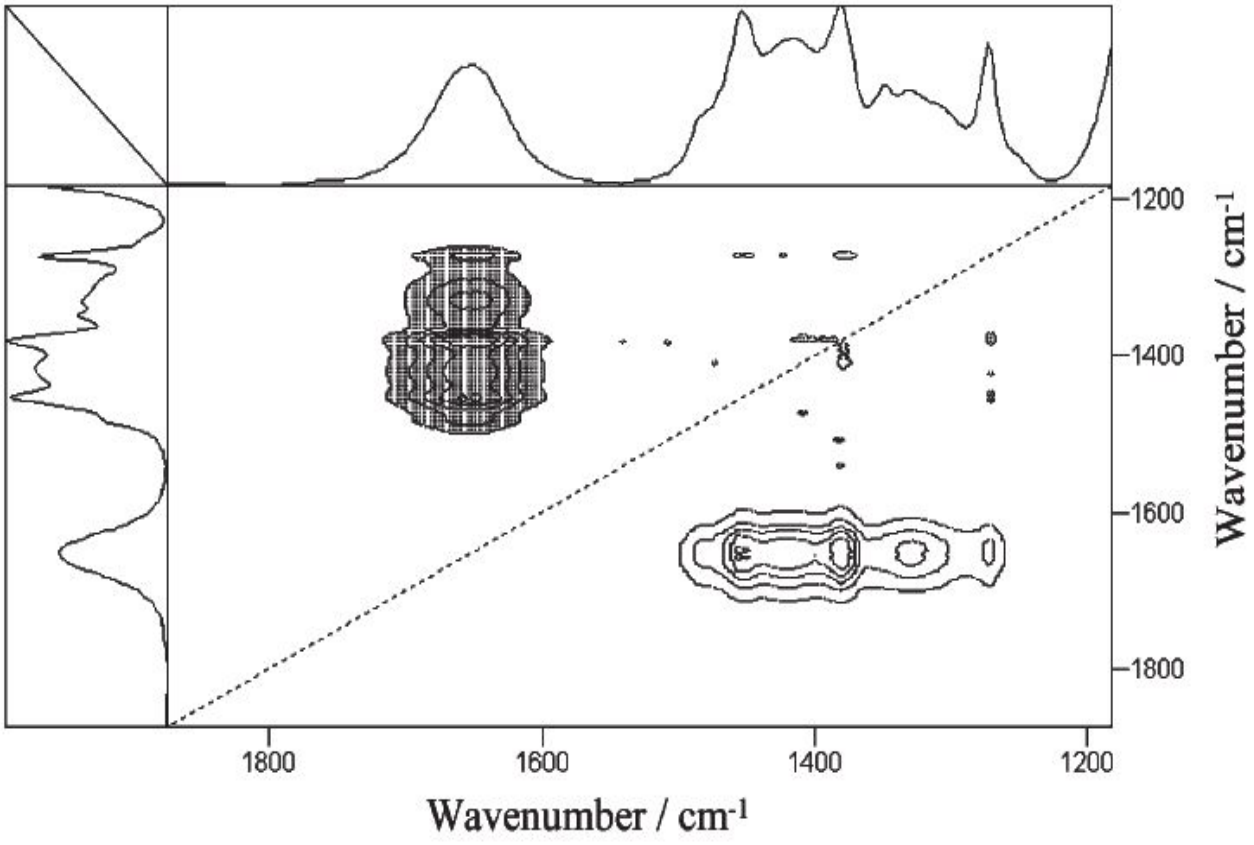

Figure 3.26: Asynchronous 2D IR correlation spectrum of MTES–TEOS–F127.

3.5 Simultaneous, in-situ and time-resolved analysis during self-assembly of mesoporous silica films by FTIR spectroscopy and SAXS

Several new techniques have been developed with the purpose of studying the phenomena occurring during self-assembly. The most popular among these techniques is in-situ SAXS using synchrotron radiation, which is used to assess structural changes and rearrangements in the mesostructure. However, this technique yields only structural information such as presence of an ordered mesostructure and degree of order, but it does not allow collecting time-resolved data about the chemistry of the process. Spectroscopic information can be obtained only ex-situ in as-prepared films, but in this case the chemical information regarding the phenomena occurring during the dip-coating stage is lost. The self-assembly of the inorganic units is guided by the self-assembly of the amphiphilic block copolymer; this process is triggered by the fast solvent (water, ethanol) evaporation, which also pushes the inorganic oligomers close together and favours polycondensation. Therefore, the lack of a spectroscopic in situ technique appears to be a weak point in the understanding of the process that leads to the formation of a mesostructure.

Several groups have successfully coupled SAXS with other in-situ techniques to correlate the structural data and the chemical processes that occur during dip-coating. An interesting example is reported by Grosso and co-workers who performed time-resolved in situ GISAXS using synchrotron light combined with interferometry measurements on a mesostructured silica film templated by cetyltriethylammonium bromide (CTAB) [31]. This combined interferometry-SAXS technique allowed correlating mesophase organisation occurring during dip-coating with film thickness. Here, the evolution of thickness with time follows a triple regime, where a first rapid evaporation step is attributed to the evaporation of (mainly) ethanol; the second step is slower, due essentially to the departure of water, and a third regime involves the loss of residual water and ethanol molecules. However, the departure of solvent molecules is just an educated guess which is not supported by experimental data. Another example of combined techniques was reported by Doshi et al. who performed time-resolved in-situ GISAXS using synchrotron light combined with gravimetric analysis to study the self-assembly of a slowly evaporating cast film [76]. In another work, in situ Karl Fischer titration measurements were used to estimate the content of water in as-deposited silica films as a function of RH, obtaining increasing h=[H_2O]/[Si] values with increasing RH values, even though titrations were not made on films but on solutions, which were assumed to be representative of the corresponding films [75]. Mass spectrometry of vapour fraction, Karl Fischer titration, ellipsometry and interferometry data acquired in-situ on mesostructured titania thick films were used to follow the evolution of volatile species and film composition [48].

Crossing these data led to the comprehension of the role of each variable involved in the self-organisation. Thanks to these central works, fundamental solution and processing parameters, such as the manifold role of water and the importance of the tuneable steady state, could be sorted out.

In the previous sections we have described the RSTR FTIR technique developed to study in-situ the first stages of self-assembly in cast films. It is very effective to monitor the evaporation of water and ethanol and the polycondensation reactions in silica mesostructured materials, and it can be extended to the in-situ analysis of mesostructured films during dip-coating, provided that the infrared spectrometer is coupled with the dip-coater. In order to obtain structural and chemical information on the physicochemical processes occurring during dip-coating, we decided to couple the FTIR and the SAXS techniques. In this section we show the results of a preliminary experiment conducted at the Austrian SAXS beamline of the ELETTRA synchrotron, in which simultaneous in-situ FTIR and GISAXS experiments were conducted in order to study and correlate the structural and the chemical processes occurring during dip-coating of mesostructured silica films. The purpose of this section is to illustrate the potential of this technique in the study of mesostructured films, therefore we have selected as an example an experiment conducted on mesostructured organosilica films obtained from MTES-TEOS solutions.

3.5.1 Experimental setup

The experimental setup is shown in Figure 3.27. FTIR measurements were performed using a Bruker IRCube™ interferometer. This is a very compact commercial interferometer working in the mid-IR range with a Ge/KBr beam-splitter and a Globar source. The setup was designed so that simultaneous FTIR and GISAXS measurements could be performed on the film, using the conventional Globar source and the synchrotron radiation, respectively. The optical components of the FTIR spectrometer were set up in a way that a parallel IR beam was focused by an additional external parabolic mirror onto the sample in transmission mode at normal incidence. The transmitted signal was reflected by a flat mirror towards an elliptical mirror focusing the signal onto the liquid nitrogen-cooled MCT detector.

A GISAXS configuration requires that the correct angle of incidence be set carefully: the optimum angle of incidence must be slightly above the critical angle of a mesostructured film (~0.2°), and small variation off this optimum angle can deeply affect the GISAXS measurements, because a too small angle can cause total reflection, whereas a too large angle can cause insufficient scattering. The dip-coater sample holder can be rotated so that the angle of incidence of the impinging X-ray can be readily varied. However, because accessing the experimental hutch during the experiment is forbidden, the sample holder rotation must be performed before the experiment is started.

Therefore, we used a freshly-coated mesostructured silica sample for the adjustment of angle of incidence, which was then left unaltered during the whole experiment by fixing the sample holder.

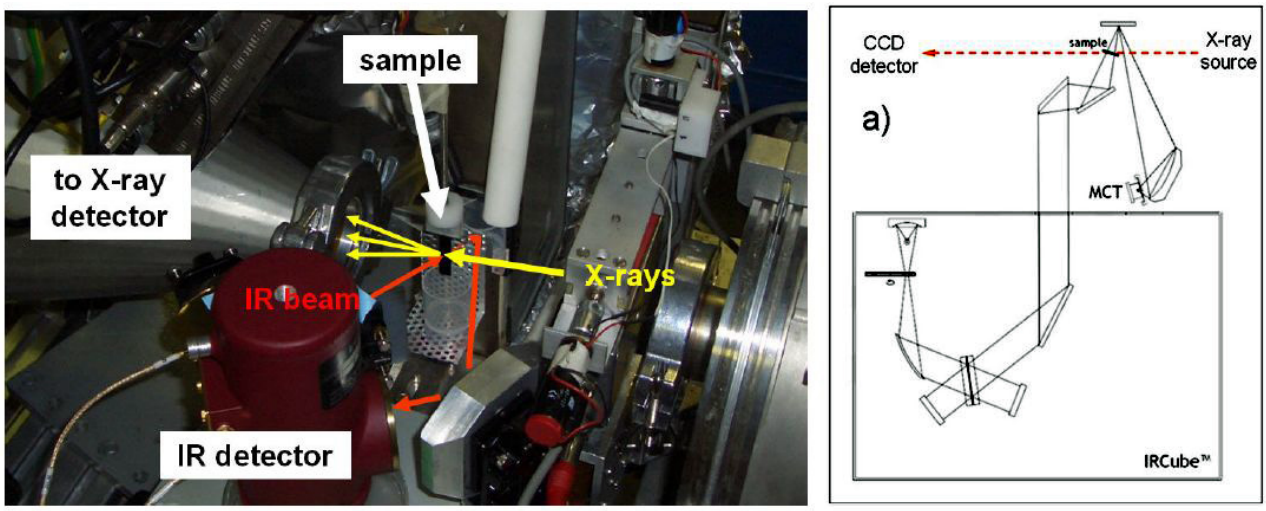

Figure 3.27: (left) Photograph of the experimental simultaneous FTIR-SAXS apparatus at the Austrian SAXS beamline at the ELETTRA synchrotron. (right) Scheme of the experimental setup used for the experiments.

In this experimental configuration, the incident IR and X-ray beams probe the very same region of the sample (see Figure 3.28). The interval between successive acquisitions was set to 2 s, since from preliminary tests we evaluated that the time scale of these processes is on the order of seconds both in terms of self-assembly and chemical processes. The sequence of GISAXS and FTIR spectra acquisitions was simultaneously launched immediately after the solution vessel was lowered. FTIR data were collected using the Bruker OPUS™ software, and each FTIR spectrum was obtained by averaging 16 interferograms collected at a resolution of 8 cm^{-1}. Background was collected prior to each measurement session as the average of 100 spectra on a bare silicon substrate, previously cleaned with water, EtOH and rinsed with acetone.

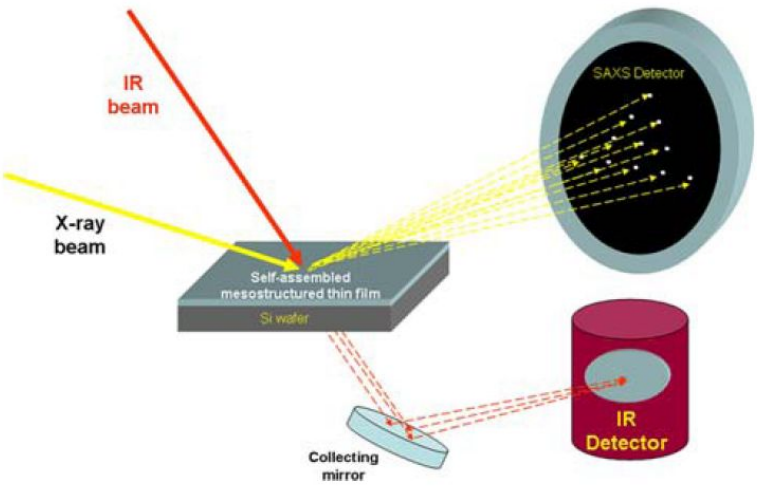

Figure 3.28: Schematic drawing of the FTIR-GISAXS experimental configuration showing that the incident IR and X-ray beams probe the very same region of the sample.

Here we present an in situ SAXS-FTIR experiment using the hybrid silica precursor solution described in section 3.2. These hybrid systems are synthesised from a precursor solution where the Si source is a mixture of TEOS and MTES, and the templating agent is block copolymer Pluronic F127. The precursor solution was prepared as described previously: a solution containing 3.08 ml EtOH, 2.84 ml TEOS, 1.42 ml MTES and 0.355 ml HCl 0.768 M was stirred for 45 minutes, then added to a solution containing 15 ml EtOH, 1.3 ml HCl 0.057 M and 1.3 g F127. The final solution was stirred for 10 minutes and used for dip-coating. The substrate was a 400 μm-thick, p-type B-doped (100) Si wafer. This substrate was chosen because it ensures transparency in the mid-IR range. Simultaneous FTIR and SAXS acquisitions were launched after lowering the solution vessel (withdrawal speed 2.3 mm/s), as soon as the silicon substrate was fully coated. The relative humidity in the deposition chamber was set to ~10% and kept throughout the whole experiment.

3.5.2 GISAXS results

Figure 3.29 shows the time-resolved GISAXS two-dimensional patterns recorded at intervals of 2 s. The first significant snapshots are shown, from t = 0 (acquisition start) to t = 20 s. Another GISAXS snapshot, recorded at t = 20 min, is also reported. The GISAXS and FTIR spectra were recorded for times as long as 40 minutes from dip-coating. The GISAXS patterns show that in the first 8 s no organisation of the mesophase takes place, and after 10 s the presence of a ring (dotted line in the figure) indicates that organisation is starting, even though a mesophase is still not well defined. At 12 s the detection of well-defined spots reveals the presence of an ordered mesostructure. Whereas these spots increase in sharpness and intensity with time, negligible changes are observed at times longer than 20 s. These in-situ GISAXS data show only two diffraction spots, which makes the unambiguous identification of the space group impossible. This is because the integration time for each GISAXS pattern was limited to 500 ms in order to have good time resolution, and higher-order diffraction spots requiring longer integration times could not be recorded. Nevertheless, these spots could be used to quantify the degree of order of the mesophase.

3.5.3 FTIR results

Figure 3.30 shows the FTIR spectra recorded simultaneously with the GISAXS patterns shown in Figure 3.29. What was expected to be detected in this experiment was the kinetics of solvent and water evaporation. The raw spectra shown in Figure 3.30 appear well resolved and exhibit good signal-to-noise ratio even if they have not been smoothed and the baseline was not corrected. We can recognise two main regions, at high wavenumbers (3700–2800 cm^{-1}) and at low wavenumbers (1700–800 cm^{-1}) where different chemical species overlap. In the first stages the FTIR spectra are

dominated by the vibrational modes attributed to ethanol. Its intense signals at 2973, 2927, 2885 cm^{-1}, at 1460–1270 cm^{-1}, at 1088 and 1050 cm^{-1}, and at 880 cm^{-1} allow following solvent evaporation with time. After about 8 s this process is completed (the residual signal after 10 s observed in the C-H stretching region around 2700–3000 cm^{-1} was assigned to the surfactant). The decrease in intensity of the 1640 cm^{-1} vibrational mode attributed to water ($\nu_b(H_2O)$) indicates that evaporation of water is also observed in the first seconds of dip-coating, but after this fast initial stage, a slower evaporation rate follows.

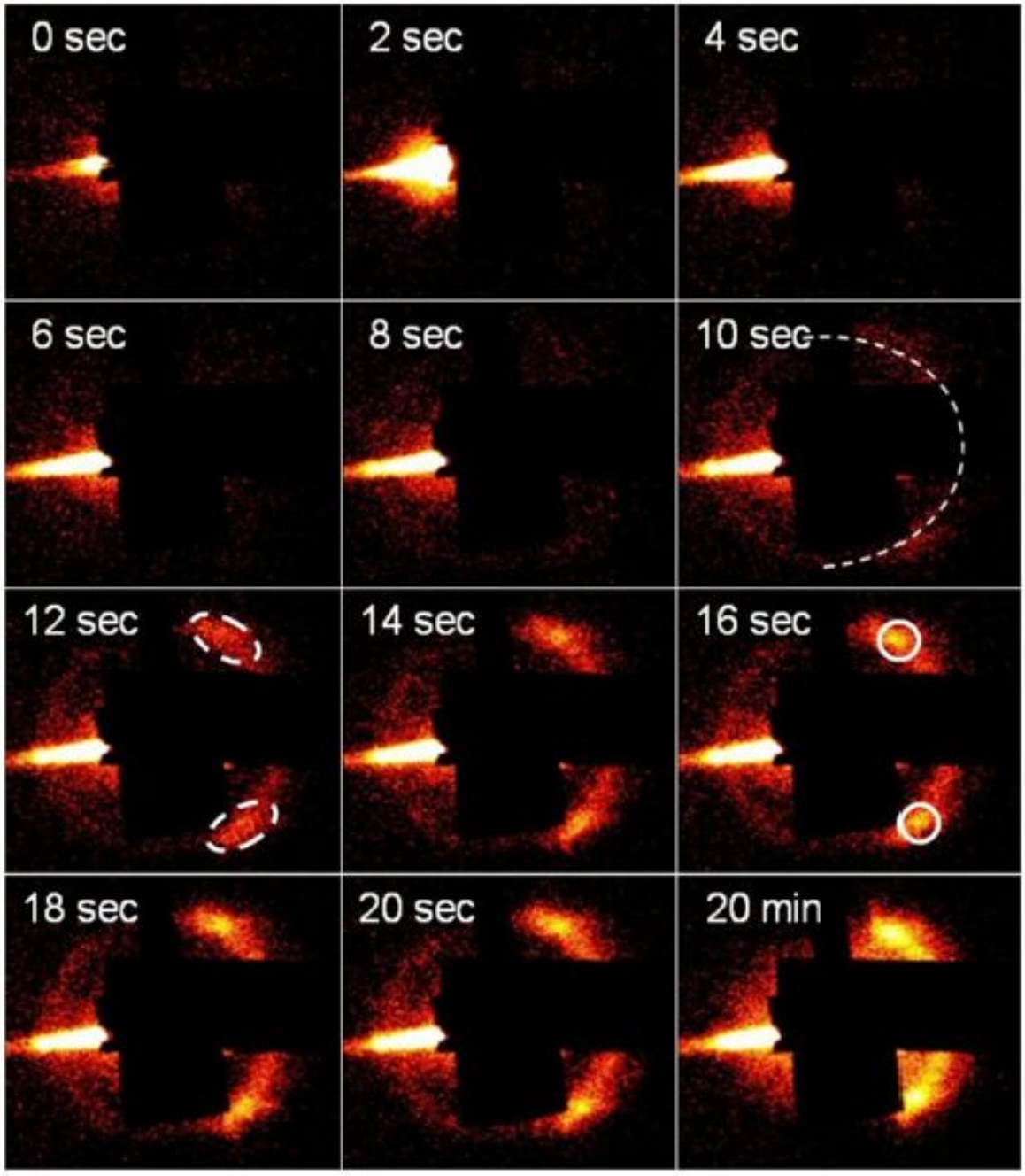

Figure 3.29: GISAXS images recorded at different times after the dip-coating.

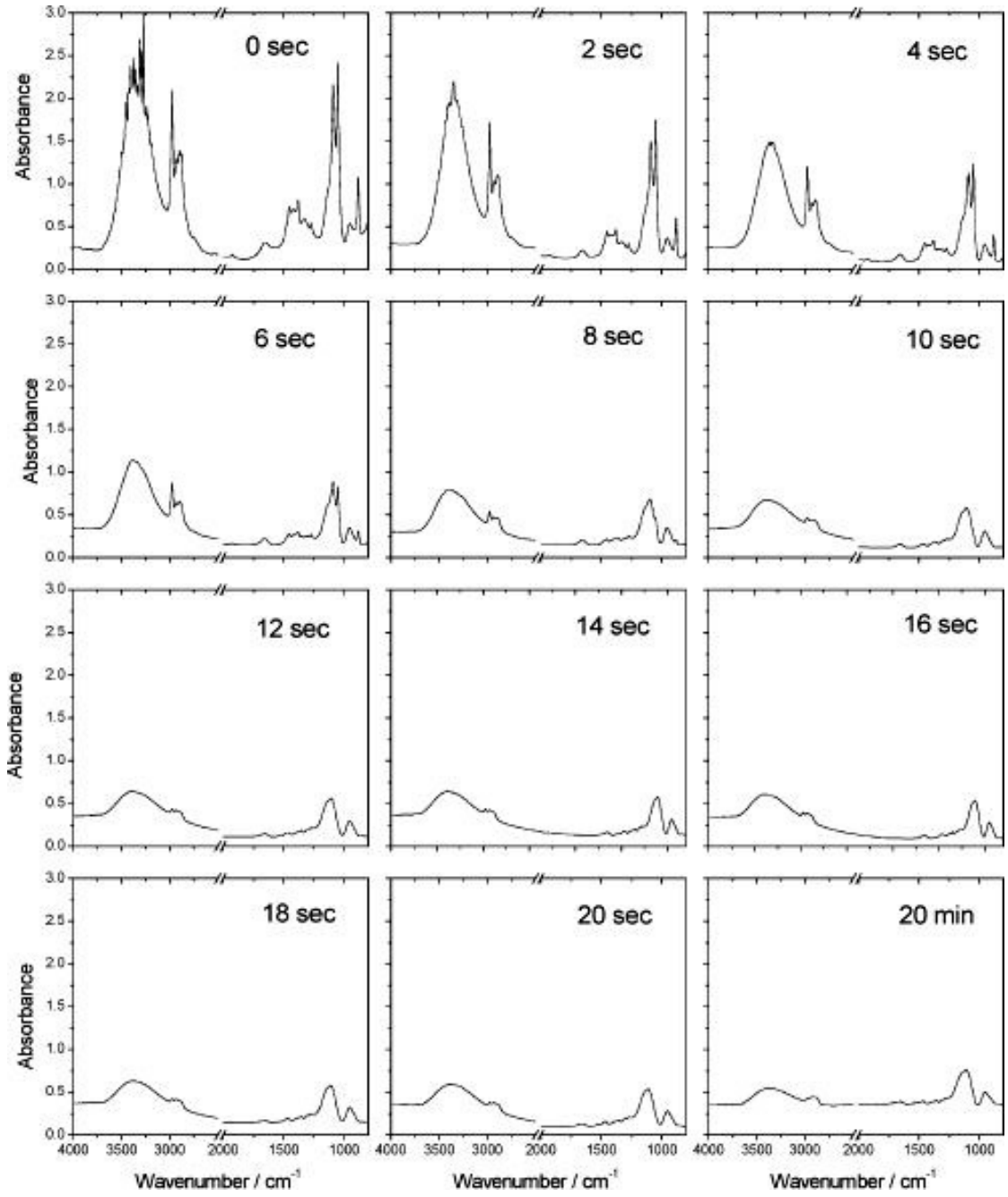

Figure 3.30: FTIR absorption spectra recorded at different times after the dip-coating.

3.5.4 Comparison between GISAXS and FTIR data

Figure 3.31 shows the content of ethanol and water in the film as a function of time (dip-coating was set as t = 0). The content of ethanol and water was estimated considering the areas subtended by two specific absorption bands that are well resolved and not overlapped with other vibrational modes, that is around 880 and 1640 cm^{-1} for ethanol and water, respectively. The area of the two bands was plotted as a function of time, assuming that the areas at t = 0 correspond to 100% water and 100% ethanol in the film. From this graph, the evaporation of ethanol appears fast, following a linear trend: after 10 seconds the residual ethanol in the film can be approximated to 0%, so that the

process can be considered to be complete. The evaporation of water has a more complex trend: (1) a fast initial evaporation in the first 2–3 seconds, similar to ethanol, is followed by (2) a slower intermediate stage between 3 and 6 seconds, (3) then a third phase of water enrichment between 6 and 10 seconds is followed by (4) another evaporation stage from 16 seconds onwards. More specifically, at t = 10 s, around 30% of the initial water is present in the film, whereas all ethanol is evaporated. At t = 20 s, around 20% of the initial water is still detected in the film. The water enrichment stage (third point in the above description) is attributed to the polycondensation reactions that occur after ethanol evaporation. This result is in good agreement with our findings in time-resolved experiments with self-assembling cast films reported in the previous section. Even if the different solution volumes that are involved during dip-coating or casting of films produce different evaporation kinetics, it appears that this behaviour is reproducible during film deposition from liquid phases when sol-gel reactions are involved.

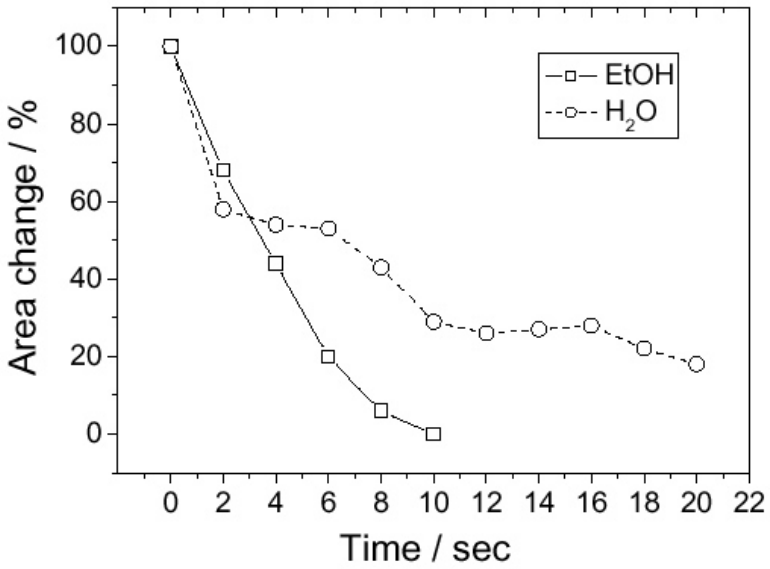

Figure 3.31: Change in the area of the 1640 cm^{-1} band attributed to water and of the 880 cm^{-1} band attributed to ethanol as a function of time after dip-coating.

From SAXS data, we observe that the organisation into an ordered mesophase starts only after ~10 seconds. Comparing these structural data with the chemical data from FTIR measurements, we infer that an ordered mesostructure is formed after ethanol evaporation is completed and 70% water has departed from the film: at this stage the SAXS diffraction spot intensity increases showing a sigmoidal trend with time. Figure 3.32 shows the change in the average intensity of a SAXS diffraction spot (upper spot in the snapshots of Figure 3.29) as a function of time. To obtain these data, the intensity of a selected diffraction spot in a SAXS pattern was calculated as the average intensity calculated in a rectangular area around the spot, composed of 1148 pixels. These data were used for a semi-quantitative evaluation, in that they could not be normalised with respect to the

intensity of the background. Nevertheless, this gave a reliable indication on how the mesophase evolves with time.

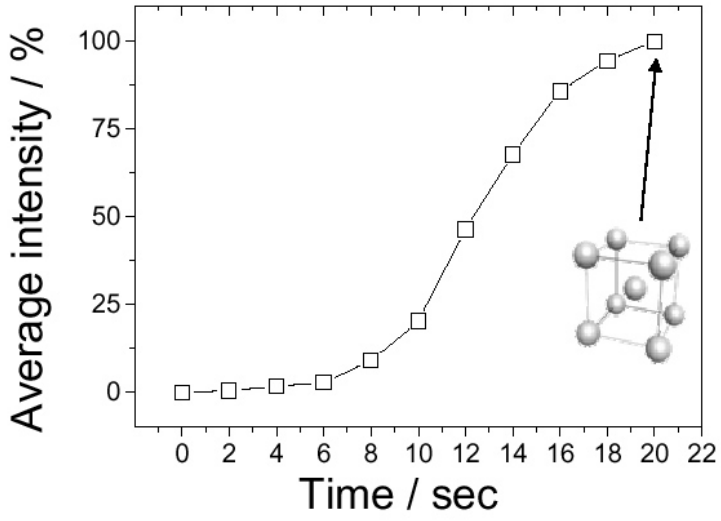

Figure 3.32: Average intensity of a GISAXS diffraction spot as a function of time.

It is not straightforward to follow polycondensation reactions by the FTIR technique because of the overlapping of the ethanol signals in the 1000-1200 cm^{-1} range with the silica antisymmetric stretching ν_{as}(Si-O-Si) band at around 1100 cm^{-1}. We have therefore chosen the Si-OH stretching band at 950 cm^{-1} to study how the condensation reactions are affected by water and ethanol evaporation. Even if this band is overlapped with the sharp 882 cm^{-1} ethanol band (after 10 seconds this band disappears in accordance with the data of Figure 3.31), then we have deconvoluted the spectra to separate the contributions of the two different components. Figure 3.33 shows the change of the Si-OH band as a function of time. In the first 6 seconds, a fast decrease of the band area is observed, and after this time the area of the band shows only a very weak decrease (~3%). These data indicate that after 6-8 seconds the polycondensation reactions are almost finished, even if clearly not all of the silanols reacted. However, at this stage the silica network is still flexible enough to allow spatial reorganisation of micelles. According to our data, it is reasonable to assume that critical micelle concentration (*cmc*) is reached only after the first water evaporation stage (steps (1) and (2) cited above) and ethanol evaporation: to our knowledge, no experimental evidence of micelle formation at an earlier stage is reported in the literature at the moment. Therefore, this is the first time that evidence is provided regarding the time correlation between solvent evaporation and mesophase formation. This is the most exciting finding of this FTIR-SAXS in-situ technique. An attempt to determine the *cmc* in the films during dip-coating has been reported by Doshi et al. [76] They assumed that the *thickness* x *micelle concentration* product is the same in the drying profile. This assumption, however, does not take into account the change in surfactant concentration

induced by surfactant migration during drying (the so-called coffee stain effect, discussed in the next chapter). The data show unambiguously that organization starts only after solvent evaporation, which represents the critical step in self-assembly. After this stage, the micelles are formed even if we can only observe their organization at a later moment.

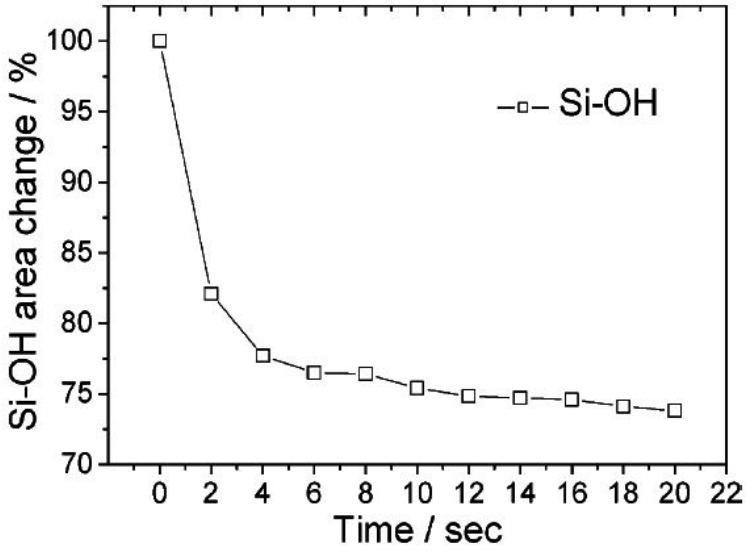

Figure 3.33: Change in the area of the infrared band at 950 cm^{-1} (Si-OH) as a function of time after dip-coating.

The major advantage of this simultaneous FTIR and SAXS analysis is the possibility to discriminate between the evaporation rates of ethanol (or any other solvent) and water, as well as to obtain semi-quantitative data that can be examined in the light of the structural data provided by SAXS. The discrimination between different chemical species can be readily attained by FTIR spectra, as vibration modes are attributed to different chemical species (e.g. the amount of free water, the degree of condensation of the inorganic walls). In this experiment, it has been proved that the formation of an organised mesophase occurs after all ethanol and 70% of water have evaporated. At this stage, the presence of water in the film can be estimated as $h = [H_2O]/[Si] = 1.56$ (i.e. 30% of h in the precursor solution), which is close to the values obtained through other in-situ experimental techniques such as Karl-Fischer titration. This leads us to identify another application of the present technique, in that the water content (expressed as h) can be simply calculated from FTIR data and correlated quantitatively with RH. As we have said, this has been done previously by means of rough estimates from Karl-Fischer titrations on cast films rather on dip-coated films, but the FTIR-SAXS technique can be considered to be more accurate. Other advantages of this FTIR-SAXS combined technique are that it is not invasive, it can be applied to thin films instead of thick films, cast drops or solutions, and it does not require altering the chemistry of the self-assembling system. It also takes into account the presence of atmospheric water, as a reference background is taken prior to each FTIR measurement session. This is important because a direct correlation can be

established between the RH value in the deposition chamber and the quantity of water present in the film: this correlation was previously studied in the literature, but using experimental techniques based on thick films or cast films, whose behaviour is quite different from thin films obtained by dip-coating and studied by in-situ SAXS. Recently, we have reproduced the same triple regime in the FTIR in-situ study on a ethanol or water-ethanol evaporating cast droplet, the results are shown in the next chapter. In this work, multiple evaporation steps were associated to water adsorption from the atmosphere, and water and ethanol evaporation from the droplet.

More in general, the simultaneous recording of different types of information allows correlating different phenomena that contribute to a complex process such as self-assembly in mesostructured films. This is particularly relevant when the kinetics of some chemical processes can affect other chemical or physical processes involved in the phenomenon. Another main advantage provided by the in-situ FTIR-SAXS technique is that different vibrational modes can be attributed to different species in the FTIR spectra (provided that they do not overlap). Therefore, different chemical information can be obtained, for example on water content, ethanol content, inorganic condensation, copolymer content, etc. This experiment also opens many important perspectives in other research areas, for example the real-time and in-situ detection of the radiation damage induced in biological systems and tissues.

CHAPTER 4

From the basics of sol-gel and EISA to applications of mesoporous silica films

Fabrication of films from liquid phase and self-organization processes of nanomaterials, such as EISA, are strongly dependent on evaporation phenomena. Sol-gel processing of thin films is a typical example and controlling the external conditions in the deposition environment is very important, because the relative humidity strongly affects the overall process, so the knowledge of the physics and the chemistry behind the evaporation of solvents, especially of ethanol and water which are the most commonly used, is very important for the development of several technologies. In this chapter are presented our studies performed by rapid-scan time-resolved FTIR spectroscopy on the evaporation process of ethanol, ethanol-water mixtures, water and deuterated water. Moreover, by time resolved FTIR imaging, we have studied the coffee-stain effect, as it has been observed for a large variety of solvent-solute systems and it was shown that controlled stain effects can be used to pattern solid surfaces by a self-assembly mechanism and several applications in nanotechnology have been envisaged. Finally, is presented an application of mesoporous silica films: they were patterned by means of deep X-ray lithography using synchrotron radiation, obtaining mesoporous objects with controlled size and shape, then an atomic force microscope enabled selective functionalisation of the objects with rhodamine 6G. This experiment allows envisioning new fabrication technologies of functional materials for applications such as DNA nano-spotting or lab-on-a-chip devices.

4.1 Study of the evaporation of ethanol and ethanol-water mixtures by time-resolved FTIR spectroscopy

Deposition of thin films from the liquid phase is a widely used technology for fabrication of coating layers of oxides, organic polymers and hybrid organic-inorganic materials. Sol-gel processing is a typical example of technology for film deposition by liquid phase and several products are now on the market, such as antireflective and antiscratch coatings [77,78]. As we have shown in the previous chapters of this doctorate thesis, sol-gel is also at the basis of EISA processing of

mesoporous thin films: in such a case the role of solvent is critical because it is only during the evaporation phase that the critical micelle concentration is reached and self-organization of the template occurs. From sol-gel to EISA processing, the evaporation of the solvent plays a crucial role, therefore a deep knowledge of this very basic phenomenon is fundamental for a real understanding and control of film deposition via the liquid phase.

In sol-gel and EISA deposition techniques, ethanol is the most widely used solvent, which is often preferred to methanol due to its lower toxicity and due to lower vapour pressure with respect to other alcohols. In previous studies, multi-step evaporation rates, attributed to water uptaking, have already been observed by interferometry for sol-gel film deposition [79,31]. Controlling water and ethanol evaporation is, therefore, necessary during thin film deposition. However, even nowadays, there is a lack on available data about simple yet extremely important features of the physics and the chemistry behind such basic phenomena. Studies on evaporation of ethanol, water and binary water-ethanol mixtures have been already performed on different surfaces by studying the changes in the contact angle [80,81].

The evaporation of an ethanol-water aerosol droplet has been also followed by cavity enhanced Raman scattering and laser induced fluorescence [82], whereas fluorescence spectroscopy has been used to probe the evolving size of evaporating droplets [83]. Experiments on droplet evaporation on solid surfaces have shown that two pure modes of evaporation can be identified [84]: one consists in the decrease of the drop-substrate contact area maintaining the contact angle constant, and the second mode results in the decrease of the contact angle keeping the surface area constant. Phenomenologically, the evaporation process can follow either a pure mode or a mixed type, where the mode changes in the course of evaporation [84,85]. Details on the solvent evaporation process appear, however, still to be fully disclosed [86].

In the previous chapter, we have described how we applied time-resolved infrared techniques, to investigate the chemical reactions and the evaporation rates of the different components during self-assembly of mesoporous thin films. In particular, we have observed that in-situ rapid-scan infrared spectroscopy is very suitable for monitoring solvent and water evaporation during film deposition. Because of the complexity of the system, however, not all the details of the process could be fully explained. We have, therefore, recognized the need for a very basic comprehension of the evaporation processes related to ethanol at ambient conditions; we applied rapid-scan infrared spectroscopy to investigate the evaporation of ethanol droplets cast on an infrared transparent substrate and 2D correlation has been used to analyze the data.

4.1.1 Experimental setup and procedure

Ethanol (EtOH) anhydrous (RPE) for analysis, water content <0.1%, and double-distilled water were used for the evaporation experiments; ethanol was purchased from Carlo Erba Reagents and used without further purification. Time-resolved in situ IR analysis was performed at the SINBAD synchrotron infrared beamline (INFN, Frascati) using the IR microscope Bruker Hyperion 3000, with a conventional Globar source, a MCT detector and a KBr beam splitter at a resolution of 8 cm^{-1}. The experiments were conducted in transmission configuration, using a double-sided, forward-backward acquisition mode.

In a typical experiment, first the background spectrum of a ZnSe substrate was recorded as the average of 40 scans in air, then a small drop of ethanol or water-ethanol mixture (50 μl) was cast on the substrate and the measurement was started immediately afterwards. Rapid scan time-resolved measurements were performed by a single scan per spectrum and an acquisition time of 133 ms followed by an interval of 160 ms before the beginning of the next acquisition. We have recorded the infrared spectra of the evaporating droplet in the shortest time sequence that could be achieved; the scan time used in the experiment is the best compromise in terms of signal-to-noise ratio and resolution.

We have optimized also the ethanol droplet size; if the ethanol drop is too large, the infrared signal will be saturated for most of the measurement time, on the other hand, smaller droplets show a very fast evaporation and are not suitable for time-resolved studies. The experimental conditions that we have selected are optimized for an evaluation of the physical changes of the system but do not allow us to extract quantitative data, for example, about the evaporation rate. The main reason is the high ethanol-substrate wettability; due to the low contact angle (θ = 30°), the ethanol droplet quickly spreads on the substrate and only a part of the droplet can be illuminated by the IR beam. We have repeated the experiment for several runs (up to ten for each composition) to ensure reproducibility of the experimental conditions, and the experimental trend has been always the same; on the contrary, the time scale has been more difficult to reproduce due to the reasons we have previously pointed out. The relative humidity (RH%) during the experiment was carefully monitored, and a cabinet was built around the microscope to control the RH, which was kept constant at 50%. The measurements were done at 25°C and at room pressure. The results were analyzed by Bruker Opus 6.5 software. Baseline was calculated by rubberband correction using 64 points in a range from 1840 to 1600 cm^{-1} for the bands at 1740 and 1640 cm^{-1}, and in a range from 950 to 750 cm^{-1} for the band at 880 cm^{-1}.

4.1.2 Experimental results and data analysis

To monitor the evaporation process of ethanol and ethanol-water binary mixtures, we have selected specific bands attributed to the two components. This choice was dictated by the need to have a vibrational mode that is not saturated during the measurement and not overlapped to other bands. In particular, we have selected the bands at 880 cm^{-1} ν_s(C-C + C-O) and at 1760 cm^{-1} (first overtone of the band at 880 cm^{-1}) for ethanol [87,52] and the band at 1640 cm^{-1} for water (bending mode) and followed their evolution with time. The choice of the bands has allowed us to obtain unsaturated signals during the overall evaporation process. In general, the choice of that bending mode of water is not the best one to follow the different components (given by different strength of the hydrogen bonds); the wider stretching band at higher energy (around 3300 cm^{-1}) allows a better separation. In the present case the saturation of the water stretching bands observed even at low water contents in the ethanol-water mixtures has restricted the choice to the water bending mode at 1640 cm^{-1}.

Figure 4.1 shows the 3D time-resolved infrared spectra of an evaporating droplet of ethanol; the time evolution of the band at 880 cm^{-1} is shown. The *x*-axis represents the wavenumber, the *y*-axis the time scale in seconds and the different colours the intensity scale. From this image the evaporation of ethanol appears as a continuous process, the same evaporation rate is observed during all the experiment. We have also analyzed the 1850-1580 cm^{-1} region in detail; the water bending mode (~1640 cm^{-1}) and the ethanol first overtone of 880 cm^{-1} band fall in this interval. Traces of water are present even in pure ethanol whereas more water might be adsorbed from the external environment during the evaporation process. The bending mode of water is, indeed, clearly observed and it appears to have a much more complex time-dependent behaviour than ethanol, which shows a constant evaporation rate.

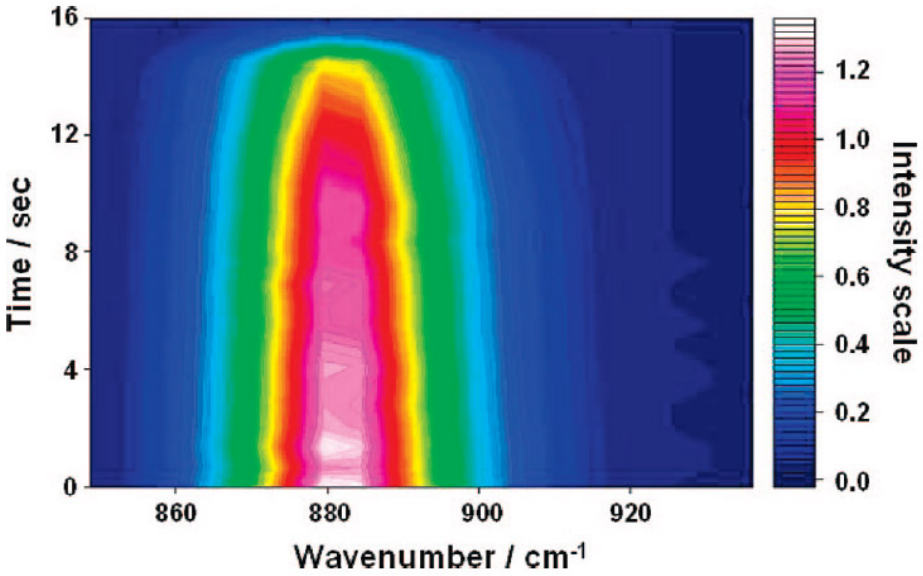

Figure 4.1: Three-dimensional FTIR image in the 850-930 cm^{-1} range obtained during the evaporation of a cast droplet of ethanol.

Figure 4.2 shows the 3D time-resolved infrared spectra of water in the ethanol evaporating droplet, a maximum can be clearly observed. We have reported in a separate graph the changes in absorbance of the peak of the water and ethanol bands as a function of the evaporation time (Figure 4.3).

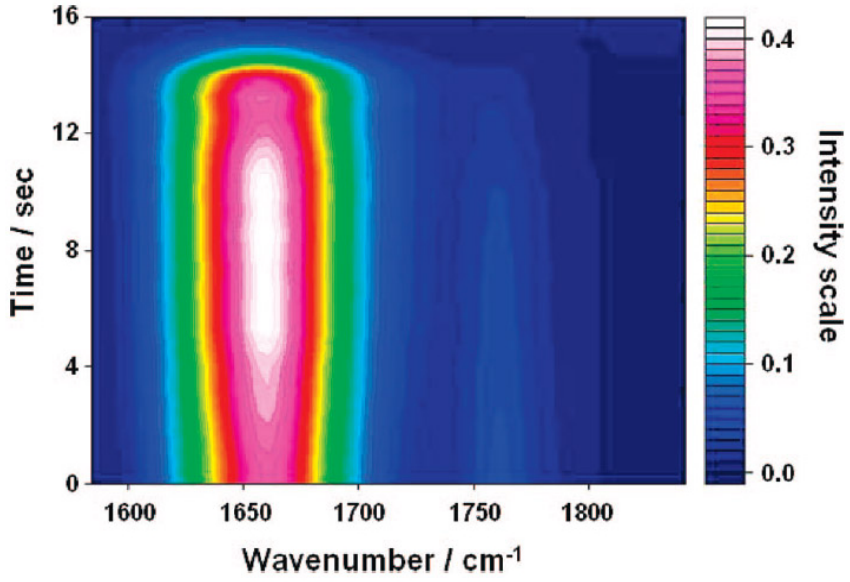

Figure 4.2: Three-dimensional FTIR image in the 1580-1850 cm^{-1} range obtained during the evaporation of a cast droplet of ethanol.

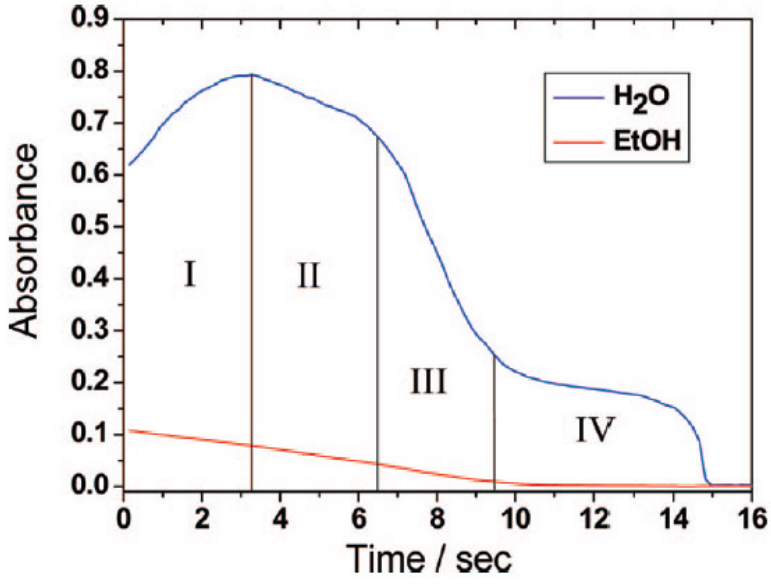

Figure 4.3: Changes in absorbance of water (~1660 cm^{-1}), blue line, and ethanol (~1760 cm^{-1}), red line, bands as a function of evaporation time.

As we have observed in the 3D time-resolved spectra, the evaporation of ethanol is continuous with a constant evaporation rate, while the spectra of water as a function of time are the result of a complex absorption-evaporation process. We have identified four different trends for water: (I) a

first stage during which water is adsorbed by ethanol from the external environment, this process reaches a maximum after few seconds from the beginning of the evaporation. It is interesting to observe that the water content in the evaporating droplet increases even if ethanol continuously decreases. (II) Water, after reaching a maximum, starts to evaporate: this is indicated by a decrease of the curve intensity. (III) The curve shows a drastic change of the slope and after this point, which is at around half of the process, the evaporation is very fast. This stage corresponds to the last part of ethanol evaporation. (IV) Ethanol is completely evaporated; the small residual droplet is now composed only of water, which eventually evaporates in a few seconds. We can also observe, from the simultaneous evolution of water and ethanol intensities, that even if water exhibits a complex behaviour, which is evidenced by four different evaporation stages, this does not affect the ethanol evaporation rate, that remains constant. The results on ethanol evaporation are in good agreement with previous findings: experiments conducted by studying the evaporation rate and the drop profile of pure ethanol have shown that there is a monotonic evolution with time [80]. These experiments, however, do not take into account the possible presence of water, which can be observed only by using time-resolved infrared spectroscopy.

We can also analyze more in detail the evolution of the water band by using 2D correlation infrared analysis, as this method has revealed to be very effective to study the water structure [88]. We have built the asynchronous spectra in the 1800-1540 cm^{-1} interval. An average spectrum was used as the reference for the analysis of the 2D spectra. Figure 4.4 shows the asynchronous 2D spectra of an evaporating water droplet, three correlation squares can be built; the correlation spectra have been obtained by extracting the FTIR spectra corresponding to the evaporation steps (stages from II to IV in Figure 4.3).

One of the advantages of 2D analysis is the improved resolution that can be achieved, in this case we can identify four different species that respond to the change of the external variable (in this case, time). Three of these bands are attributed to water (1630, 1670, 1720 cm^{-1}) [89,90] and the fourth one to ethanol (1760 cm^{-1}). The water network structure is generally described by a simple model, which is based on three levels of connectivity [91]. Gaussian fitting of the wide stretching band around 3300 cm^{-1} gives three components that are assigned to "*network water*" (~3320 cm^{-1}), "*intermediate water*" (~3465 cm^{-1}) and "*multimer water*" (~3585 cm^{-1}) [92]. The bending mode (~1650 cm^{-1}) of water is much narrower and much less sensitive to changes of the network structure; identification of the different components on the basis of the literature is also difficult because of the lack of systematic data. Previous studies of water confinement in micellar systems have, however, allowed to identify at least two Gaussian components at ~1625 and ~1660 cm^{-1}, which have been attributed to "*intermediate water*" and "*network water*", respectively [90,93]. 2D

correlation spectra suggest, in the present case, the presence of three correlated components. On the other hand, also the fitting that we have performed using the water bending bands obtained from the time-resolved analysis, is achieved by using three Gaussian components. We attribute the three bands that we have resolved in the bending mode of water by Gaussian fitting and the correlated peaks from 2D correlation analysis to "*multimer water*" (1630 cm^{-1}), "*intermediate water*" (1670 cm^{-1}) and "*network water*" (1720 cm^{-1}), in accordance with the simple model for water structure.

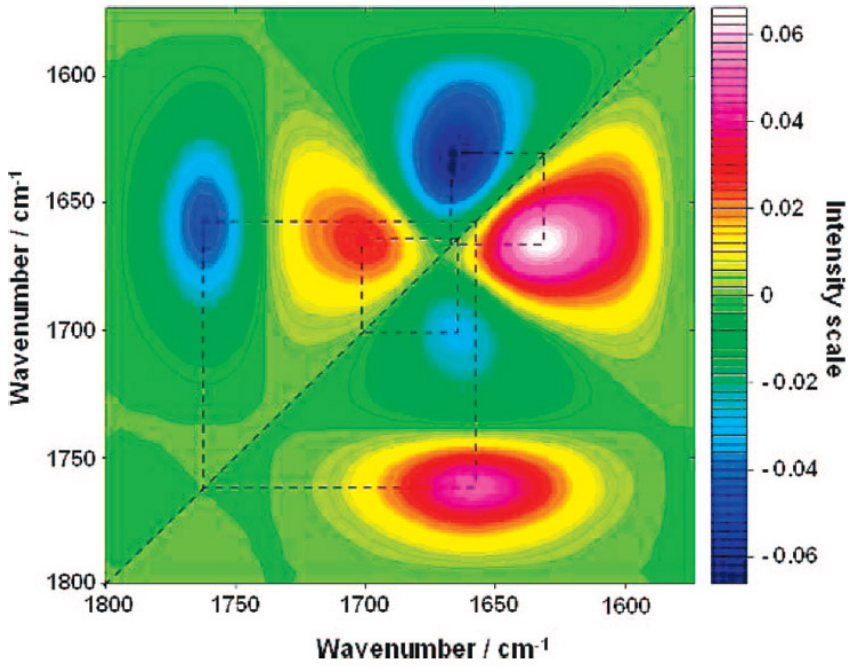

Figure 4.4: Asynchronous 2D infrared correlation plot in the 1800-1580 cm^{-1} range of an ethanol evaporating droplet.

The correlation squares in 2D correlation spectra show that there is an asynchronous correlation between ethanol and *intermediate water*: the two bands respond to the time change, but one increases in intensity while the other one shows a simultaneous decrease. In addition, there are other asynchronous correlations: *intermediate water-multimer water* and *intermediate water-network water*. To interpret these 2D data, we have to keep in mind that the water bands have a complex evolution with time: they increase and decrease in intensity and do not have a monotonic trend; furthermore small overlapping of the bands are present and this can be also a source of error. In particular, overlapping of the ethanol first overtone with the bending mode of water and overlapping of water with the tail of the δ_a(HCH) band of ethanol are observed. The different correlation peaks shown by the 2D correlation spectra could be, therefore, originated by the overlapping of these bands. To clarify this point, we have performed similar experiments of evaporation of pure water (see also the next section). In this case the FTIR time rapid scan experiments are very difficult to perform in the middle infrared range because even the signal from

the bending band is easily saturated. We were able, however, to record good signals from the last stage of the water evaporation and we have used these data to obtain a 2D asynchronous spectrum of evaporating water in the 1550-1750 cm^{-1} range (Figure 4.5). In this case ethanol overlapping can be discarded and we still observed three components for evaporating water, which we can attribute to the presence of the different correlated components in the bending mode of water. The complex evaporation process shown by water is likely correlated with the presence of different water species; adsorbed water appears to be the main responsible for the first and second stage, whereas the other components mostly evaporate during stages III and IV.

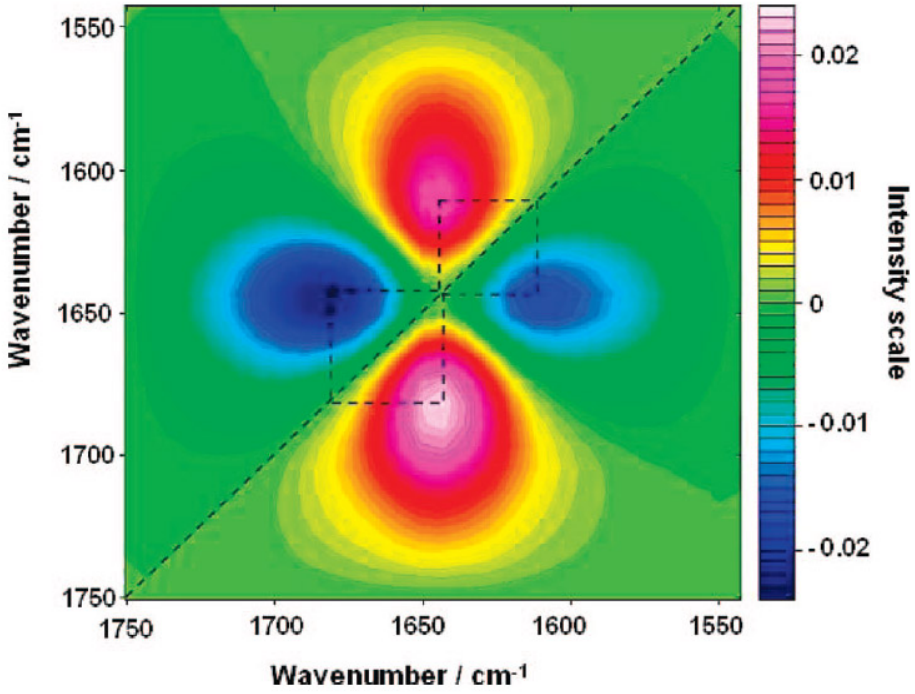

Figure 4.5: Asynchronous 2D infrared correlation plot in the 1800-1540 cm^{-1} range of an evaporating droplet of pure water. The 2D spectra have been obtained taking the water spectra relative to the last stage of evaporation.

We have extended the time-resolved rapid scan experiments to water-ethanol mixtures. Controlled amounts of water have been added to pure ethanol to obtain binary mixtures, in the 1-10 vol% of water in ethanol. This interval has been selected taking into account the azeotrope of the ethanol-water mixture, which is at the liquid composition of 95.5% in ethanol and 4.5% water, percentage by weight [94]. We have, therefore, monitored the evaporation of mixed compositions close to the azeotrope. Figure 4.6 (a-f) shows the evolution of water and ethanol peak intensity with evaporation time; the results show that in all of the ethanol-water mixtures, the ethanol evaporation rate remains constant, as in the case of pure ethanol. With the increase of water content, however, there is a change in the different evaporation stages, whereas four stages are still observed in the 99%EtOH-1%H_2O composition, in the other compositions only three stages are detected. It must be observed

that in the compositions in which the water content is higher than 1 vol%, the signal of the bending mode of water results saturated at the beginning of the evaporation. It is difficult, therefore, to state whether at higher water contents the first stage of water adsorption occurs or not.

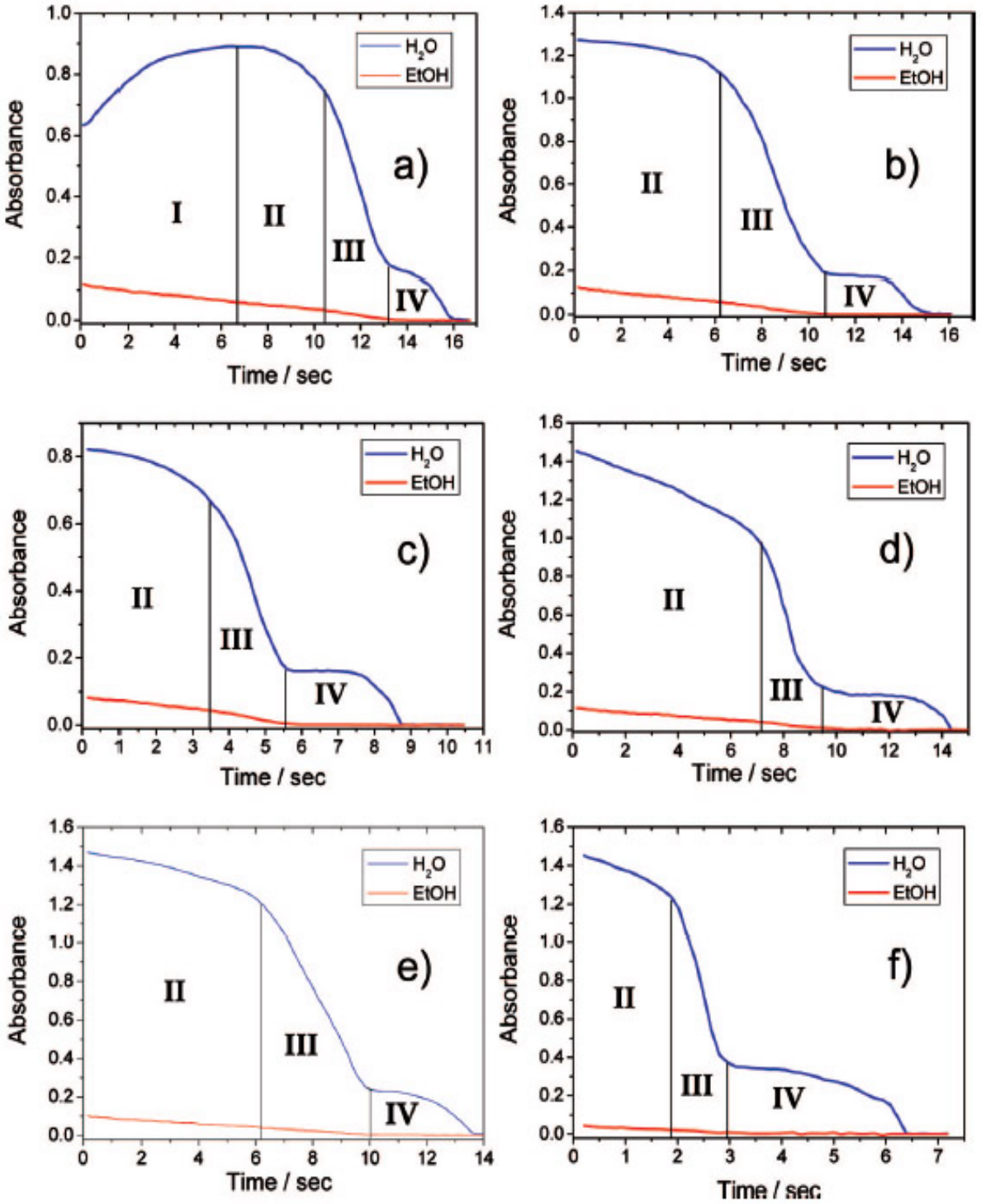

Figure 4.6: Changes in absorbance of water (~1660 cm^{-1}, blue line) and ethanol (~1760 cm^{-1}, red line) bands as a function of evaporation time for six different concentrations (from 99 (a), to 94 (f) vol% of ethanol) of ethanol-water binary mixtures.

4.2 Study of the evaporation of water and of deuterated water by time-resolved FTIR spectroscopy

After studying the evaporation of ethanol, we drew our attention to the evaporation of water, which is an other fundamental constituent of the mother solution in sol-gel processing of mesoporous thin films. Understanding not only the evaporation of ethanol, but also the evaporation of water is a mandatory step to increase the reproducibility of film formation and to develop applications. As a matter of fact, controlling the external conditions in the deposition environment is very important because the relative humidity strongly affects the overall process.

Evaporation of water is very important for nanochemistry, but is also a fundamental general process that is ubiquitous in ordinary life. Several aspects of this very basic process still have to be understood, the main limitation is represented by the lack of time-resolved techniques that can be applied to monitor in-situ the evaporation process. Most of the studies have used contact angle changes as a function of time to follow the water evaporation. This method, however, gives only a limited set of information and does not allow to investigate the details of the chemical-physical features associated to the process [80,81,95,96]. An alternative technique to study evaporation-adsorption phenomena is rapid scan time resolved infrared spectroscopy. As shown in section 4.1 and in chapter 3, this technique has shown to be a very powerful tool to follow reversible and irreversible time-dependent chemical-physical phenomena that can be observed using interferometric methods in a millisecond time scale. We have applied RSTR infrared spectroscopy to observe the evaporation of both a water droplet and of a deuterated water (D_2O) droplet, cast on a solid substrate as a function of the relative humidity in the external environment. The technique has allowed getting a direct time-resolved observation into the evaporation of water.

4.2.1 Experimental setup and procedure

Deuterated water and double-distilled water were used for the evaporation experiments. Time-resolved in-situ IR analysis was performed at the SINBAD synchrotron infrared beamline (INFN, Frascati), using the same instrumentation described in section 4.1. Even a few micron thickness droplet of water cast on an infrared transparent substrate can easily give a saturated signal, especially at the first stage of the evaporation process. We have faced this problem optimizing the experiment in the near-IR region, where the water overtone and combination bands can be well resolved and not saturated signals since the beginning of the process have been obtained. RSTR measurements were performed by averaging 8 interferograms per spectrum for a total acquisition time of 1.23 s, with a time delay between the beginning of each acquisition of 10 s, at a spectral

resolution of 16 cm^{-1}. These parameters are the best compromise in terms of signal-to-noise ratio and resolution compared to the typical evaporation time of the investigated samples. We have optimized also the water droplet size; if the water droplet is too large the infrared signal will be saturated for most of the measurement time, on the other hand, smaller droplets show a very fast evaporation and are not suitable for time-resolved studies. The experimental conditions that we have selected are optimized for an evaluation of the physical changes of the system, but do not allow us to extract quantitative data, for example about the evaporation rate. We have repeated the experiment for several runs (up to ten for each experimental condition) in order to ensure reproducibility, and the experimental trend has been always the same; on the contrary, the time scale has been more difficult to reproduce because of the limited control of drop dimensions. The relative humidity (RH%) during the experiment was carefully monitored and the evaporation experiments were run at three different RH: 15, 30 and 45%, at 25°C and at room pressure.

In a typical experiment, a small droplet of H_2O or D_2O (50 μl) was cast on a ZnSe substrate and the measurement started immediately afterwards. The experiments were performed in transmission configuration, using a double-sided, forward-backward acquisition mode of the interferometer. The background spectrum of the ZnSe substrate was recorded as the average of 40 interferograms in the air. The results were analyzed by Bruker Opus 6.5 software, baseline was calculated by rubberband correction using 64 points.

4.2.2 Evaporation of water at different relative humidity

The evaporation of a water droplet cast on a ZnSe substrate has been followed using the ~5200 cm^{-1} band in the near-IR region, which is assigned to the second order combination of OH stretching (~3350 cm^{-1}) and OH bending vibrational modes (~1650 cm^{-1}), $\nu_s^{01}(OH) + \delta^{01}(OH)$ [97]. The 5200 cm^{-1} band ranges from 4600 to 5400 cm^{-1} and has a maximum at 5190 cm^{-1}; the band is strongly asymmetric with a long tail at low wavenumbers and appears formed by different components (Figure 4.7, left column) [88]. There is a general consensus in literature to assign this overtone band of water to several overlapped species, however, a detailed analysis of this combination band has failed to distinguish the substructures that are correlated to the vibrational sub-bands [97]. Our experiments of evaporation performed at different RH have given the FTIR spectra in Figure 4.7 (left column: a= 45% RH, b= 30% RH and c= 15% RH). The different spectra exhibit a similar trend, even if the evaporation experiment is performed at different relative humidity: a decrease in absorbance with no shift in the absorption maxima. A better representation of the time dependence of the phenomenon is given by 3D FTIR time-resolved spectra (absorbance-wavenumber-time) shown in Figure 4.7 (right column: d= 45% RH, e= 30% RH and f= 15% RH); the absorbance

intensity is represented by false colour change. The evaporation of the water drop appears as a continuous process and no significant differences emerge if the experiment is performed at different RH conditions. An asymmetry at the end of the process is observed in all the spectra, the 5200 cm^{-1} component seems the last to disappear, which can suggest that different water components evaporate at different rates. These experimental conditions have not allowed discriminating any contribution of water adsorbed from the external environment.

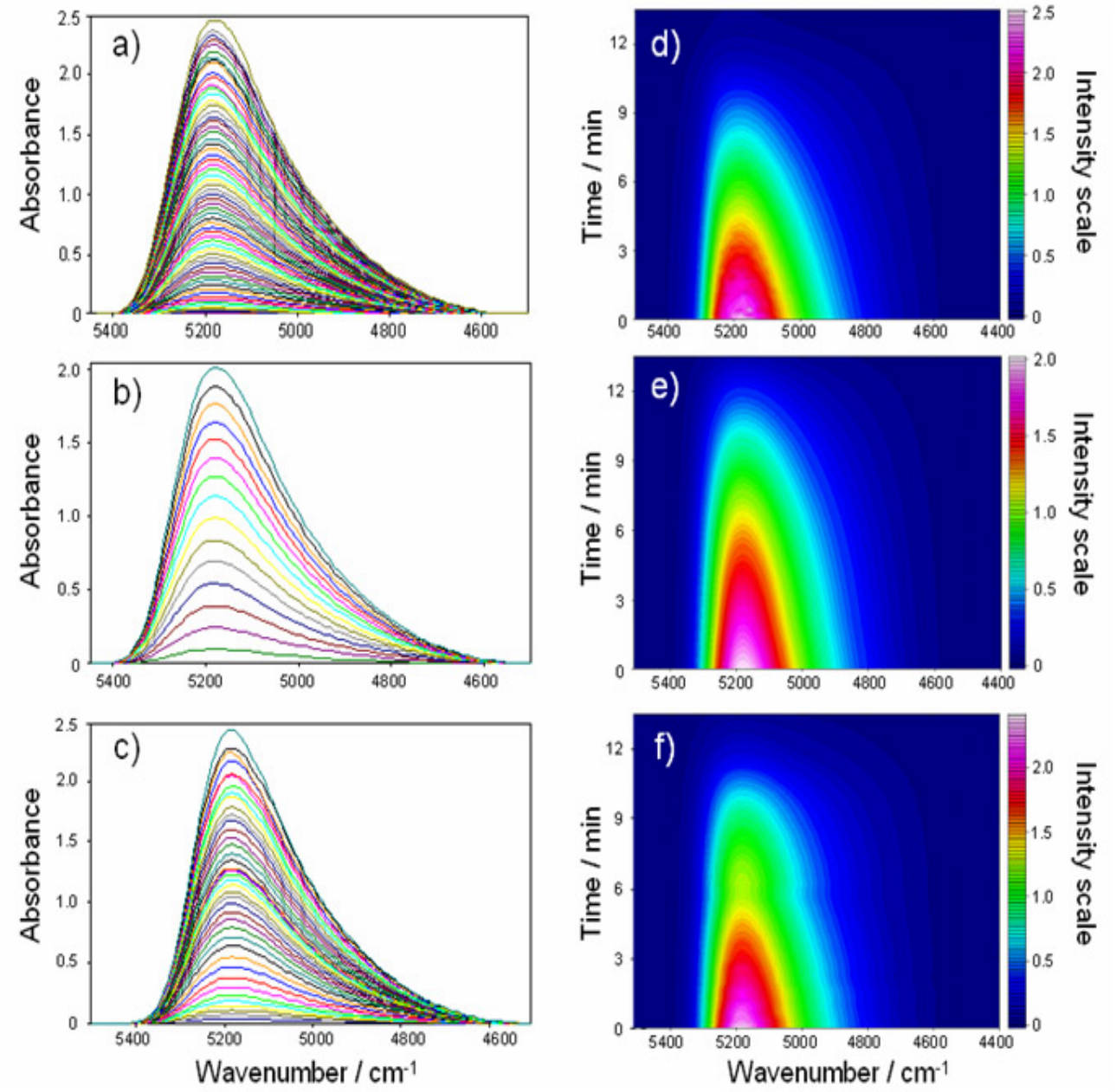

Figure 4.7: Rapid-scan time-resolved FTIR spectra in the 5500 – 4500 cm^{-1} range of an evaporating water droplet, a) 45% RH, b) 30% RH and c) 15% RH. 3D FTIR time-resolved spectra (absorbance-wavenumber-time), d) 45% RH, e) 30% RH and f) 15% RH; the absorbance variation is represented by false colour change.

4.2.3 Evaporation of deuterated water at different relative humidity

The water evaporation experiments performed by time-resolved FTIR spectroscopy have not shown any discontinuity in the process, even if adsorption of water from external environment should have been expected, at least at the higher RH conditions. The water adsorption is likely balanced by the evaporation of water at the first stages, this means that the process is slower at higher RH, but this effect is hard to detect, at least in the present experimental conditions because it is impossible to discriminate between evaporating and adsorbed water molecules. We have, therefore, performed evaporation experiments with deuterated water; because of the good separation between the vibrational modes of water and D_2O, this should allow, in principle, distinguishing contributions from the water molecules adsorbed from the external environment during the evaporation process.

Figure 4.8 (left column: a= 45% RH, b= 30% RH and c= 15% RH) shows the FTIR spectra recorded during the evaporation of a droplet of deuterated water cast on a ZnSe substrate at different RH conditions.

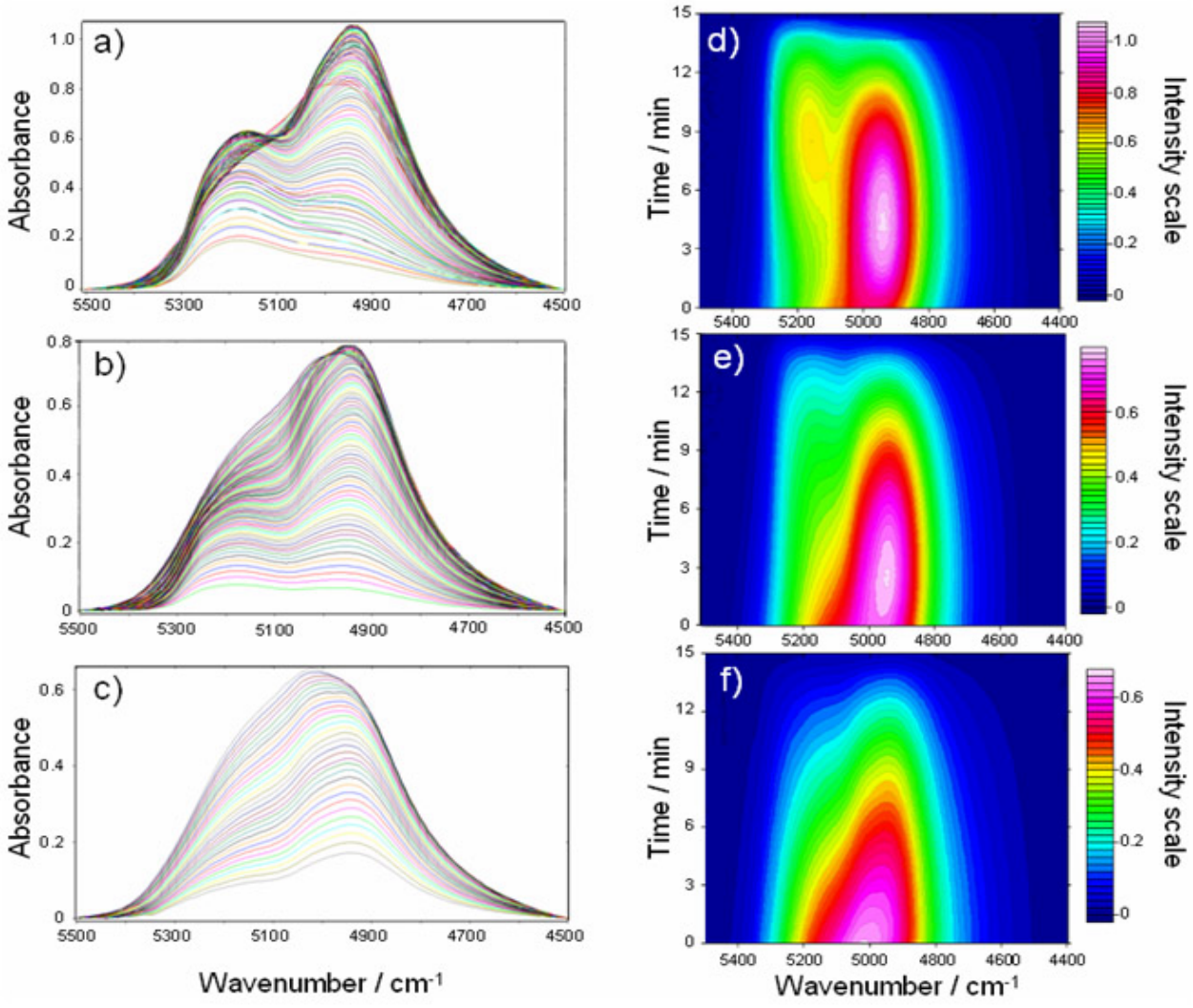

Figure 4.8: Rapid-scan time-resolved FTIR spectra in the 5600 – 4400 cm^{-1} range of an evaporating droplet of deuterated water, a) 45% RH, b) 30% RH and c) 15% RH. 3D FTIR time-resolved spectra (absorbance-wavenumber-time), d) 45% RH, e) 30% RH and f) 15% RH; the absorbance variation is represented by false colour change.

The FTIR spectra range from 4500 to 5500 cm^{-1}, and are strongly asymmetric; a strong difference is observed in the spectra recorded at different RH which appear formed of different overlapped vibrational modes. The main band shows an absorption maximum around 5000 cm^{-1}, which is attributed to the first overtone of the stretching mode of D_2O [98]. This band has shown to be sensitive to temperature variations and up to five components have been separated by Gaussian fitting [98]. An overlapped band of medium-strong absorbance is detected around 5200 cm^{-1}, which is attributed to the combination band of water (*vide supra*); this band has a different absorbance as a function of evaporation time and relative humidity conditions. The 2D spectra (wavenumber-absorbance) do not allow, however, identifying a clear time dependent trend; visualization of the data by 3D spectra (absorbance-wavenumber-time) gives, instead, a direct indication of the time dependency of the phenomenon. We attribute the 5200 cm^{-1} water component to water adsorbed from the external environment, which is supported by the trend shown in Figure 4.8 (right column: d= 45% RH, e= 30% RH and f= 15% RH): the absorbance of the water combination band is getting stronger with the increase of the RH in the experimental room, only a small perturbation of the signal is observed at 15% RH, whilst at 45% RH another peak appears in the middle of the evaporation process. The H_2O combination band (5200 cm^{-1}) and D_2O stretching first overtone band (5000 cm^{-1}) appear enough separated in the 3D spectra to give a direct visualization of the different trends during the evaporation process. We have not tried any deconvolution analysis because both the bands are formed by several water and deuterated water components that are difficult to resolve. If we use a simple water model (three main water species) we should assume at least six components, three each one for water and D_2O, and with a high uncertainty due of the high overlapping of the bands. If we look to the maximum of absorbance of deuterated water (5000 cm^{-1}) we observe that is shifted to longer times when the evaporation process occurs at higher RH values. It is difficult to state if this is a true phenomenon or is generated by the overlapping of the adsorbed water, which causes a translation of the peak to longer times; on the other hand the 3D spectra clearly show that a higher RH induces a stronger water adsorption. Some interesting observations about the time scale of the water adsorption can be also drawn on the basis of the present results: the more the evaporation of deuterated water proceeds, which means also spreading of the drop and increasing of the evaporation rate, the more water is adsorbed on the drop surface. The maximum of water adsorption is, in fact, observed after more than half of the evaporation process has been completed.

As we have previously pointed out, the partial overlapping of water combination band and deuterated water first overtone stretching mode does not allow a clear separation between the water adsorption and deuterated water evaporation phenomena. We have, therefore, used the band around

7000 cm^{-1} to follow directly the water adsorption process. This band ranges between 7200 and 6500 cm^{-1} and is assigned to the second overtone of the water stretching mode; it has a lower intensity in comparison with the 5000 cm^{-1} band and appears also strongly asymmetric with a tail at the lower wavenumbers, but is well separated from other overtones and combination bands of deuterated water and can be used to follow the kinetics of the water adsorption process. The 3D FTIR spectra in the 6400 – 7300 cm^{-1} range are reported in Figure 4.9 (a= 45% RH, b= 30% RH and c= 15% RH); they show the absorbance changes as a function of time of the second overtone stretching band of water. The spectra show that the water adsorption from the external environment does not follow a sudden mechanism, but it increases with the time to reach a maximum after two third of the process; after that, the evaporation of the adsorbed water starts, as addressed by the decrease in the absorbance of the associated band.

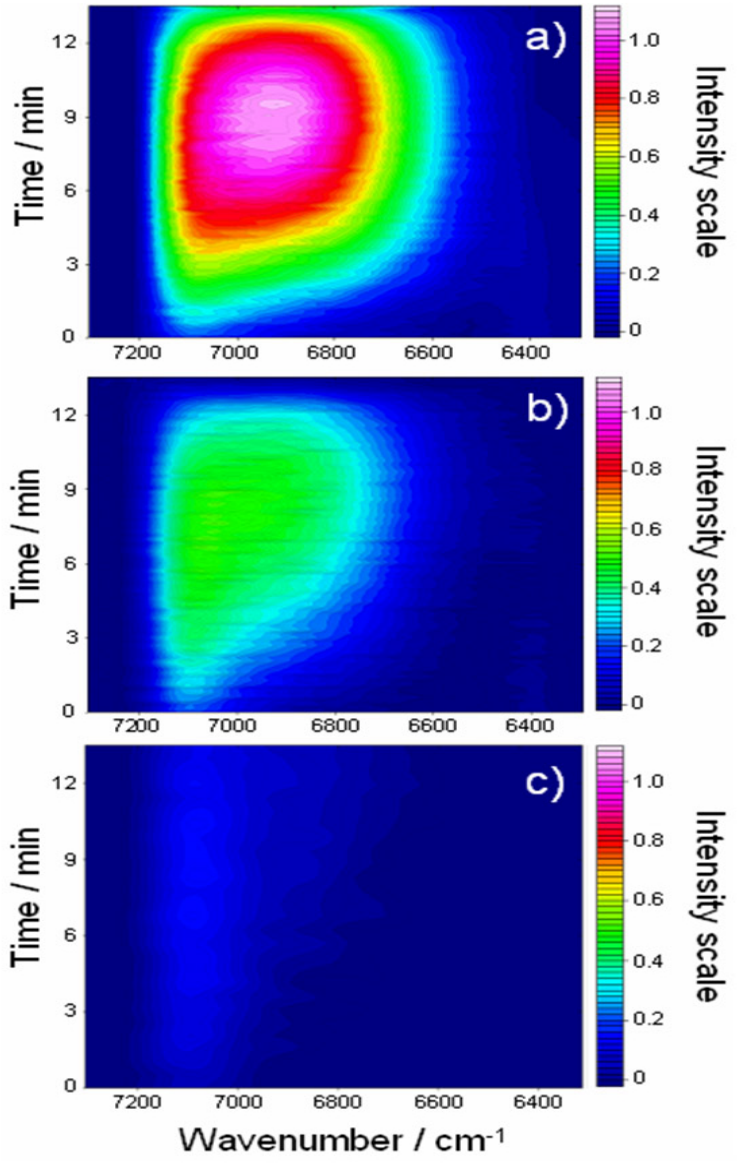

Figure 4.9: 3D FTIR time-resolved spectra (absorbance-wavenumber-time) in the range 7300 – 6300 cm^{-1}, a) 45% RH, b) 30% RH and c) 15% RH; the absorbance variation is represented by false colour change.

The adsorption-evaporation process of water, as shown by the experiments with deuterated water, is a complex phenomenon whose kinetics is environment dependent in terms of temperature, pressure and RH. In the present experiment we have only changed one parameter, the RH, and water adsorption on evaporating droplets appears to play an important role. We have also tried to obtain some information about the different water species that contribute to the process; we have used a three Gaussian component model to deconvolute the time resolved FTIR spectra. The number of Gaussian components that can be chosen for the curve fitting is somehow arbitrary in absence of a fully descriptive model for water. In the simple model Gaussian fitting of the wide stretching band around 3300 cm^{-1} is achieved by three components which are assigned to "*network water*" (~3320 cm^{-1}), "*intermediate water*" (~3465 cm^{-1}) and "*multimer water*" (~3585 cm^{-1}) [92]. We follow this simple three component model at different energies to have at least an indication if different water species are adsorbed-desorbed in a similar way during water evaporation. We have deconvoluted the FTIR spectra in the 7300 – 6500 cm^{-1} range using three Gaussian components at different wavenumbers, which are the second overtone of the corresponding *network*, *intermediate* and *multimer water* components. Figure 4.10 shows the results of fitting, the data are reported in a 3D plot (wavenumber-time-absorbance); the spectra recorded during evaporation experiments at 15% RH (Figures 4.10 a,b,c) are very noisy because of the very low absorbance of the band. A very small amount of water is adsorbed at this low RH value, which is close to the detection limit. The time-dependent evolution of the different Gaussian components as a function of the external RH is shown in Figure 4.10: the three water components appear centred around 6850 cm^{-1} (*network water*) (Figure 4.10a (15%RH), 4.10d (30%RH), 4.10g (45%RH)), 7050 cm^{-1} (*intermediate water*) (Figure 4.10b (15%RH), 4.10e (30%RH), 4.10h (45%RH)) and 7100 cm^{-1} (*multimer water*) (Figure 4.10c (15%RH), 4.10f (30%RH), 4.10i (45%RH)). The data show that the first component to evaporate is *multimer water*, (but more likely this can also indicate the disruption of the hydrogen bonded network of stronger strength in favour of the less structured components, *vide infra*), followed by *intermediate* and *network* water. Figure 4.11 shows the change of the absorbance as a function of evaporation time for the three different water components during the evaporation of D_2O at 45% RH. Even with the simple model we considered, the different mechanisms occurring during the evaporation of the water species give clear indications about the entire adsorption-evaporation process. During the first stage, the adsorption process is dependent on the external RH: the higher the RH, the higher the water adsorption from the external environment. The water adsorption proceeds with the time up to reaching a maximum, after this moment the adsorbed water also evaporates. If we consider a simple model of three main water components of different hydrogen strength, we can state that water evaporation proceeds through the disruption of more strongly

hydrogen bonded networks and the formation of smaller networks and clusters that finally evaporate.

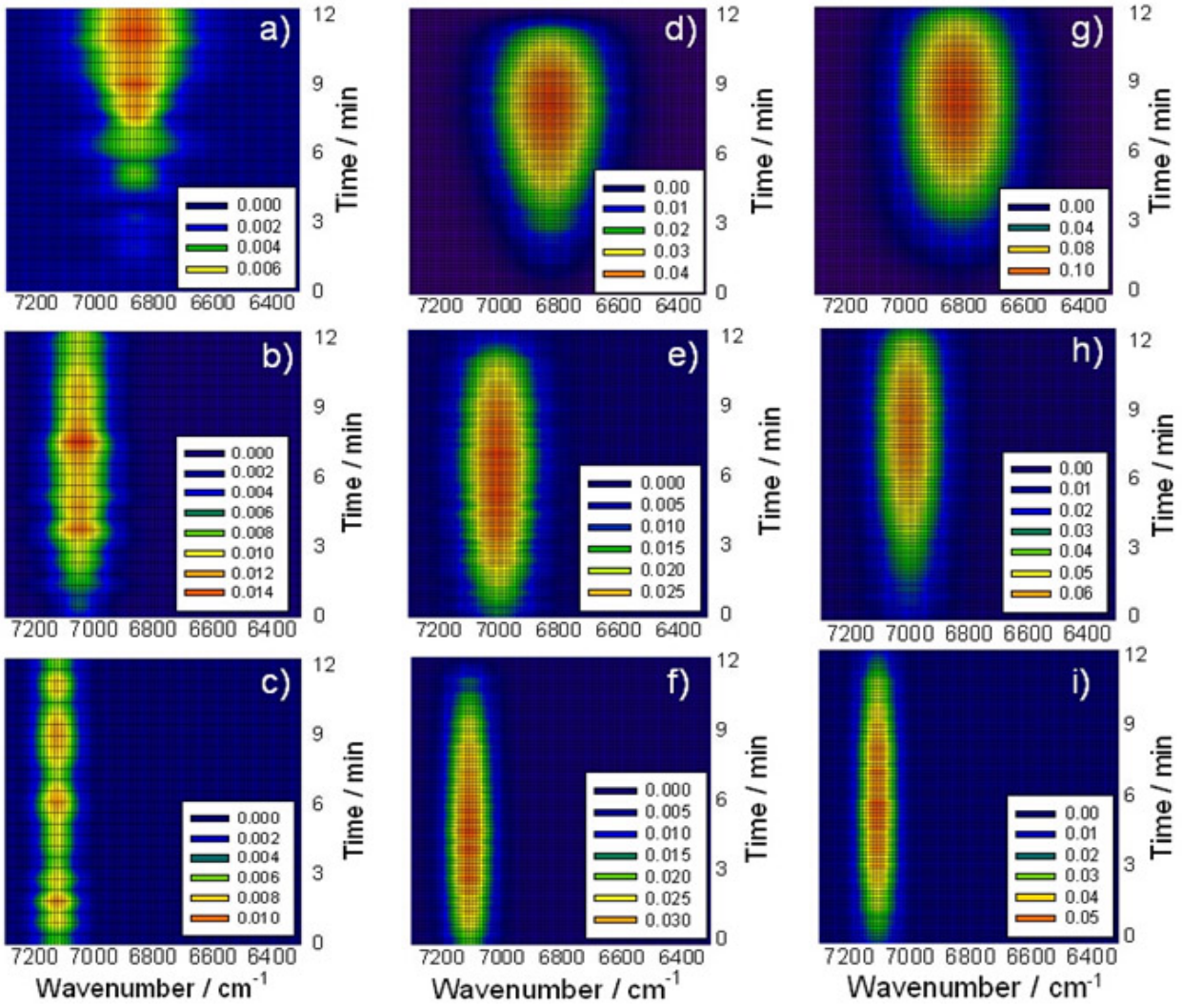

Figure 4.10: Time-dependent evolution of the three Gaussian components used to fit the second overtone stretching water band as a function of the external RH: ~6850 cm^{-1} (*network water*) a) 15% RH, d) 30% RH, g) 45% RH; ~7050 cm^{-1} (*intermediate water*) b) 15% RH, e) 30% RH, h) 45% RH and ~7100 cm^{-1} (*multimer water*) c) 15% RH, f) 30% RH, i) 45% RH.

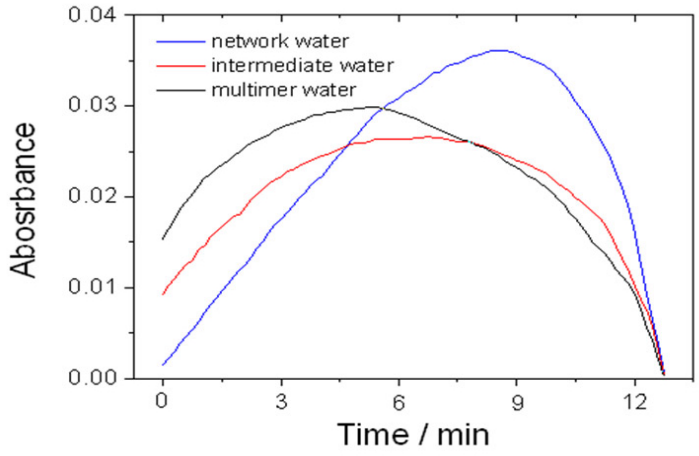

Figure 4.11: Change of the absorbance as a function of evaporation time for the three different water components during the evaporation of D_2O at 45% RH; ~6850 cm^{-1} (*network water*), blue line; ~7050 cm^{-1} (*intermediate water*), red line and ~7100 cm^{-1} (*multimer water*), black line.

4.3 Stain effects studied by time-resolved FTIR imaging

Pattern formation in evaporating colloidal droplets is an important phenomenon that is commonly observed in several solute-solvent systems. After evaporation of the solvent a ring-like pattern remains onto the solid substrate under the condition of contact line pinning. The formation of ring-like stains by evaporation of a drop containing a solute onto a solid substrate is caused by capillary flows to the edge of the drop [99]. This effect does not depend on the solute-solvent combination or on the substrate and is observed under the condition that a geometrical constraint pins the contact line to the initial position [100]; the evaporation of the solvent is balanced by a capillary flow towards the pinned drop edge. It has been demonstrated that if pinning is accompanied by a non-uniform evaporation of the solvent, the mass conservation requires a flow towards the contact edge [101]. Roughness of the surface plays a very important role to induce pinning of the droplet at the contact edge, on the other hand it has also been demonstrated that "self-pinning" can be observed on a smooth surface due to accumulation of solid particles at the contact line. In this last case different types of patterns arise from the competition between de-wetting and contact line pinning [101]. The formation of ring-like stains induced by evaporation of a drop has been observed for a large variety of solvent-solute systems, in aqueous and non-aqueous solvents and for solutes of different sizes [100], from molecular (dye molecules) up to colloidal scale (polystyrene microspheres) [102]. Some control of the ring shape and thickness is obtained through the manipulation of the evaporation conditions, such as the vapour field around the evaporating droplet: different patterned ring-like stains are obtained [100]. A theoretical model for an evaporating colloidal droplet has been proposed and related experiments have shown that three evaporation modes are possible [103], *edge-enhanced evaporation* (free evaporation of the droplet), *constant evaporation* (the experimental conditions are controlled to achieve a constant evaporation condition across the droplet) [100] which produces ring patterns and *centre-enhanced evaporation* (evaporation mainly is occurring around the droplet centre), which conversely gives a uniform stain without rings.

Controlled stain effects can be used to pattern solid surfaces by a self-assembly mechanism and several applications in nanotechnology have been envisaged [104]. More in general, drying mediated phenomena appear as an emerging bottom-up technique to obtain self-assembled and ordered surfaces from micro and nano-objects [105]. Evaporation phenomena have been also the subject of several works [106], even if the complexity of the processes is far to be exhaustively understood; several important technological applications, such as DNA microarray manufacturing are affected by stain effects upon solvent drying [107]. Evaporation is a typical time-dependent

phenomenon whose kinetic depends on several parameters and on the experimental conditions. Different analytical techniques have been used to investigate such type of complex phenomena, but some fundamental experiments still have to be performed especially in a time resolved scale. As we have shown previously, FTIR spectroscopy is a very effective technique to investigate non repetitive time-resolved phenomena on a millisecond scale and has allowed to elucidate the adsorption of water under different relative humidity conditions during the evaporation. All these considerations led us extend this method, applying a time-resolved infrared imaging technique to the evaporation of a water droplet containing an organic dye, methylene blue, to study the stain effect induced by evaporation. The technique has the advantage to allow, within a second scale, the reproduction of an infrared spatial image of the droplet and simultaneous phenomena, such as mass transport and water evaporation at the contact edge, can be analyzed at the same time.

4.3.1 Experimental setup and procedure

Time-resolved in-situ IR analysis was performed at the SINBAD synchrotron infrared beamline (INFN, Frascati), using a Bruker Hyperion 3000 microscope with a conventional Globar source and a KBr beam-splitter. The IR imaging was performed in the wavelength range of 900–5600 cm^{-1} with a resolution of 8 cm^{-1} by a Mercury-Cadmium-Telluride 64x64 pixel focal plane array (FPA) detector cooled to the liquid nitrogen temperature.

Time-resolved imaging measurements were performed by averaging 16 interferograms per spectrum for a total acquisition time of 16 s, the time delay between the beginning of each acquisition was 45 s. These parameters are the best compromise in terms of signal-to-noise ratio and resolution compared to the typical evaporation time of the investigated samples. We have optimized also the water droplet size; if it is too large the infrared signal will be saturated for most of the measurement time, on the other hand, smaller droplets show a very fast evaporation and are not suitable for time-resolved studies. We have also considered the error that can be introduced because of the geometry of the droplet; rays near the edge of the droplet, in fact, have an angle of incidence that can be near grazing, so reflectance effects can be present. To calculate this error we have considered that the dimension of the droplet has an average diameter of around 2 mm, but only the edge of the droplet is illuminated by the IR light and the condenser of the microscope collects the light only from an area of 170x170 μm^2, which is less than 1/400th of the overall droplet area. Considering the Snell law and the water reflectivity, we have evaluated that the droplet geometry, as the upper limit, can introduce an error within 5% of the measured absorbance. The relative humidity (RH%) during the experiment was carefully monitored and kept at 45±2%, at room temperature and pressure.

Size and shape of droplets as a function of time were recorded using a CCD video camera equipped with a telephoto lens working in macro mode that magnified the images. The camera was placed on the same plane of the droplet substrate. For volume and contact angle measurements, snapshots of the drop profile were extracted every 45 s from the video camera acquisitions in simultaneous combination with the infrared images. The optical images were analysed using a commercial software for drop analysis.

Methylene blue (tetramethylthionine chloride, purity 90%) was purchased from Aldrich and used without further purification. The solution for the experiment was prepared dissolving 1 mg of the dye in 1 cc of bi-distilled water. After 5 minutes of stirring, a small droplet of solution (1.5 μl) was cast on a ZnSe substrate and the measurement started 10 s later. This time delay was necessary to select the border of the droplet before starting to monitor its time evolution. The experiments were performed in transmission configuration, using a double-sided, forward-backward acquisition mode of the interferometer. The background spectrum of the ZnSe substrate was recorded as the average of 64 interferograms in the air. The results were analyzed by Bruker Opus 6.5 software.

The image of the dried drop was taken by mapping the drop using the motorized sample stage of the microscope and selecting an area of 60x60 μm^2. by the adjustable upper aperture slits. The sample stage was automatically moved horizontally and vertically by steps of 60 μm on a grid of 36x36 points covering continuously a total area of 2.16x2.16 mm^2. The detector was a MCT cooled at the liquid nitrogen temperature. Each spectrum was recorded as the average of 20 interferograms and the background spectrum of the ZnSe substrate was recorded as the average of 100 interferograms in the air.

4.3.2 Experimental results and data analysis

The possibility to perform IR imaging time-resolved experiments opens new analytical possibilities such as to follow the evolution of different chemical species as a function of time and space. This technique allows a direct observation of the phenomenon in submicron and molecular systems; previous experiments performed using microspheres have been limited to micro range objects [99,100,101]. We have applied the technique to study some specific details of ring-like stain formation in a solute-solvent system composed of methylene blue in water.

We have followed the evolution of the ring edge during evaporation, at the point where self-pinning is achieved and the mass transportation gives rise to the ring formation. This is a particularly critical region for investigating ring-like stain formation because the presence of the solute affects the evaporation and the hydrodynamics at the droplet edge. Figure 4.12 shows the sequence of images (from a to f) taken from 180 s after droplet casting up to the end of the evaporation process, 450 s.

The images have been obtained by integration of the water band around 2150 cm^{-1}, which is formed by the combination of L_2 libration mode at 686 cm^{-1} and bending mode at 1640 cm^{-1}, in the 2300-1850 cm^{-1} range. Every image is 170x170 μm^2 and the position is indicated by the *X* and *Y* axes, while the intensity change of the absorption band is reported in a false colour scale.

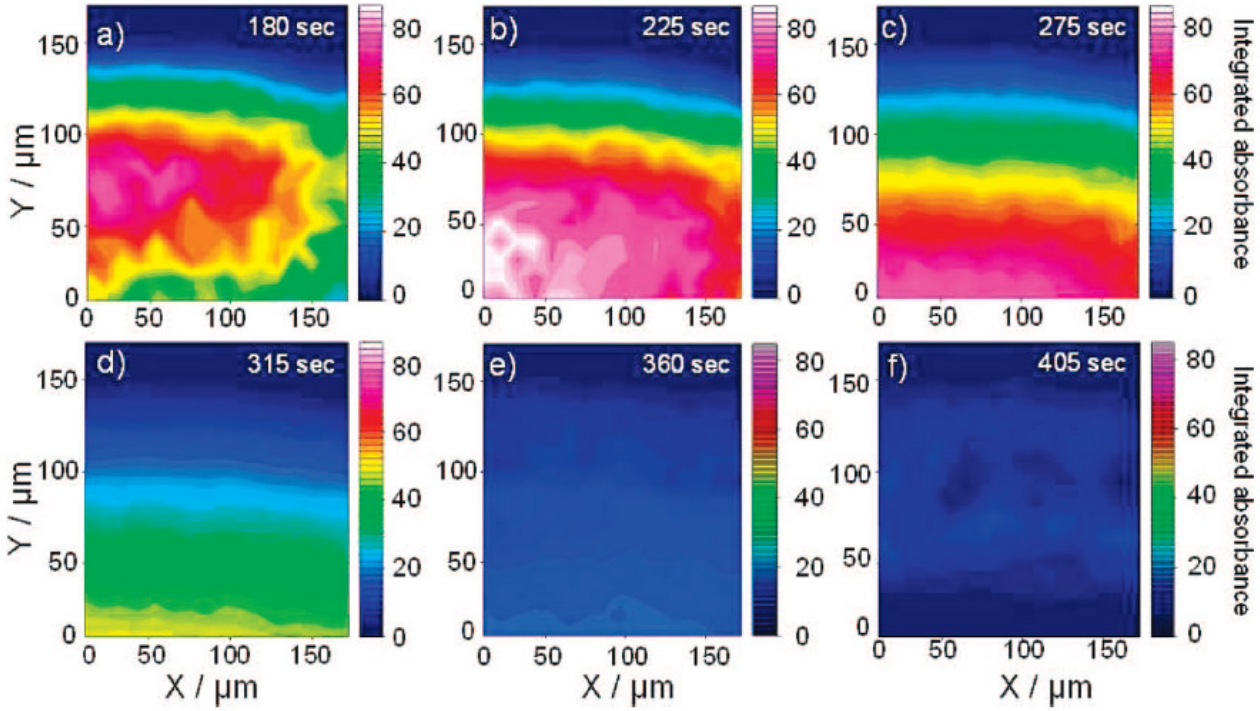

Figure 4.12: Sequence of infrared images (from a to f) taken from 180 s after droplet casting up to 450 s. The images have been obtained by integration of the water band around 2150 cm^{-1}, in the 2300-1850 cm^{-1} range. Every image is 170x170 □m^2, and the position is indicated by the *X* and *Y* axes, while the change of the integrated absorption band is reported in a false colour scale.

The sequence of infrared images allows following the changes in intensity of the water absorption band as a function of time and space, keeping in mind that we have monitored the droplet edge. The images give a direct evidence of the variation of the droplet profile as a function of evaporation time. The droplet appears pinned to the edge during the overall evaporation, as it is confirmed by optical images (vide infra); the water edge shows a continuous decrease in intensity during evaporation and from the centre to the droplet edge. The change in absorption intensity from the centre is correlated to the water droplet height and is a direct indication of the change of water droplet shape as the evaporation proceeds. If we extract a set of infrared data from the image matrix, such as the FTIR spectra related to a selected *X* position (we have selected *X*=90µm in the images), we can reconstruct the change of the droplet edge geometry during evaporation. Figure 4.13 shows the change in absorbance versus *Y* position of the infrared absorption data as a function of time. What we observed is exactly the change of the droplet profile during the evaporation time,

the height of the droplet (in the present case represented by the absorbance intensity) decreases with time, and the contact line is pinned to the edge.

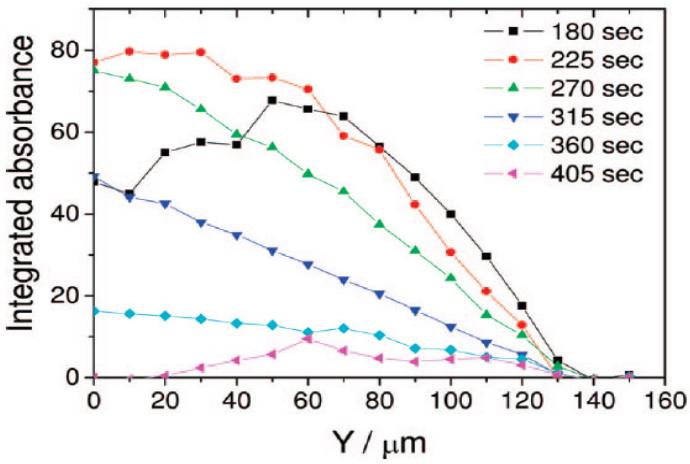

Figure 4.13: Change of integrated absorbance vs. *Y* position of the infrared absorption data as a function of time (*X*=90 μm in the images in Figure 4.12).

The advantage of time-resolved infrared imaging can be evaluated if we integrate a different band of the infrared absorption spectra used to obtain the sequence of images in Figure 4.12. The images shown in Figure 4.14 (from a to f) have been obtained integrating the 1600 cm^{-1} band of methylene blue, in the 1660-1540 cm^{-1} interval (see Figure 4.15), they allow to follow the mass transport to the edge during evaporation.

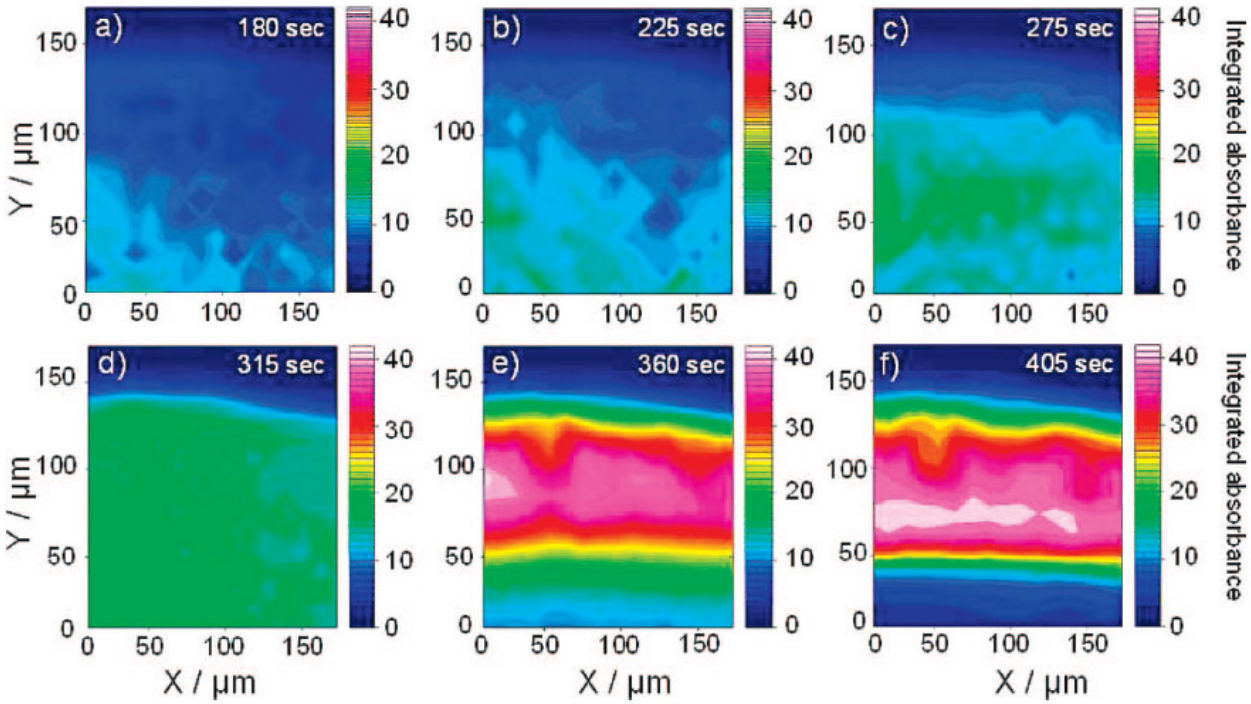

Figure 4.14: Sequence of infrared images (from a to f) from 180 s up to 450 s. The images have been obtained by integration of the band of methylene blue at 1600 cm^{-1}, in the 1660-1540 cm^{-1} range. Every image is 170x170 μm^2, and the position is indicated by the *X* and *Y* axes, while the change of the integrated absorption band is reported in a false colour scale.

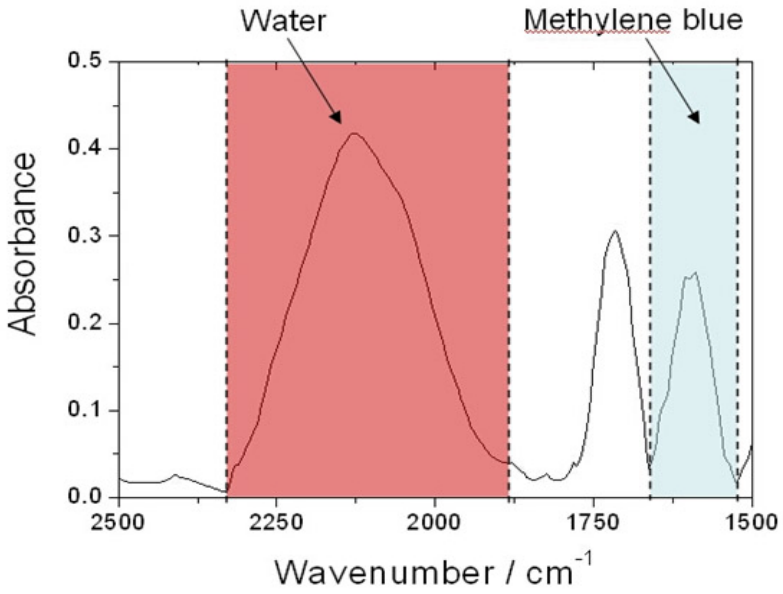

Figure 4.15: Typical FTIR absorption spectra of methylene blue dissolved into water. The red and blue regions are respectively indicating the integration range of the band attributed to water and methylene blue that have been used to build the 3D spectra of Figures 4.12 and 4.14.

In this case we observe a progressive increase in intensity along the *Y* position, a trend which is somehow opposite to that of water, and the final formation of a ring after water evaporation. The evolution of the droplet profile, expressed in this case in terms of methylene blue concentration, is reported in Figure 4.16, which shows the change in absorbance of methylene blue as a function of *Y* position. In this case we can consider the graph in Figure 4.16 as the time evolution of the evaporative mass flux during droplet evaporation; we can clearly observe the formation of the ring in correspondence of the end of the water evaporation process (Figure 4.13) and again the pinning of the contact line.

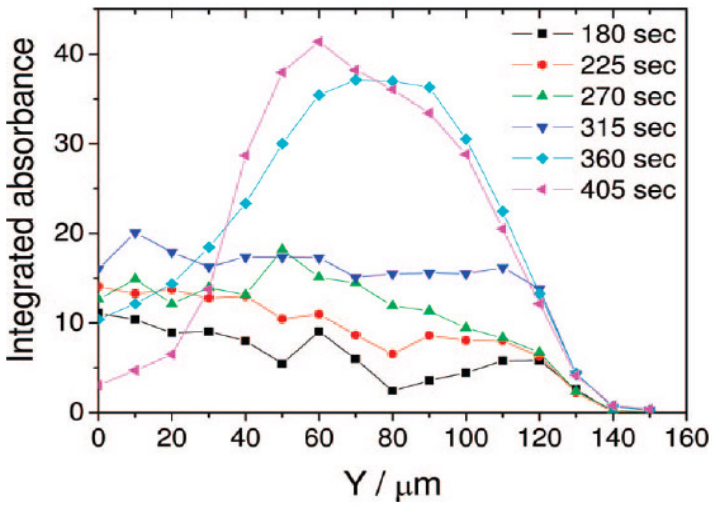

Figure 4.16: Change of integrated absorbance vs. *Y* position of the infrared absorption data as a function of time (*X*=90 μm in the images in Figure 4.14).

Our experimental set up is simple; the droplet has been allowed to evaporate on a ZnSe substrate in a closed box at constant RH, which was always kept around 45%; the experimental data show that conditions of controlled RH are enough to obtain constant evaporation. The result of the evaporation in constant conditions of the water-methylene blue system is a uniform ring of methylene blue, which is shown in the optical image (Figure 4.17a) and in the infrared chemical image (methylene blue) (Figure 4.17b); a methylene blue ring is formed at the end of the process.

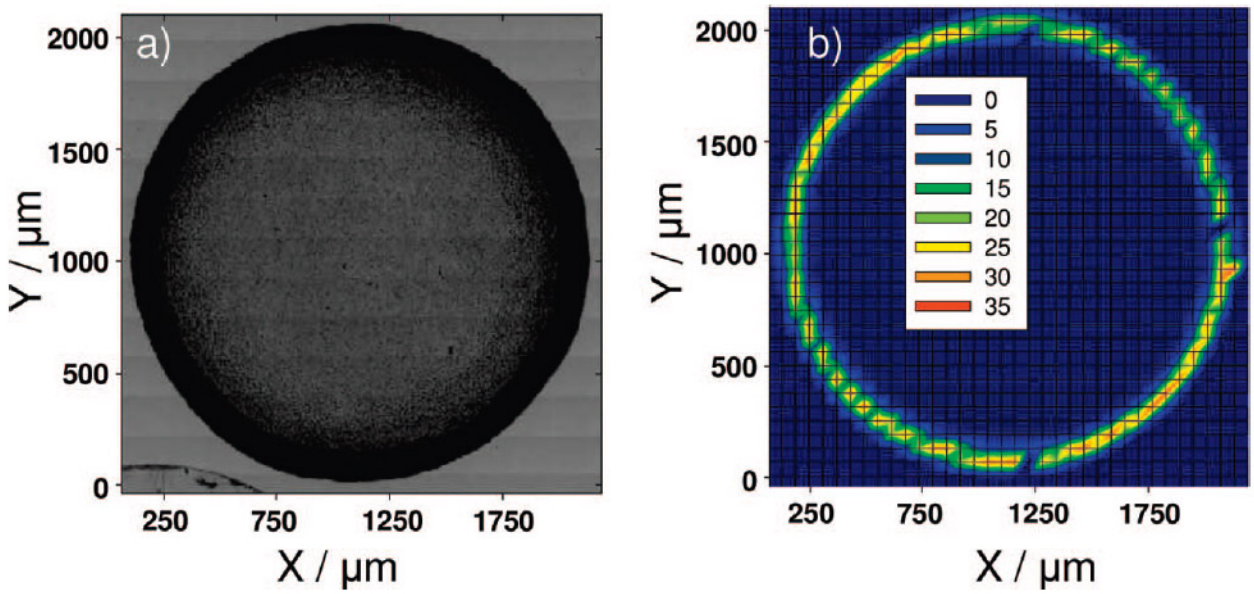

Figure 4.17: Optical image (a) and infrared chemical image (methylene blue) (b) taken at the end of the evaporation process of a water droplet with methylene blue. The false colour scale represents the variation of integrated absorbance of the 1600 cm^{-1} band of methylene blue.

The optical images of the evaporating droplet, recorded simultaneously to the infrared chemical imaging, are shown in Figure 4.18; the droplet, as previously observed by infrared images, appears pinned during all the evaporation process. We have measured the change in contact angle and drop height measured at the centre of the droplet as a function of evaporation time. They show a linear variation (Figure 4.19), both the curves have been fitted by a linear function. We can use these experimental results for a comparison with the theoretical predictions of the models proposed by Fischer [103] for particle convection in evaporating droplets. We correlate the increase in intensity of methylene blue in correspondence to the droplet edge with an increase in molecular flux in this region; the flux disappears at the contact line. The initial contact line pinning is produced by defects on the substrate; accumulation of dye molecules at the contact line maintains the contact line pinned during the evaporation. There is convection taking place from the centre toward the contact line because of not only matter conservation, but also because of increase of local energy due to the drop surface deformation (increasing of surface energy) and increase of solute concentration. This latter point, local increase of solute concentration, must be counter balanced by two phenomena: (a)

diffusion of solute in the opposite direction than the flux and (b) precipitation at the contact line. The precipitation is more likely to be the predominant result of the flow because it is kinetically favoured, fast precipitation because of oversaturated concentration at the borderline. This precipitation also tends to increase the interface energy at the contact line and to enhance capillary flow at the same time. The energy barrier to make the contact line move back to the centre, reducing the contact area of the drop, is thus increased with evaporation time and deposition of the methylene blue at the periphery and is thus unfavourable. The diffusion of methylene blue by osmotic pressure back to the centre to homogenize the concentration everywhere in the drop is less favoured as a result of the evaporating flow of the solution in the opposite direction.

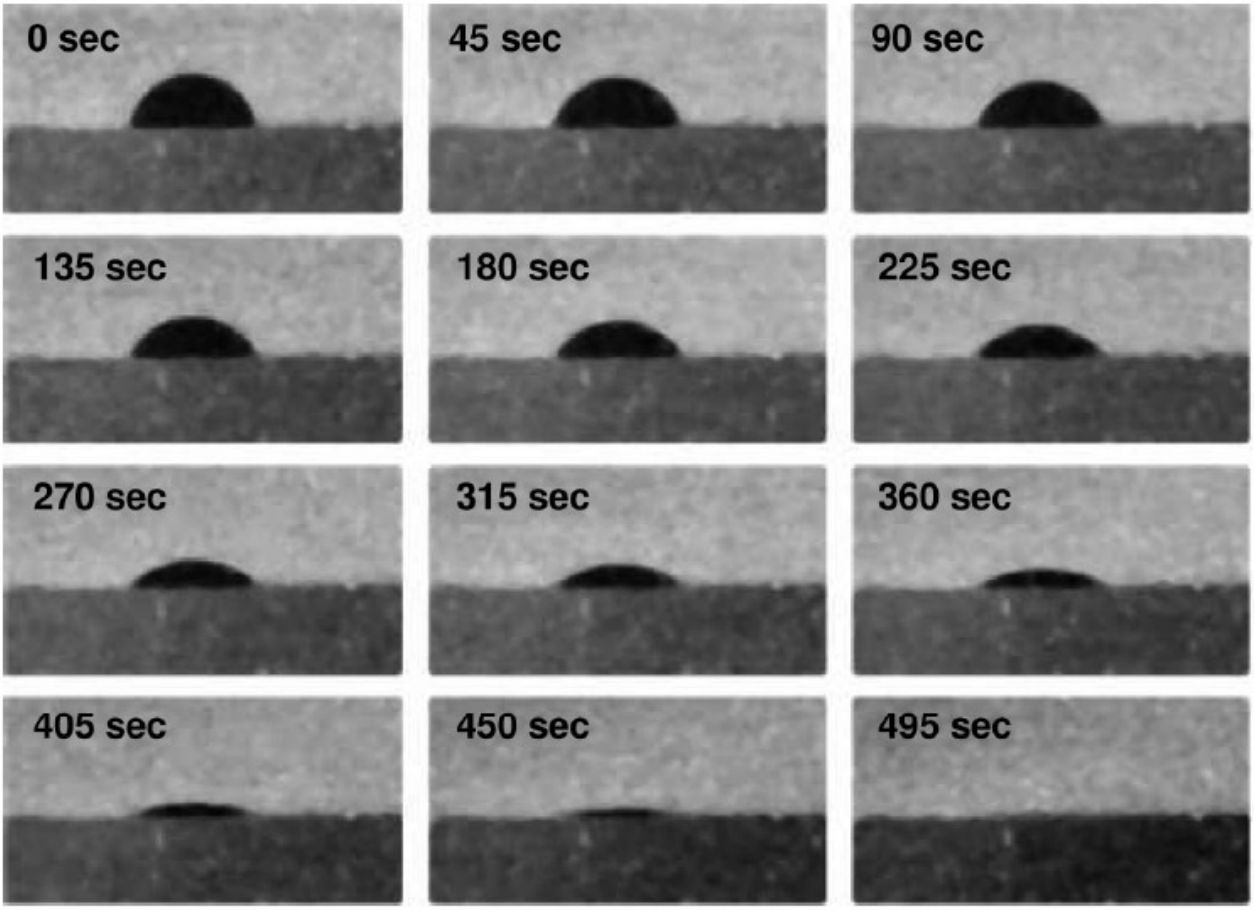

Figure 4.18: Optical images of the evaporating droplet as a function of time.

When these considerations are taken into account, the experimental results are consistent with a constant evaporation model; this is well supported by the linearity of the contact angle and volume curves during the evaporation process, while the time evolution of the dye transport does not show an increase close to the pinning line (Figure 4.16). On the other hand if we were in a condition of edge-enhanced evaporation we should have observed an increase of concentration just at the limit of the contact line and deviation from the linearity of the contact angle and volume variations with

evaporation time. The relatively high RH conditions (45%) in a close controlled room are enough to achieve constant evaporation conditions.

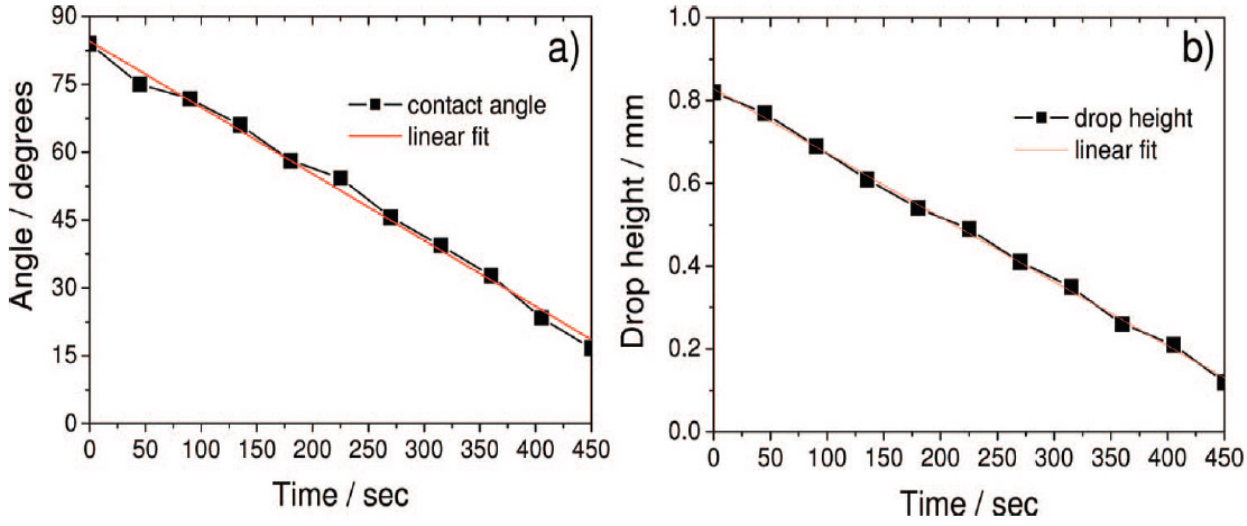

Figure 4.19: Contact angle as a function of evaporation time (a) and drop height as a function of evaporation time (b).

The experimental method that we have described can be applied to more general applications; we have applied the same technique to observe stain effects in solutions containing bacteria, and the method has shown also to be very effective even in quite different experimental conditions. The limit of the experimental conditions are represented by the saturation of the infrared signal; the applicability is, therefore, restricted by the possibility not to distinguish saturated bands during the overall measure. A careful selection of the band for integration has therefore to be done, and at the same time the droplet size has to be adjusted to get the best compromise in terms of signal-to-noise ratio and signal saturation. We can, therefore, state that this experimental setup can be used to study several types of different evaporation phenomena that are time and space dependent by a careful choice of the experimental conditions.

4.4 Fabrication of mesoporous functionalized arrays by integrating deep X-ray lithography with dip-pen writing

Combined bottom-up and top-down approaches to the synthesis of organised matter are attracting much interest due to the possibility of fabricating complex functional nano- and micro-structures for advanced applications [108,109]. Typically, the possibility of building structures defined at the atomic or molecular level is a prerogative of bottom-up syntheses, whereas complex structures such as micro- and nanoscopic interconnects and circuits can be obtained by top-down approaches,

which also are suited for industrial scale-up. Therefore, the development of specific technologies based on combinations of both types of synthetic approaches is an important goal for basic and applied research.

Self-assembled mesoporous thin films are a notable example of materials synthesised by a bottom-up approach [110,79]. whose integration in devices requires, however, top-down processing. Specific patterning of mesoporous films aimed at obtaining circuits or dot arrays is a task that cannot be fulfilled by merely dip-coating or spin-coating the precursor solution on a substrate without further processing. In particular, the bottom-up EISA technique used in the synthesis of mesoporous films needs coupling with top-down processing such as substrate pre-patterning or film lithography [79]. In this way, hierarchically-structured porous materials can be obtained, where organisation resides on multiple length scales: porosity (typically 2–10 nm), film thickness (50–500 nm) and pattern size (150 nm to 1.3 μm). The ordered mesopores constitute an ideal host to guest functional organic molecules or nanoparticles [111], while the patterns, from the nano- to the micro-scale, allow designing devices for different advanced applications [112], for example as DNA nanoarrays or lab-on-a-chip devices.

The possibility to pattern mesoporous films was first demonstrated by Brinker et al., who employed a wide range of lithographic techniques [113,114]. These were based either on mesophase change or on mesostructure disruption occurring upon irradiation with UV light. Alternatively, dip-pen nanolithography, ink-jet printing using a ‘‘self-assembling ink’’ [115], and selective de-wetting were used to obtain patterned mesoporous arrays and microfluidic devices. On the other hand, the need for high-tech integrated components requires more and more sophisticated lithographic techniques to achieve higher aspect ratios, a higher definition, the capability to pattern thick structures, higher resolution (depending on film thickness, down to few tens of nanometers), and the capability to define patterns of complex non-periodic shapes. It is important to underline that several of the possible applications that are envisioned for mesoporous materials, such as nano–micro arrays and lab-on-a-chip devices, have exactly these stringent requirements. At the moment there is a gap between the material development and the available technologies. With the aim of providing knowledge to close this gap, we have developed a highly integrated fabrication patterning process that is based on deep X-ray lithography [116] and dip-pen writing [117,118] of the mesoporous patterned arrays.

Deep X-ray lithography (DXRL) has never been used to obtain patterned mesoporous films. This is surprising, because the development of a technology for patterning mesoporous coatings based on X-rays has several advantages compared to other techniques such as dip-pen nanolithography (DPN) and UV lithography: for example, integration with the current fabrication techniques for

electronic devices, high aspect ratio, better lateral resolution (depending on film thickness, down to few tens of nanometres), possibility of patterning thick coatings and complex non-periodic structures, or periodic objects using the phase mask technology. It has been demonstrated that a peculiar property of mesoporous materials, the presence of a tunable steady state after film deposition, can be exploited for inducing reversible phase changes by X-rays [119]. These experiments were conducted on mesostructured hafnia films, but this processing can be generalised to develop a technology based on X-ray lithography on mesoporous films of different compositions, for instance silica and titania. In the work presented in this section we have strived to develop a patterning technology based on this mesoporous response to X-ray radiation. We have used DXRL to pattern mesostructured silica thin films. DXRL is a manufacturing process by which a material that is exposed to high-resolution, high-intensity and extremely collimated synchrotron radiation through an X-ray mask changes its dissolution rate in a liquid solvent (developer). By this lithographic method, the mask pattern is, therefore, transferred to the material [120]. In our case, this lithographic approach is based on selective template removal and silica polycondensation induced by synchrotron radiation. The areas of the film that are not exposed to radiation can be selectively etched due to a lower crosslinking degree of the inorganic network. An important advantage of this method is the possibility of simultaneously removing the surfactant and inducing condensation of the silica network in a single-step process. Several patterned objects, not limited to periodic structures, have been obtained. By this approach, we have patterned several objects with different sizes and shapes on mesostructured silica films.

4.4.1 Sample preparation and characterisation setup

Mesostructured silica films were prepared as described in section 3.1.1, using block copolymer Pluronic F127 as the structure-directing agent and TEOS as the silicon source. An amount of 0.6 g of photoacid generator bis(4-tertbutylphenyl)iodonium p-toluenesulfonate (see Figure 4.20) was added to the final solution. The substrates chosen for deposition were p-type boron-doped, (100)-oriented, 400 μm-thick silicon wafers. The silicon substrates, previously cleaned with water, EtOH and rinsed with acetone, were dip-coated in the precursor sol at the pulling rate of 2.3 mm/s at the relative humidity (RH) of 40%.

The as-deposited mesostructured silica films were patterned at the DXRL beamline at Elettra synchrotron 3 hours after deposition. The samples were exposed through X-ray masks containing test patterns of different size, shape and geometry (5 to 500 μm). The masks had a gold absorber with thickness of 20 μm and a titanium transparent membrane with thickness of 2.2 μm. The deposited dose on the bottom of the film was 3 $kJ \cdot cm^{-3}$. After 12–24 hours from X-ray exposure, the

films were rinsed in a developing solution to remove the unirradiated parts of the mesostructure. The developing solution was optimised in order to obtain the etching in a time scale of seconds and the maximum aspect ratio for the patterned structures. This solution was prepared by mixing 35 ml of ethylene glycol with 10 ml of ethanol. The samples were sonicated for 20–30 seconds in the solution, then they were dried under an air flow. The films, after the lithographic process, were thermally treated at 150°C for 1 hour in order to stabilise the inorganic network.

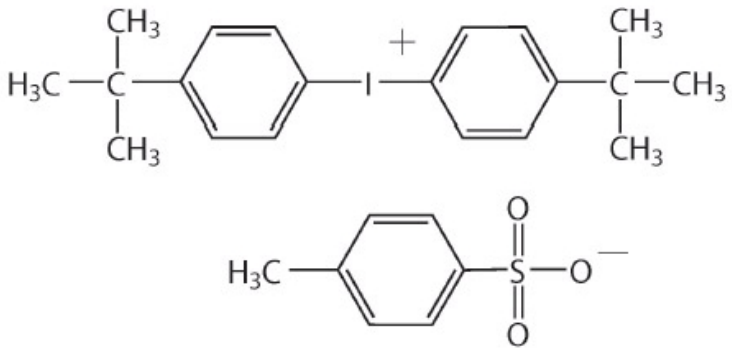

Figure 4.20: Photoacid generator used in the fabrication of patterned mesostructured silica films: bis(4-tert-butylphenyl)iodonium p-toluenesulfonate.

The mesostructure was investigated by GISAXS with an incident wavelength of 1.54 Å. TEM images were obtained in bright field mode on a JEOL 200CX microscope equipped with a tungsten cathode operating at 200 kV. Samples were prepared evaporating on a carbon-coated copper grid one drop of a suspension containing scratched fragments of the films in *n*-octane.

FTIR microscopy was performed at the SISSI beamline of the ELETTRA synchrotron. IR spectra were collected using a Bruker Hyperion 3000 microscope attached to a Bruker Vertex 70 interferometer working in the mid-IR range with a conventional Globar source and a KBr beamsplitter. The microscope was equipped with a liquid nitrogen-cooled MCT detector and a motorised sample stage that allowed mapping of the samples using a rectangular aperture of 15×30 μm^2. Each spectrum was obtained in transmission mode averaging 700 interferograms at a resolution of 8 cm^{-1}.

The samples were observed by an optical microscope Nikon Optiphot 500 both before and after the development. A white-light optical profiler (ADE-Shift MicroXAM) with a 50× objective was employed for the three-dimensional mapping of different patterned zones.

An NT-MDT Ntegra Atomic Force Microscope (AFM) was used to analyse the topography of the samples. Surfaces were measured at 0.5–1 Hz scan speed in semi-contact mode, using a silicon tip with nominal resonance frequency of 150 kHz, 5 N/m force constant, and 10 nm typical curvature radius. The same AFM was used to perform a DPN experiment in the following way. We have

prepared a solution containing Rhodamine 6G $8 \cdot 10^{-3}$ M and deposited a small volume (a droplet of 2 µl) on a Si surface. The AFM tip was then dipped into the droplet and subsequently moved above the patterned sample. The position was chosen by observation with the optical microscope and then the tip was approached onto the surface in contact mode. A square was drawn performing a 5×5 µm scan at 1 Hz. Another experiment was conducted leaving the whole sample in a diluted solution ($3 \cdot 10^{-5}$ wt% of Rhodamine 6G in ethanol) for 2 minutes. The sample was then extracted at controlled speed (140 mm/s) and rinsed 3 times with pure ethanol. The result of the DPN and dipping experiments was investigated by a confocal fluorescence microscope (Witec CRM 200), equipped with an Ar-Ion Laser (514 nm excitation line) and with a 200×200 μm^2 piezoelectric scanner. The spatial distribution of Rhodamine 6G has been detected mapping the fluorescence excited on the surface after the deposition process.

4.4.2 Experimental procedure and results

The patterned films were first observed by optical microscopy in order to assess the quality of the lithographic process. Figure 4.21 shows an optical micrograph of a patterned sample, in which patterned objects are discernible due to the difference in refractive index between the masked and the unmasked regions. The patterned areas appear white (Figure 4.21a), light blue (Figure 4.21b and 4.21c) or red (Figure 4.21d). This observation suggested that physical or chemical changes took place in the unmasked areas of the films. Therefore we used GISAXS and TEM to detect the mesophase variations in the films upon X-ray irradiation, while FTIR microscopy was employed to investigate the chemical changes induced on the mesoporous materials by the patterning process.

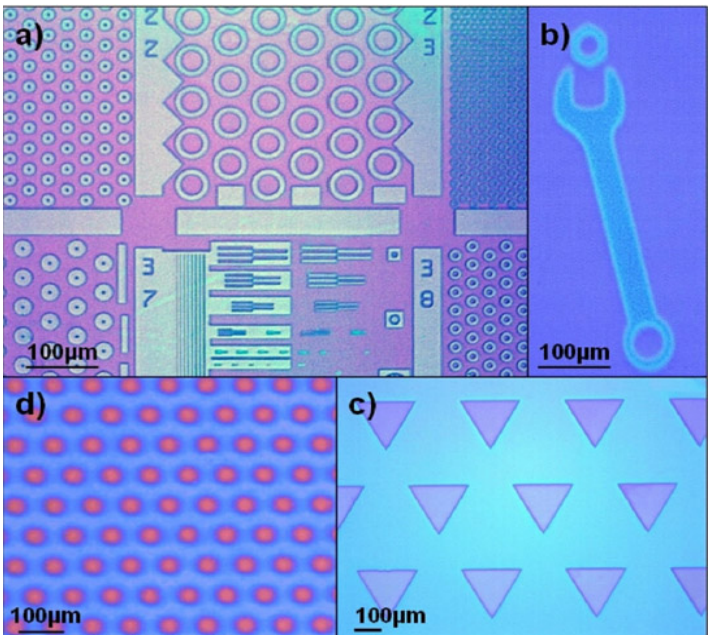

Figure 4.21: Optical micrograph of a patterned mesostructured silica film. The patterned objects can be discerned by their colour, due to the difference in refractive index between the masked and the unmasked regions.

In order to perform GISAXS tests, as-deposited mesostructured films were exposed to DXRL synchrotron radiation through a mask that covered half of the film, so that a large area of the sample could be investigated by the probing beam. GISAXS experiments showed that in both the irradiated and the masked regions, the mesostructure has two-dimensional hexagonal symmetry (space group *p6mm*), which is composed by a stack of tubular micelles packed in structures with hexagonal cross section [121]. TEM measurements confirmed a *p6mm* mesostructure with cylindrical micelles: cross-sectional images revealed the presence of either hexagonal stacking (front view, Figure 4.22a) or tubular structures (side view, Figure 4.22b). A comparison between the masked and unmasked GISAXS patterns showed that no substantial change in spot position and sharpness occurred, leading to conclude that no change in mesostructure symmetry took place upon deep X-ray patterning.

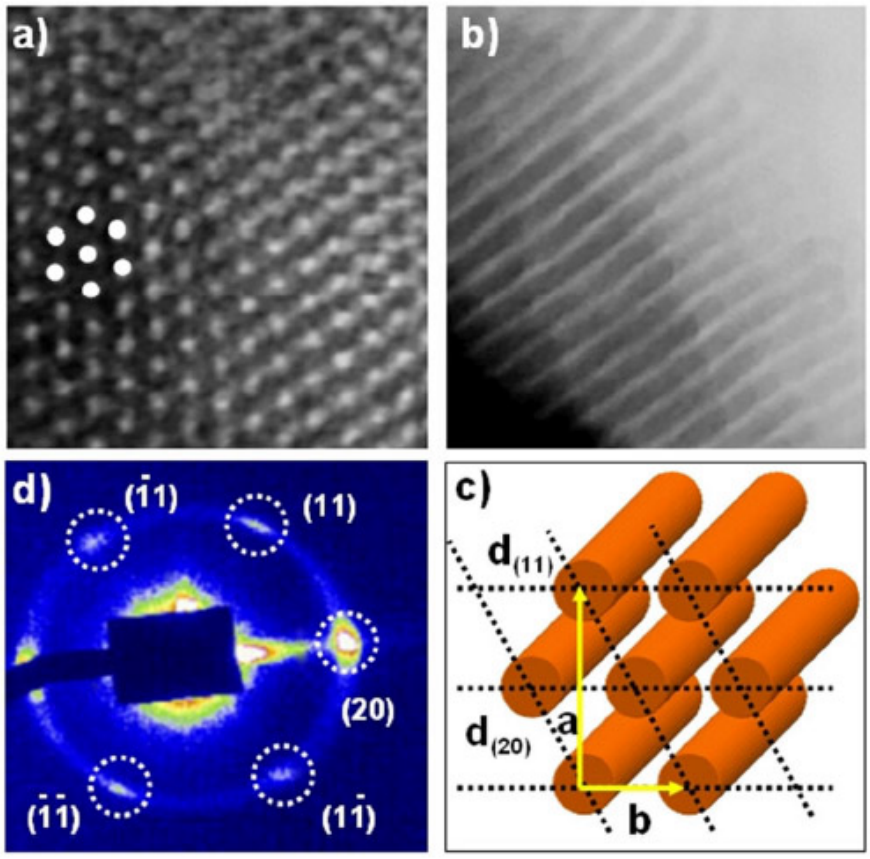

Figure 4.22: TEM images showing the shape of the cylindrical mesopores (a and b), which are disposed according to a two-dimensional hexagonal cross section (c). The GISAXS pattern reveals a *p6mm* symmetry group.

The exposure of the films to X-rays did not cause any change in the mesophase, but the regions that were not exposed to X-ray radiation could be easily etched, as described in the previous section. This developing process is fast and effective: optical profilometry measurements revealed that the masked areas of the samples were completely removed by the etching. Figures 4.23a and 4.23b show portions of a mesoporous film patterned with circular pillars 50 μm in diameter and

subsequently etched, whereas Figure 4.23c shows the results of a partial etching leading to low aspect ratio. We also evaluated whether the etching process affects the mesostructure, because in the etching procedure the whole film is soaked in the solution: this could cause a partial degradation of the Si-O-Si network resulting in loss of order or collapse of the inorganic walls with mesostructure disruption. However, an etched film presenting a large exposed area was investigated by GISAXS and no change in the diffraction patterns of the etched film was detected (not shown in figure), indicating that the mesostructure was retained upon etching. Mesostructure preservation is very important from the viewpoint of applications, in that the properties associated with the ordered mesostructure (e.g. high specific surface area, pore accessibility) must be retained in order to ensure functionality.

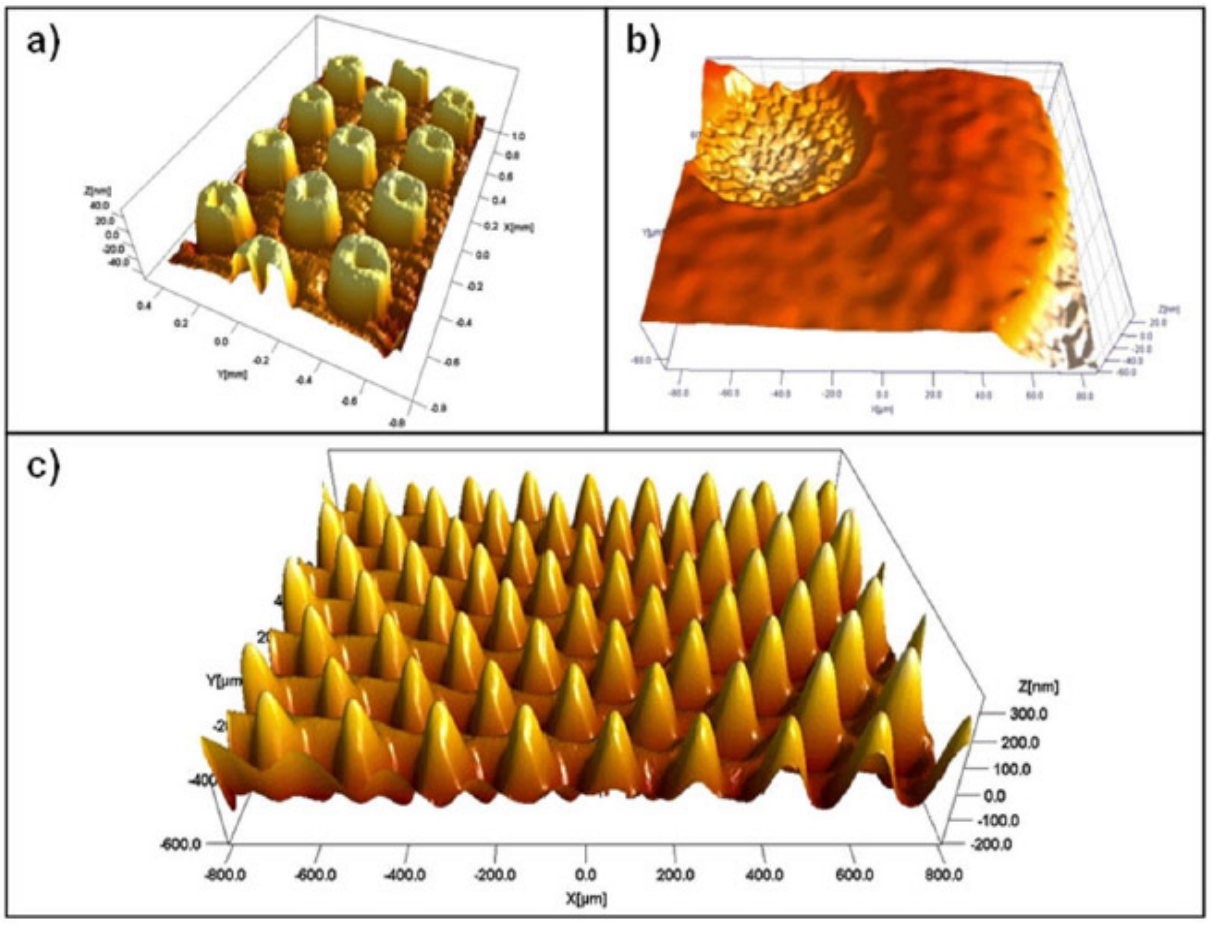

Figure 4.23: Optical profilometry of etched patterned mesoporous silica films relative to different objects: hollow pillars (a and b) and partial etching leading to low aspect ratio (c).

Regarding the physicochemical processes occurring during the lithographic process, the most likely hypothesis, supported by the literature, is that silica polycondensation reactions are induced by the acid photocatalyst upon activation by X-rays [113]. However, only indirect evidence has been reported on this point, therefore one of our goals was to elucidate this important aspect by infrared microscopy, which is a very useful tool to obtain a chemical mapping of an object on a micrometre

scale. We have chosen this imaging technique to study the chemical changes induced by the synchrotron radiation on the samples because it readily correlates the distribution of the chemical species by a three-dimensional mapping of the sample, providing a "chemical picture" of a selected area. This picture is composed of a fixed number of pixels, each containing an interferogram associated with a FTIR spectrum. The integrated areas of the spectra in a selected wavenumber interval are associated to a colour according to an intensity scale, therefore an image is obtained showing the presence of the chemical species relative to that wavenumber interval. We have conducted the experiments in transmission mode because Si substrates allows transmission of incident IR radiation.

The visible image taken by the integrated optical microscope (Figure 4.24a) refers to a 200×200 μm^2 portion of a sample which was patterned, but not etched. It shows a purple-pink ring corresponding to the irradiated region, whereas the light-blue portion corresponds to the unirradiated region. The same area was observed by infrared microscopy, by which an image was obtained (Figure 4.24b) by calculating the absorbance intensity of the FTIR spectrum at 2891 cm^{-1} (symmetric C-H stretching of CH_2 in Pluronic F127) after a baseline subtraction in the 3030–2840 cm^{-1} region. The different colours, corresponding to different intensities in a linear intensity scale, point out that a sharp decrease in intensity of the CH_2 stretching mode (2891 cm^{-1}) occurred in the ring area. This effect was induced by exposure to X-rays and can be quantified calculating the ratio between the maximum and the minimum band intensities along a diameter of the circular pillar reported in Figure 4.24a. In this case the reduction of the CH_2 stretching band between the points A and B (see Figure 4.24a) is around 38%. This indicates a partial removal of the surfactant by the incident radiation.

Another chemical map was obtained from the data collected in the same experiment by integrating the Si-OH stretching band around 930 cm^{-1} (Figure 4.24c). These data show a strong decrease of silanols in the exposed areas, which is associated with higher silica degree of polycondensation. The mechanism, supported by other works, is the decrease of pH upon X-ray irradiation due to photodecomposition of the photoacid, which yields aryliodo radical-cation and aryl-radical species [122]. The decrease of pH from ~2 to ~0 leads to acid-catalysed inorganic polycondensation [113]. De-polymerisation in the organic phase is likely to be caused by the radicalic species generated upon irradiation from the photoacid molecules [122]. As reported in the literature, X-rays can induce a radicalic de-polymerisation in the organic phase which may be caused by OH free radicals created from water molecules by high-flux radiation, either via direct homolysis or via photoelectric effect [123,124]. Because this phenomenon is not detected in films prepared without photoacid initiator, a leading role should be attributed to the photoinitiator molecules.

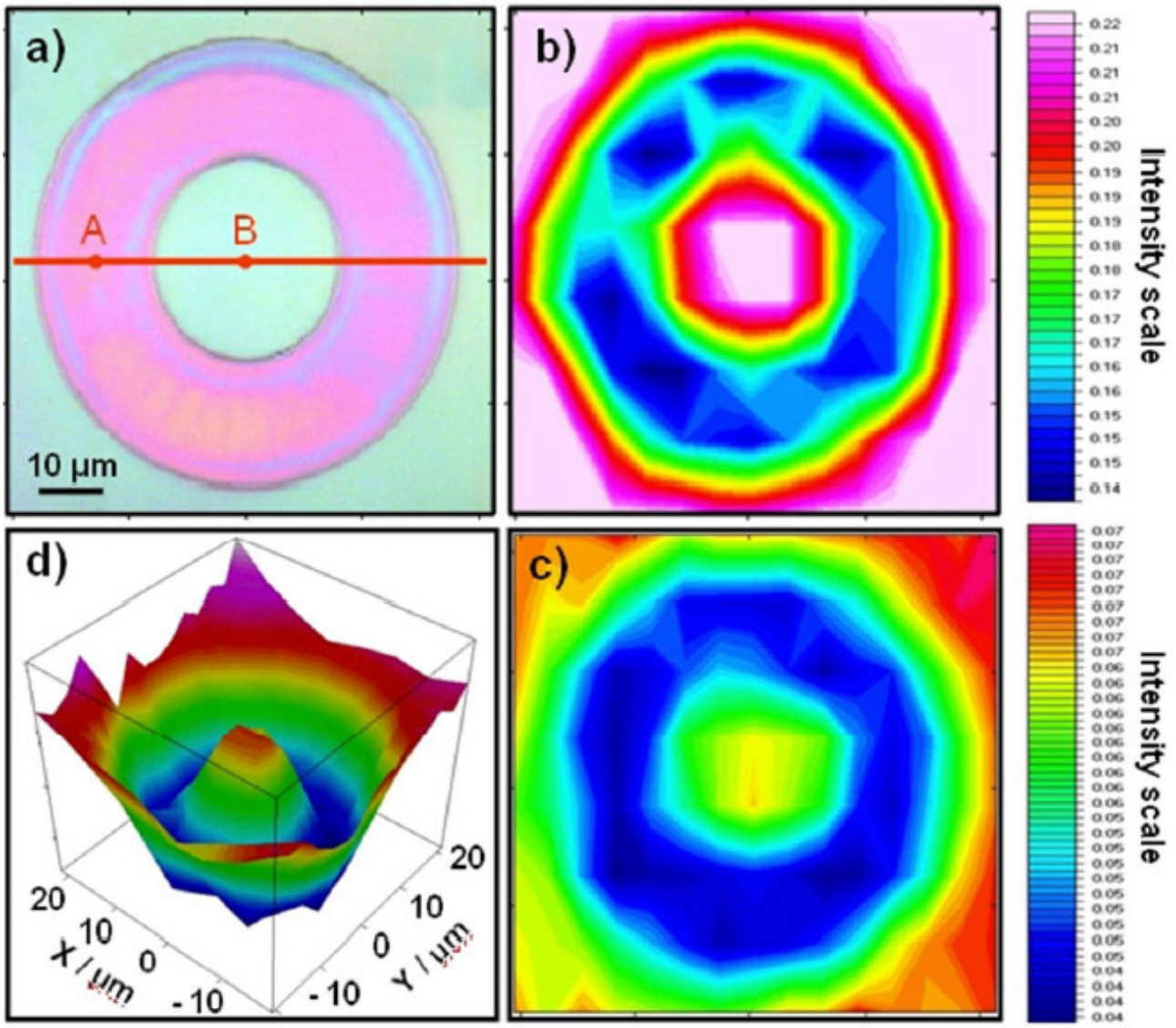

Figure 4.24: Visible image (a) and FTIR microscopy images relative to template (b and d) and silanols (c).

As a crosscheck, we have exposed mesostructured silica films that did not contain the photoinitiator: no difference in silica condensation between the irradiated and the unirradiated regions of the film was detected as well as no difference in organic removal (not shown in figure). The observation that the irradiated areas of the patterned films containing the photoinitiator were preserved after the exposure and the developing process, whereas the unexposed areas were easily dissolved, confirms the increased degree of polycondensation of the silica network induced by the photoacid.

One of the aims of this work was to test integration of top-down techniques with the bottom-up self-assembly pathway leading to mesostructure formation. The lithographic approach by DXRL enabled the fabrication of isolated mesoporous pillars; another top-down technique was chosen to chemically functionalise the pillars by means of a controlled writing process using an atomic force microscope. In a proof-of-concept experiment, the AFM cantilever tip was used as a dip-pen using

rhodamine 6G as the ink in order to functionalise selected mesoporous pillars. The AFM cantilever tip was dipped into the rhodamine solution so that it took up a drop of solution, then it was approached to its destination pillar. When the cantilever landed on the pillar and the solution came into contact with the film, capillary forces drove the solution from the cantilever tip into the pillar, so that the mesopores became filled with the rhodamine solution.

The results of this controlled writing process were observed by confocal fluorescence microscopy. Figure 4.25a shows the mapping of the fluorescence signal integrated in the spectral range 530–580 nm. The two regions where the dip-pen functionalisation was performed are characterised by a high fluorescence intensity and can be clearly distinguished on two separate pillars. Here, the signal due to rhodamine is two orders of magnitude higher than the background, which might be due to the slight fluorescence effect typically found in sol-gel derived materials. This experiment demonstrates that, using this method, it is possible to fabricate highly fluorescent mesoporous microstructures by the functionalisation of micrometric mesoporous objects with different guest molecules (for example, oligonucleotide strands can be attached to the pillars in the fabrication of microarrays for DNA spotting). The lateral feature size of the patterned pillars corresponds to the conditions for microarray deposition, which are typically around 30 μm [125]. The lateral resolution of AFM enables functionalisation of sub-micron mesoporous objects using small amounts of analytes; in addition, the patterned mesoporous support maximises the adsorption of guest molecules due to the high specific surface area of mesoporosity. Furthermore, the hexagonal *p6mm* mesostructure allows accessibility of the material from the outside and diffusion of analytical species into the material, opening the route for efficient immobilisation of biological species in analytical applications.

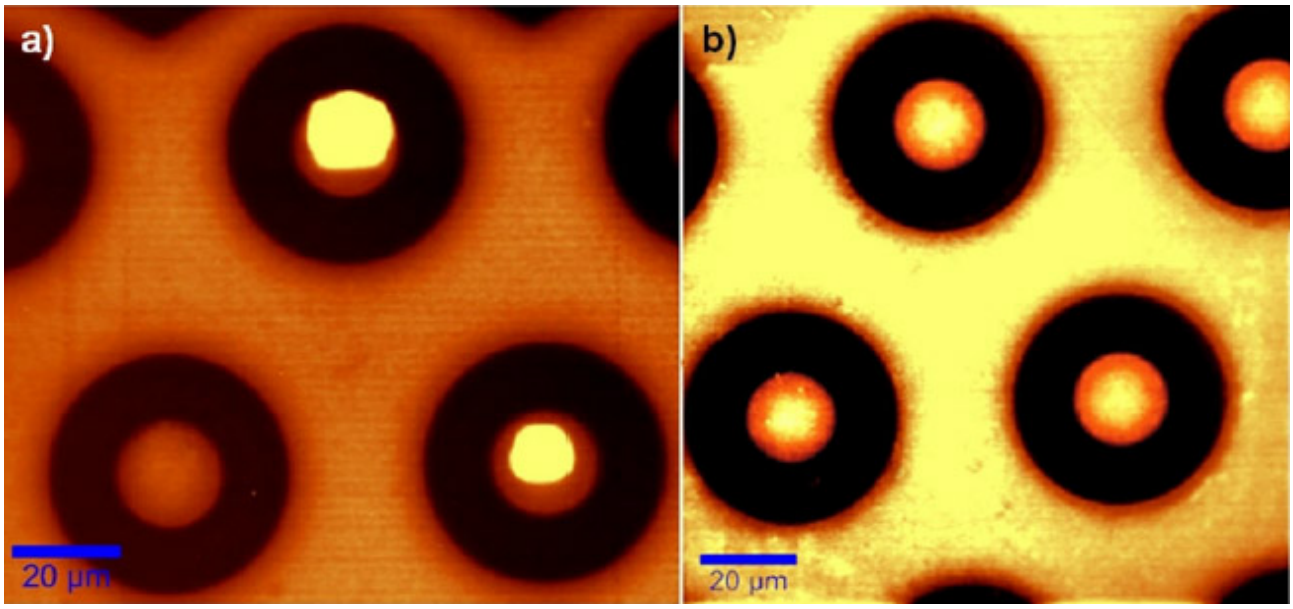

Figure 4.25: Results of the dip-pen functionalisation process showing fluorescence integrated in the spectral range 530–580 nm (a). It is compared to the fluorescence of a totally impregnated film (b).

Another experiment was performed with the aim of testing the fluorescence efficiency of the patterned structure. A patterned mesoporous film was impregnated with a $3 \cdot 10^{-5}$ wt% rhodamine 6G solution in ethanol: the sample was soaked in this solution for 2 minutes, then it was rinsed with ethanol to ensure that no excess solution was left on the film surface. Confocal fluorescence microscopy (Figure 4.25b) revealed the presence of rhodamine 6G on the mesoporous patterned areas, whereas the etched regions of the film showed no fluorescence, with around one order of magnitude between the fluorescence intensity in the etched (dark areas) and unetched (bright areas) regions. This also demonstrated that the etching process completely removes the unexposed region of the film, leaving no residue of the film on the substrate.

To summarise, ordered mesoporous silica films were patterned by means of deep X-ray lithography using synchrotron radiation, obtaining mesoporous objects with controlled size and shape. The mesostructure was investigated by GISAXS and TEM, revealing an ordered two-dimensional hexagonal p6mm structure. The patterning mechanism was studied by infrared imaging, which provided evidence for the selective increase of silica polycondensation and the partial removal of the templating agent. A dip-pen approach using an atomic force microscope enabled selective functionalisation of the mesoporous objects with rhodamine 6G. This experiment allows envisioning new fabrication technologies of functional materials for applications such as, for example, DNA nano-spotting or lab-on-a-chip devices.

References

[1] Special issue on self-assembly, *Proc. Natl. Acad. Sci. U.S.A.* 99(8) (2002).

[2] S. Förster, T. Plantenberg, *Angew. Chem. Int. Ed. Engl.* 41, 688 (2002).

[3] F. Schüth, K.S.W. Sing, J. Weitkamp, editors, *Handbook of porous solids*, Wiley-VCH Verlag GmbH, Weinheim, Germany, 2002.

[4] A. Sayari, P. Liu, *Microp. Mater.* 12, 149 (1997).

[5] J. Roquerol, D. Avnir, C.W. Fairbridge, D.H. Everett, J.H. Haynes, N. Pernicone, J.D.F. Ramsay, K.S.W. Sing, K.K. Unger, *Pure and Appl. Chem.* 66, 1739 (1994).

[6] C.T. Kresge, M.E. Leonowicz, W.J. Roth, J.C. Vartuli, J.S. Beck, *Nature* 359, 710 (1992).

[7] C.J. Brinker, G.W. Scherer. *Sol-gel science: The physics and chemistry of sol-gel processing*, Academic Press, San Diego, 1992.

[8] J.D. Wright, N.A.J.M. Sommerdijk, *Sol-gel materials: Chemistry and applications*, CRC Press, Boca Raton, 2001.

[9] W. Stober, A. Fink, E. Bohn, *J. Colloid Interface Sci.* 26, 62 (1968).

[10] J.N. Israelachvili, *Intermolecular and surface forces*, Academic Press Ltd., London, 2nd edition, 1998.

[11] A. Firouzi, F. Atef, A.G. Oertli, G.D. Stucky, B.F. Chmelka, *J. Am. Chem. Soc.* 119, 3596 (1997).

[12] N. Israelachvili, D.J. Mitchell, B.W. Niham, *J. Chem. Soc.* 72, 1525 (1976).

[13] J. Israelachvili, *Intermolecular and surface forces*, 2nd Ed. Academic Press, New York, 1992.

[14] Q. Huo, R. Leon, P.M. Petroff, G.D. Stucky, *Science* 268, 1324 (1995).

[15] Q. Huo, D.I. Margolese, U. Ciesla, P. Feng, T.E. Gier, P. Sieger, R. Leon, P.M. Petroff, F. Schuth, G.D. Stucky, *Nature* 368, 317 (1994).

[16] P.T. Tanev, T.J. Pinnavaia, *Science* 267, 865 (1995).

[17] A. Thomas, H. Schlaad, B. Smarsly, M. Antonietti, *Langmuir* 19, 4455 (2003).

[18] P.F.W. Simon, R. Ulrich, H.W. Spiess, U. Wiesner, *Chem. Mater.* 13, 3464 (2001).

[19] R. Ivanova, B. Lindman, P. Alexandridis, *Adv. Colloid Interf. Sci.* 89-90, 351 (2001).

[20] D. Zhao, J. Feng, Q. Huo, N.A. Melosh, G.H. Fredrickson, B.F. Chmelka, G.D. Stucky, *Science* 279, 548 (1998).

[21] F. Tiberg, J. Brinck, L. Grant, *Curr. Opinion Colloid Interf. Sci.* 4, 411 (2000).

[22] N.A. Melosh, P. Lipic, F.S. Bates, F. Wudl, G.D. Stucky, G.H. Fredrickson, B.F. Chmelka, *Macromolecules* 32, 4332 (1999).

[23] P.C.A. Alberius-Henning, K.L. Frindell, R.C. Hayward, E.J. Kramer, G.D. Stucky, B.F. Chmelka, *Chem. Mater.* 14 (2002).

[24] G.J.A.A. Soler-Illia, E. Crepaldi, D. Grosso, C. Sanchez, *Chem. Comm.* 9, 2298 (2002).

[25] R. Ivanova, P. Alexandridis, B. Lindmann, *Colloids Surf. A* 183–185, 41 (2001).

[26] G.J.A.A. Soler-Illia, C. Sanchez, *New J. Chem.* 24, 493 (2000).

[27] C.J. Brinker, Y. Lu, A. Sellinger, H. Fan, *Adv. Mater.* 11, 579 (1999).

[28] G. Cortial, M. Siutkowski, F. Goettmann, A. Moores, C. Boissière, D. Grosso, P. Le Floch, C. Sanchez, *Small* 2, 1042 (2006).

[29] S. Besson, T. Gacoin, C. Ricolleau, C. Jacquiod, J.P. Boilot, *Nano Lett.* 2, 409 (2002).

[30] D. Grosso, F. Babonneau, G. Soler-Illia, P.A. Albouy, H. Amenitsch, *Chem. Comm*. 748 (2002).

[31] D. Grosso, F. Babonneau, P.A. Albouy, H. Amenitsch, A.R. Balkenende, A. Brunet-Bruneau, J. Rivory, *Chem. Mater.* 14, 931 (2002).

[32] C. Kittel, *Introduction to solid state physics*, John Wiley & Sons, 7th edition, 1996.

[33] N.W. Ashcroft, N.D. Mermin, *Solid state physics*, Harcourt College Publishers, 1976.

[34] T.N. Blanton, T.C. Huang, H. Toraya, C.R. Hubbard, S.B. Robie, D. Louer, H.E. Gobel, G. Will, R. Gilles, T. Raftery, *Powder Diffr.* 10, 91 (1995).

[35] http://www.esrf.eu/computing/scientific/FIT2D/ (accessed in October 2008).

[36] http://www.ncnr.nist.gov/programs/crystallography/software/cmpr/ (accessed in November 2008).

[37] http://cobweb.ecn.purdue.edu/~hgroup/Research/Nanocell/NANOCELL.html
(accessed in November 2008).

[38] M. Cestelli Guidi, M. Piccinini, A. Marcelli, A. Nucara, P. Calvani, E. Burattini, *J. Opt. Soc. Am. A* 22, 2810 (2005).

[39] A. Nucara, S. Lupi, P. Calvani, *Infr. Phys. Tech.* 45, 375 (2004).

[40] I. Noda, *Bull. Am. Phys. Soc.* 31, 520 (1986).

[41] I. Noda, *J. Am. Chem. Soc.* 111, 8116 (1989).

[42] I. Noda, *Appl. Spectrosc.* 44, 550 (1990).

[43] I. Noda, *Appl. Spectrosc.* 47, 1329 (1993).

[44] I. Noda, *Appl. Spectrosc.* 54, 994 (2000).

[45] I. Noda, Y. Ozaki, *Two-dimensional correlation spectroscopy: applications in vibrational and optical spectroscopy*, J. Wiley & Sons, 2004.

[46] P. Falcaro, D. Grosso, H. Amenitsch, P. Innocenzi, *J. Phys. Chem. B* 108, 10942 (2004).

[47] E.L. Crepaldi, G. Soler-Illia, D. Grosso, F. Cagnol, F. Ribot, C. Sanchez, *J. Am. Chem. Soc.* 125, 9770 (2003).

[48] E.L. Crepaldi, G. Soler-Illia, A. Bouchara, D. Grosso, D. Durand, C. Sanchez, *Angew. Chem. Int. Ed. Engl.* 42, 347 (2003).

[49] http://rsb.info.nih.gov/ij/ (accessed in November 2008)

[50] R.N. Ward, D.C. Duffy, P.B. Davies, C.D. Bain, *J. Phys. Chem.* 98, 8536 (1994).

[51] J. Gallardo, A. Duran, D. Di Martino, R. Almeida, *J. Non-Cryst. Solids* 298, 219 (2002).

[52] P. Innocenzi, *J. Non-Cryst. Solids* 316, 309 (2003).

[53] P. Innocenzi, P. Falcaro, D. Grosso, F. Babonneau, *J. Phys. Chem. B* 107, 4711 (2003).

[54] Y. Su, J.Wang, H. Liu, *Macromolecules* 35, 6426 (2002).

[55] H. Yoshino, K. Kamiya, H. Nasu, *J. Non-Cryst. Solids* 126, 68 (1990).

[56] A. Fidalgo, L.M. Ilharco, *J. Non-Cryst. Solids* 283, 144 (2001).

[57] K. Kamiya, T. Yoko, K. Tanaka, M. J. Takeuchi, *J. Non-Cryst. Solids* 121, 182 (1990).

[58] K. Davis, M.J. Tomozawa, *J. Non-Cryst. Solids* 201, 177 (1996).

[59] X.S. Zhao, G.Q. Lu, A.K. Whittaker, G.J. Millar, H.Y. Zhu, *J. Phys. Chem. B* 101, 6525 (1997).

[60] J. Chen, Q. Li, R. Xu, F. Xiao, *Angew. Chem. Int. Ed. Engl.* 34, 2694 (1995).

[61] S. Sugahara, T. Kadoya, K.I. Usami, T. Hattori, M. Matsumura, *J. Electrochem. Soc.* 148, F120 (2001).

[62] F.L. Galeneer, *Phys. Rev. B* 19, 4292 (1979).

[63] S. Besson, T. Gacoin, C. Jacquiod, C. Ricolleau, D. Babonneau, J.P. Boilot, *J. Mater. Chem.* 10, 1331 (2000).

[64] K.M. Davis, M. Tomozawa, *J. Non-Cryst. Solids* 201, 177 (1996).

[65] G.E. Walrafen, S.R. Samanta, *J. Chem. Phys.* 69, 493 (1978).

[66] J.G. Bayly, V.B. Kartha, W.H. Stevens, *Infrared Phys.* 3, 211 (1963).

[67] Y. Shen, P. Wu, *J. Phys. Chem. B* 107, 4224 (2003).

[68] P. Innocenzi, P. Falcaro, D. Grosso, F. Babonneau, *J. Phys. Chem. B* 107, 711 (2003).

[69] A. Bearzotti, J. Mio Bertolo, P. Innocenzi, P. Falcaro, E. Traversa, *J. Eur. Ceramic Soc.* 24, 1969 (2004).

[70] J. Mio Bertolo, A. Bearzotti, P. Falcaro, E. Traversa, P. Innocenzi, *Sensor Letters* 1, 64 (2003).

[71] P. Falcaro, S. Costacurta, G. Mattei, H. Amenitsch, A. Marcelli, M.C. Guidi, M. Piccinini, A. Nucara, L. Malfatti, T. Kidchob, P. Innocenzi, *J. Am. Chem. Soc.* 127, 3838 (2005).

[72] P. Innocenzi, M.O. Abdirashid, M. Guglielmi, *J. Sol-Gel Sci. Technol.* 3, 47 (1994).

[73] R.E. Galindo, A. Van Veen, H. Schut, S.W.H. Eijt, C.V. Falub, A.R. Balkenende, F.K. De Theije, *Mater. Eng. B* 102, 403 (2003).

[74] D.L. Wetzel, Vib. Spectrosc. 29, 291 (2003).

[75] F. Cagnol, D. Grosso, G.J. de A.A. Soler-Illia, E.L. Crepaldi, F. Babonneau, H. Amenitsch and C. Sanchez, *J. Mater. Chem.* 13, 61 (2003).

[76] D.A. Doshi, A. Gibaud, V. Goletto, M. Lu, H. Gerung, B. Ocko, S.M. Han, C.J. Brinker, *J. Am. Chem. Soc.* 125, 11646 (2003).

[77] C.S. Ashley, S.T. Reed, *US Patent 4929278*, 1990.

[78] S. Hofacker, M. Mechtel, M. Magerb, H. Kraus, *Prog. Org. Coat.* 45, 159 (2002).

[79] D. Grosso, F. Cagnol, G.J. Soler-Illia, E.L. Crepaldi, H. Amenitsch, A. Brunet-Bruneau, A. Bourgeois, C. Sanchez, *Adv. Funct. Mater.* 14, 309 (2004).

[80] K. Sefiane, L. Tadrist, M. Douglas, *Int. J. Heat Mass Transf.* 46, 4527 (2003).

[81] A. Cheng, K.H. Sefiane, D. Soolaman, L. Tadrist, M. Douglas, H.Z. Yu, *Int. J. Phys. Chem. B* 110, 11267 (2006).

[82] R.J. Hopkins, J.P. Reid, *J. Phys. Chem. A* 109, 7923 (2005).

[83] H.M. Tzeng, K.F. Wall, M.B. Long, R.K. Chang, *Opt. Lett.* 9, 273 (1984).

[84] H.Y. Erbil, G. McHale, M.I. Newton, *Langmuir* 18, 2636 (2002).

[85] C.N. Lam, R. Wu, D. Li, M.L. Hair, A.W. Neumann, *Adv. Colloid Interf. Sci.* 96, 169 (2002).

[86] X. Fang, B. Li, E. Petersen, Y. Ji, J.C. Sokolov, M.H. Rafailovich, *J. Phys. Chem. B* 109, 20554 (2005).

[87] E.K. Plyler, *J. Res. Nat. Bureau Stand.* 48, 281 (1952).

[88] V.H. Segtnan, S. Sasic, T. Isaksson, Y. Ozaki, *Anal. Chem.* 73, 3153 (2001).

[89] V. Buch, J.P. Devlin, Eds. *Water in Confining Geometries*; Springer,: New York, 2003.

[90] C. Boissiere, J.B. Brubach, A. Marmet, G. De Marzi, C. Bourgaux, E. Prouzet, P. Roy, *J. Phys. Chem. B* 106, 1032 (2002).

[91] B. Czarnik-Matusewicz, S. Pilorz, J.P. Hawranek, *Anal. Chim. Acta* 544, 15 (2005).

[92] J.B. Brubach, A. Mermet, A. Filabozzi, A. Gerschel, P. Roy, *J. Chem. Phys.* 122, 184509 (2005).

[93] J.B. Brubach, A. Mermet, A. Filabozzi, A. Gerschel, D. Lairez, M.P. Krafft, P. Roy, *J. Chem. Phys.* 105, 430 (2001).

[94] D.R. Lide, Ed. CRC-Handbook of Chemistry and Physics, 87th ed., Taylor and Francis, Boca Raton, FL, 2007, pp 6-157.

[95] C. Bourges-Monnier, M.E.R. Shanahan, *Langmuir* 11, 2820 (1995).

[96] K.S. Birdi, D.T. Vu, A. Winter, *J. Phys. Chem.* 93, 3702 (1989).

[97] B. Czarnik-Matusewicz, S. Pilorz, *Vibr. Spectr.* 40, 235 (2006).

[98] D.E. Khoshtariya, T.D. Dolidze, P. Lindqvist-reis, A. Neubrand, R. Van Eldik, *J. Mol. Liquids* 96–97, 45 (2002).

[99] R.D. Deegan, O. Bakajin, T.F. Dupont, G. Huber, S.R. Nagel, T.A. Witten, *Nature* 389, 827 (1997).

[100] R.D. Deegan, O. Bakajin, T.F. Dupont, G. Huber, S.R. Nagel, T.A. Witten, *Phys. Rev. E* 62, 756 (2000).

[101] R.D. Deegan, *Phys. Rev. E* 61, 475 (2000).

[102] J. Conway, H. Korns, M.R. Fisch, *Langmuir* 13, 426 (1997).

[103] B.J. Fischer, *Langmuir* 18, 60 (2002).

[104] E. Rabani, D.R. Reichman, P.L. Geissler, L.E. Brus, *Nature* 426, 271 (2003).

[105] T.P. Bigioni, X.M. Lin, T.T. Nguyen, E.I. Corwin, T.A. Witten, H.M. Jaeger, *Nature* 5, 265 (2006).

[106] C. Bourgés-Monnier, M.E.R. Shanahan, *Langmuir* 11, 2820 (1995).

[107] V. Dugas, J. Broutin, E. Souteyrand, *Langmuir* 21, 9130 (2005).

[108] J.Y. Cheng, C.A. Ross, H.I. Smith, E.L. Thomas, *Adv. Mater.* 18, 2505 (2006).

[109] G.A. Ozin, S.M. Yang, *Adv. Funct. Mater.* 11, 95 (2001).

[110] G. Soler-Illia, C. Sanchez, B. Lebeau, J. Patarin, *Chem. Rev.* 102, 4093 (2002).

[111] P. Innocenzi, P. Falcaro, S. Schergna, M. Maggini, E. Menna, H. Amenitsch, G. Soler-Illia, D. Grosso, C. Sanchez, *J. Mater. Chem.* 14, 1838 (2004).

[112] B.J. Scott, G. Wirnsberger, M.D. McGehee, B.F. Chmelka, G.D. Stucky, *Adv. Mater.* 13, 1231 (2001).

[113] D.A. Doshi, N. Huesing, M. Lu, H. Fan, Y. Lu, K. Simmons-Potter, B.G. Potter Jr, A.J. Hurd, C.J. Brinker, *Science* 290, 107 (2000).

[114] H. Fan, Y. Lu, A. Stump, S.T. Reed, T. Baer, R. Schunk, V. Perez-Luna, G.P. Lopez, C.J. Brinker, *Nature* 405, 56 (2000).

[115] Y. Lu, Y. Yang, A. Sellinger, M. Lu, J. Huang, H. Fan, R. Haddad, G. Lopez, A.R. Burns, D.Y. Sasaki, J. Shelnutt, C.J. Brinker, *Nature* 410, 913 (2001).

[116] F. Cerrina, *J. Phys. D* 33, R103 (2000).

[117] K. Salaita, Y. Wang, C.A. Mirkin, *Nat. Nanotechnol.* 2, 145 (2007).

[118] M. Su, X. Liu, S.Y. Li, V.P. Dravid, C.A. Mirkin, *J. Am. Chem. Soc.* 124, 1560 (2002).

[119] L. Malfatti, T. Kidchob, S. Costacurta, P. Falcaro, P. Schiavuta, H. Amenitsch, P. Innocenzi, *Chem. Mater.* 18, 4553 (2006).

[120] E.W. Becker, W. Ehrfeld, P. Hagmann, A. Maner, D. Münchmeyer, *Microelectron. Eng.* 4, 35 (1986).

[121] D. Grosso, A.R. Balkenende, P.A. Albouy, A. Ayral, H. Amenitsch, F. Babonneau, *Chem. Mater.* 13, 1848 (2001).

[122] J.V. Crivello, J.H.W. Lam, *Macromolecules* 10, 1307 (1977).

[123] A.F. Gross, M.R. Diehl, K.C. Beverly, E.K. Richman, S.H. Tolbert, *J. Phys. Chem. B* 107, 5475 (2003).

[124] W.S. Seo, J.H. Lee, X. Sun, Y. Suzuki, D. Mann, Z. Liu, M. Terashima, P.C. Yang, M.V. McConnell, N.D.G.H. Dai, *Nature Materials* 5, 971 (2006).

[125] S. Besson, T. Gacoin, C. Jacquiod, C. Ricolleau, J.P. Boilot, *Mat. Res. Soc. Symp. Proc.* 707 (2002).

CONCLUSIONS

During the three years of this doctorate work great steps forward have been taken in the deposition, characterization and application of mesoporous silica films obtained by sol-gel processing. Well assessed experimental techniques, as SAXS and TEM applied ex-situ, have been used to characterize thoroughly the mesophase symmetry of silica and hybrid organic-inorganic films and membranes obtained by evaporation-induced self-assembly and dip-coating. Time-resolved rapid-scan FTIR spectroscopy has been used in-situ to study the kinetics of polycondensation reactions during film formation. The FTIR technique has shown to be very powerful to understand in great detail the chemical-physical processes that take place during film formation. It has been applied in-situ also simultaneously with SAXS, to have both the structural and chemical information and it has allowed to establish the important role of ethanol and water related to micelle formation and mesostructure organization with time.

These results have led us to investigate in great detail the evaporation processes of water and ethanol and how they are influenced by the environmental conditions (i.e., relative humidity), which play a fundamental role in the final properties of the as-deposited mesoporous film. The power of the IR technique has been confirmed also by its application as time-resolved FTIR imaging to study the coffee-stain effect in a pure solvent-solute system.

Finally, it has been shown that it is possible to fabricate mesoporous functionalized arrays with controlled size and shape by integrating deep X-ray lithography with dip-pen writing. It has been possible to control the quality of the whole production process by means of characterization techniques currently available in a modern synchrotron facility. The successful application of these bottom-up and top-down techniques allows to envisage new fabrication technologies of functional mesoporous materials for applications, such as DNA nano-spotting or lab-on-a-chip devices.

Acknowledgements

In the three years of this doctorate there are really many persons I must thank, as in different manners they allowed me to start and finish successfully this work. The very first of them is Plinio Innocenzi, who trusted me and gave me the opportunity of working within his group. I have enjoyed very much this experience and have learnt really a lot. I am very grateful to Luca Malfatti, Stefano Costacurta, Paolo Falcaro, Tongjit Kidchob, Masaide Takahashi for the efforts and the ideas they have continuously put in developing this work. I must thank also Enrico Traversa and Silvia Licoccia, as they also trusted me and allowed to start this doctorate at University "Tor Vergata".

I thank Annibale Mottana and Giancarlo Della Ventura of University Roma Tre, who partially funded my assegno di ricerca during the first two years of the doctorate and Stelluccia Nunziante Cesaro of CNR-ISMN who funded the assegno di ricerca in the third year, together with Carlo Guaraldo and Mario Calvetti who gave me a short contract at INFN-LNF.

The experimental part of this doctorate was carried on mainly in two synchrotron facilities. The first one is SINBAD beamline in Laboratorio Daϕne-Luce of INFN-LNF, where Claudio Marcelli and Emilio Burattini gave me the opportunity to start working in 2001, with the daily fruitful collaboration of Mariangela Cestelli Guidi. I must thank also Gianfelice Cinque, Giannantonio Cibin, Antonella Balerna, Giorgio Cappuccio, Daniele Di Gioacchino, Emanuele Pace, Benjamin Robouch, Dariush Hampai, Alessio Bocci and the whole technical staff: Antonio Grilli, Agostino Raco, Marco Pietropaoli, Giacomo Viviani and Antonietta Frani. This seven-year long experience has been fundamental for my scientific formation and every day it has been a pleasure to work with them all. The second synchrotron facility is ELETTRA. I must thank Heinz Amenitsch of the SAXS beamline, Benedetta Marmiroli of the DXRL beamline, Lisa Vaccari and Andrea Perucchi of the SISSI beamline for their fundamental assistance. Surely, this scientific work wouldn't have been possible without the skilful and generous contribution of Pierangelo Morini and Diego Sali of Bruker Optics. I have had also very fruitful collaborations with: Paolo Calvani, Paolo Postorino, Alessandro Nucara, Stefano Lupi, Fabio Bellatreccia, Giuseppe Bellisola, Agostina Congiu Castellano, Cyril Petibois, Wojtek Kwiatek, Pascale Roy, David Moss, Ulrich Shade.

Finally, I must thank Antonella, who supported me in these three years, in which we started our engagement in January 2006, she accepted to become my wife in June 2007 and gave me our son Adrian in April 2008. As a chemist, Antonella helped me also to understand better the world of chemistry.